1 Iron Cycling and Isotopic Fractionation in a Ferruginous, Seasonally

2 Ice-Covered Lake

3

- 4 Andy W. Heard^{1,2,*}, Chadlin M. Ostrander^{2,3,4}, Elizabeth D. Swanner⁵, Kathryn Rico^{5,6}, Sune G.
- 5 Nielsen^{1,2,7}.

6

- 7 ¹Department of Geology & Geophysics, Woods Hole Oceanographic Institution, Woods Hole, MA,
- 8 USA
- 9 ²NIRVANA Laboratories, Woods Hole Oceanographic Institution, Woods Hole, MA, USA
- ³Department of Geology & Geophysics, University of Utah, Salt Lake City, UT, USA
- ⁴Department of Marine Chemistry & Geochemistry, Woods Hole Oceanographic Institution,
- 12 Woods Hole, MA USA
- ⁵Department of Geological and Atmospheric Sciences, Iowa State University, Ames, IA, USA
- ⁶School of Earth and Space Exploration, Arizona State University, Tempe, AZ, USA.
- ⁷CRPG, CNRS, Université de Lorraine, 15 rue Notre Dame des Pauvres, 54501 Vandoeuvre lès
- 16 Nancy, France

17

- 18
- **Corresponding author: <u>andrew.heard@whoi.edu</u>

20

21 For submission to Geochimica et Cosmochimica Acta

22

23 Keywords: Ferruginous lakes; iron isotopes, seasonal; Precambrian oceans; iron formations

24

- 25 Abstract (490 words)
- Ferruginous conditions, defined by anoxia and abundant dissolved ferrous iron (Fe^{2+}_{aq}), dominated
- 27 the Precambrian oceans but are essentially non-existent in a modern, oxygenated world.
- 28 Ferruginous meromictic lakes represent natural laboratories to ground truth our understanding of
- 29 the stable Fe isotope proxy, which has been used extensively in interpreting the origins of Fe-rich
- sedimentary rocks like iron formations (IFs) and the interactions of early life with high-Fe²⁺aq

conditions. Here we report comprehensive geochemical and Fe isotopic analyses of samples collected in May and August 2022, and March 2023, from Deming Lake, Minnesota, a ferruginous meromictic lake that undergoes surface freezing in winter and never becomes euxinic. Through chemical and Fe isotopic analyses of different putative Fe sources to Deming Lake; including eolian input trapped in winter ice cover, nearby bogs, and regional groundwaters sampled at surface springs; we find that a groundwater source provides the best chemical and Fe isotopic match for Deming Lake and can support Fe²⁺_{aq}-rich waters at depth that maintain a permanent chemocline at ~12 m. The ice-free Deming Lake water column can be split into three layers dominated by distinct Fe cycling regimes. Layer (I) extends from the lake surface to the base of the oxycline at ~6 m, and its Fe cycling is dominated by isotopically light Fe uptake into biomass. likely from stabilized dissolved Fe³⁺, with variable eolian lithogenic influences. Layer (II) extends between the oxycline and the chemocline at \sim 12 m and is dominated by partial Fe²⁺_{aq} oxidation on approach to the oxycline, with the formation of variably isotopically heavy Fe³⁺-bearing particles. Layer (III) underlies the chemocline and is defined by Fe²⁺ phosphate (vivianite) and carbonate saturation and precipitation under anoxic, Fe²⁺_{aq}-rich conditions with little Fe isotopic fractionation. The ice-covered winter water column features more homogenous Fe chemistry above the chemocline, which we attribute to seasonal homogenization of Layers (I) and (II), with suppressed ferric particle formation. Authigenic Fe minerals with non-crustal (light) Fe isotopic compositions only appreciably accumulate in sediments in Deming Lake underlying the chemocline. All sediments deposited above 12 m appear crustal in their Fe isotopic, Mn/Fe, and Fe/Al ratios, likely revealing efficient reductive dissolution of Fe³⁺-bearing lake precipitates and remineralization of Fe-bearing biomass. We find limited fractionation of Fe isotopes in the icecovered water column and suggest this provides evidence that substantial delivery of oxidants is required to generate highly fractionated Fe isotopic compositions in Sturtian Snowball era IFs. By comparing Fe isotopic and Mn/Fe fractionation trends in the different Deming Lake layers, we also suggest that correlations between these two parameters in giant early Paleoproterozoic IFs requires the simultaneous deposition of multiple authigenic phases on the ancient seafloor. Finally, high-precision triple Fe isotopic analyses of dissolved Fe impacted by extensive oxidation near the Deming Lake oxycline reveal that the slope of the mass fractionation law for natural, O₂-mediated Fe²⁺_{aq} oxidation is identical to those previously defined for both UV photo-oxidation, and for an array of highly fractionated Paleoproterozoic IFs.

31

32

33

34

35

36

37

38

39

40

41

42

43

44

45

46

47

48

49

50

51

52

53

54

55

56

57

58

59

60

61

1. Introduction

62

63

64

65

66

67

68

69

70

71

72

73

74

75

76

77

78

79

80

81

82

83

84

85

86

87

88

89

90

91

92

The evolution of redox conditions in Earth's oceans and atmosphere has been one of the key environmental controls on the evolution of life on our planet. The oceans featured dissolved iron (Fe) in its reduced, ferrous form (Fe²⁺_{aq}) as the dominant redox species for the majority of Earth history (Poulton and Canfield, 2011). Prior to the rise of molecular oxygen (O₂) in the atmosphere after the Great Oxidation Event (GOE) around 2.2-2.4 billion years (Ga) ago (Gumsley et al., 2017; Poulton et al., 2021) and for much of the ensuing Precambrian, Fe²⁺ was the most abundant inorganic redox-active species in the oceans (Poulton and Canfield, 2011). A lack of abundant dissolved O_2 or hydrogen sulfide (H₂S) in the deep oceans to remove Fe as insoluble Fe³⁺ oxides or Fe sulfide minerals enabled Fe²⁺_{aq} from seafloor hydrothermal and continental weathering sources to accumulate to high concentrations of perhaps 1000s of µg/L (Holland, 1984; Eroglu et al., 2018; Dauphas et al., 2024). The most striking evidence for high dissolved Fe²⁺_{aq} in the Precambrian oceans are iron formations (IFs), Fe- and Si-rich chemical sedimentary rocks that are found in sedimentary successions on all major Precambrian cratons and today host the largest economic Fe deposits (Bekker et al., 2010). The widespread and Fe-rich nature of IFs indicates that: i) the early oceans were anoxic and rich in reduced Fe²⁺_{aq}, the only Fe species that is soluble at high concentrations in seawater, in conditions that are defined as 'ferruginous' and ii) mechanisms existed in the early oceans to promote the voluminous precipitation of Fe minerals from the large marine Fe²⁺_{aq} pool. The modern-day mineral assemblages of IFs reflect long term diagenetic and metamorphic processes. Candidate precipitate phases include ferric oxyhydroxides, mixed-valence green rusts, Fe-rich carbonates, and predominantly Fe²⁺-bearing phyllosilicates (Halevy et al., 2017; Konhauser et al., 2017; Siahi et al., 2020; Rasmussen et al., 2021). These candidate IF precursor phases interact very differently with respect to dissolved nutrient elements (Robbins et al., 2016; Tostevin and Ahmed, 2023), and their formation requires vastly different chemical and redox conditions for formation. Better constraints on which of these minerals were the dominant IF precipitates are a key to unlocking myriad aspects of ocean biogeochemistry under a dominantly ferruginous redox state. Ferruginous conditions dominating the Precambrian also means that oxygenic phototrophs like cyanobacteria that ultimately fueled the rise of oxygen emerged against a backdrop of high dissolved Fe²⁺_{aq} in or at the boundaries of their habitat. As such, interpreting the geological record

of the earliest signs of oxygenic photosynthesis should be aided by a better understanding of the geochemical and isotopic imprints of cyanobacterial growth in high Fe conditions (Swanner et al., 2015a, 2017).

It is essentially impossible to study the biogeochemical cycling of Fe in ferruginous ocean conditions today because these environments do not exist in the modern oceans (Dauphas et al., 2024). Most of the global oceans are well-oxygenated such that the stable Fe species is highly insoluble Fe³⁺ that precipitates as amorphous oxyhydroxides rather than accumulating in solution (Millero, 1998). Where anoxic conditions are established in the modern oceans in sites of extremely high organic productivity and/or through the restriction and stratification of water masses, Fe²⁺_{aq} does not accumulate to the extent representative of early ferruginous oceans. This is because abundant dissolved sulfate in the modern oceans enables H₂S to accumulate at far higher levels than Fe²⁺_{aq} following anaerobic bacterial sulfate reduction, either in 'euxinic' water columns featuring free H₂S, or in sedimentary porewaters. In turn, H₂S efficiently removes all of the less abundant Fe to insoluble sulfide minerals such as pyrite (FeS₂) (Raiswell et al., 2018).

In the absence of a direct marine analog for early ferruginous oceans, most of our understanding of natural ferruginous environments comes from the study of meromictic lakes i.e., lakes that are vertically stratified with a deepest water layer (monimolimnion) that does not mix with shallower waters (Swanner et al., 2020). Such lakes exist around the world in settings where physical properties promote stratification and isolation of the monimolimnion from the oxygenated atmosphere or photosynthetic oxygen production. Ferruginous conditions can be established in the monimolimnion of such lakes where local geochemical sources promote a higher abundance of dissolved Fe than sulfur species. There is a rich history of geochemical studies of meromictic lakes and their underlying sediments, many of which have been motivated by the early Earth questions detailed above. In particular, meromictic lakes have become popular natural laboratories for understanding stable Fe isotope geochemistry, using observed systematics in ferruginous water columns and sediments as analogs for interpreting the vast database of Fe isotope analyses made of IFs and other Fe-rich Precambrian sediments (Malinovsky et al., 2005; Teutsch et al., 2009; Busigny et al., 2014; Ellwood et al., 2019; Yang et al., 2022; K. Liu et al., 2022). A focus of those studies has been on dissolved (and to a lesser extent, particulate) Fe isotopic compositions developed close to the transitional boundary layer or 'oxycline' between oxygenated near-surface waters and Fe²⁺_{aq}-rich deeper waters, where a large amount of Fe²⁺_{aq} oxidation takes place. This

natural oxidation process at the top of an anoxic deep water mass mimics the most widely cited model for the genesis of IFs (Konhauser et al., 2017). In particular, the formation of isotopically heavy ferric oxyhydroxides, which leads to isotopically light dissolved Fe near the redoxcline, has been used as evidence to support both the oxide-precursor origin of IFs (which are often isotopically heavy) and a mass-balance interpretation of other, Fe isotopically light Precambrian sediments such as Archean pyrites (Dauphas et al., 2004b; Rouxel et al., 2005; Planavsky et al., 2012).

Considerably less attention has been given to Fe isotopic systematics in the monimolimnion of meromictic ferruginous lakes where redox processes play little role in Fe mineral precipitation and drive muted fractionation. Similarly, the interactions of dissolved Fe with biology inhabiting the shallowest epilimnion and or/oxycline of these lakes, where dissolved and particulate Fe abundances are typically low enough to present analytical challenges, have received limited attention (Ellwood et al., 2019; K. Liu et al., 2022). All of these depth regimes offer important calibration points for understanding Fe isotopic systematics of ancient chemical sediments beyond those formed through simple oxidation-reduction processes. Furthermore, prior studies have not always analyzed the coupled Fe isotopic systematics of dissolved and particulate Fe, even near to lake oxyclines. To understand the Fe chemical and isotopic interactions between dissolved and particulate phases in a ferruginous water column in more detail, including processes occurring away from the redoxcline, we conducted three field sampling campaigns at Deming Lake, Minnesota (MN), USA.

2. Deming Lake, USA

Deming Lake is a small meromictic lake in Itasca State Park, MN, USA (Fig. 1). With a surface area of ~50,000 m² and a maximum depth of >17 m in a small kettle-hole depression near its center, Deming Lake has a relative depth (depth divided by average lake diameter) of ~8 %. Its small surface area makes Deming Lake susceptible to stratification (Gorham and Boyce, 1989; Swanner et al., 2020, 2023a) because wind mixing cannot act on a large enough area to drive vertical mixing of the entire water column depth. Surface mixing by wind is further hindered by the surrounding thickly wooded and steeply elevated margins of the lake (Lascu et al., 2012). The lake is thermally stratified in the spring to fall months, but undergoes freezing and thermocline collapse during the winter, enabling vertical mixing of the epilimnion and metalimnion (Swanner

et al., 2023a). However, a permanent chemocline separating high specific conductance deeper waters beneath 11-13 m depth has been recognized for several decades (Baker and Brook, 1971; Church et al., 1989; Reiter et al., 1998; Lascu et al., 2012; McLauchlan et al., 2013; Swanner et al., 2023b), and this chemical stratification is strong enough to prevent seasonal mixing in the deepest several meters of the lake.

The monimolimnion of Deming Lake is extremely rich in dissolved Fe²⁺_{aq}, on par with some other well-characterized ferruginous meromictic lakes such as Lac Pavin, France, and Brownie and Canyon Lakes, USA (Busigny et al., 2014; Lambrecht et al., 2018; Swanner et al., 2020). Stabilization of a high dissolved Fe²⁺_{aq} concentration in the lake is enabled by the lack of interaction between deep waters and the oxygenated atmosphere, by a lack of sulfur in the system that may generate H₂S, and by the likely input at depth of Fe-rich carbonate-bicarbonate-type groundwaters that are typical for the region (Megard et al., 1993). Deming Lake has minimal surface inflows, but a short water residence time (~90 days), implicating shallow groundwater as a major component of the water budget (Swanner et al., 2023a). Various Fe-rich groundwater-fed springs are found in the nearby surrounding areas of Itasca State Park (Swanner et al., 2023a).

A key feature of Deming Lake's biogeochemistry is the presence of a subsurface chlorophyll maximum layer (SCML), a turbidity maximum at 5 m to 6.5 m depth created by abundant Chlorophyll-a-containing Cyanobacteria inhabiting a depth coincident with the summer thermocline (Baker and Brook, 1971; Swanner et al., 2023a). This SCML is particularly pronounced during the summer months, but despite the abundance of Chlorophyll-a, likely consumes O₂ such that the SCML is coincident with the oxycline (Swanner et al., 2023a). This zone offers the potential to observe the isotopic effect of interactions between abundant Cyanobacteria and water column Fe.

Unlike some other meromictic ferruginous lakes that have been the subject of stable Fe isotopic study (Busigny et al., 2014; Ellwood et al., 2019; Yang et al., 2022), H₂S never appreciably accumulates in Deming Lake, making it an ideal natural laboratory for studying Fe isotopic fractionation where Fe²⁺_{aq} is the dominant redox species at all depths beneath the oxycline. We conducted a comprehensive Fe isotopic and geochemical survey of the Deming Lake water column, sediments, and various putative Fe sources to the lake, to address the following questions:

• What are the major sources and sinks of Fe in Deming Lake, and how do these fluxes maintain strongly ferruginous conditions at depth?

- Does biomass at the oxycline have a distinctive Fe isotopic signature, particularly within
 the highly productive SCML?
 - How do seasonal mixing of the epilimnion and metalimnion and establishment of winter ice cover impact ferruginous lake chemical profiles and Fe export?
 - Can targeted studies of coupled dissolved and particulate Fe geochemical systematics in Deming Lake refine our understanding of the ancient geochemical record?

3. Methods

3.1. Sampling Procedures

Sampling and *in situ* sensor analysis during May and August 2022 was conducted from an anchored boat at the deepest location of the lake, approximately 20 m water depth. Sampling of the ice-covered lake in March 2023 was conducted on foot using the same sampling and sensor equipment, through holes cored in the lake ice. A Yellow Springs Instruments (YSI) ProDSS was lowered on a depth-calibrated cable and used to record depth (m), temperature (°C), pH, oxidation/reduction potential (ORP; in mV), dissolved O₂ (mg/L), turbidity (Formazin Nephelometric Units or FNU), specific conductance (Sp Cond; in Microsiemens Per Centimeter or μS/cm), and total dissolved solids (TDS; in mg/L). These are reported for each sampling date in Table S1. All samples for water column dissolved and particulate major and minor elements and Fe isotopes were collected using a Proactive Mini Monsoon pump with a low-flow controller that was attached to vinyl tubing and a power cable marked with 0.5 m depth increments. As the pump was lowered to each new sampling depth, the pump was run for a period of time measured to be long enough to ensure that shallower-derived waters were flushed out and waters at the depth of interest were flowing out of the sampling tubes, before sample collection was initiated.

Waters were filtered in-line for Fe isotopic analysis using Millipore[®] SterivexTM-GP pressure filter units with Luer-Lok connections and 0.22 μ m PES membrane filters that were purged by syringe, sealed with parafilm and frozen until leaching and analysis. Water samples for Fe isotope analyses were collected in 1 L Nalgene HDPE bottles precleaned with 10 % trace metal-grade HCl. At some depth levels, we report dissolved but not particulate analyses where additional dissolved Fe analyses were made possible with excess water samples collected for trace metal analysis that contained sufficiently high dissolved Fe. SterivexTM filters were also used to collect materials for particulate manganese (Mn) oxide concentration (pMn_{ox}) measurements by passing

150 mL and stored identically to filters collected for particulate Fe isotopes. Waters for trace metal analysis were filtered with removable 25 mm diameter 0.22 µm PES membrane filters placed in acid-cleaned polypropylene Swinnex filter holders that were removed and immediately placed in cleaned Savillex Teflon reactors until leaching and analysis. Filtered waters for dissolved trace metal samples were collected in 50 mL centrifuge tubes that were precleaned with 10 % trace metal-grade HCl. All lake water samples were acidified at the end of the sampling day using Optima grade HCl to a molarity of 0.4 M.

A core of ice from the center of the lake was obtained in March 2023 using a Kovacs Mark V coring system. The core barrel extracts a 14 cm diameter ice core and returned a ~40 cm-long ice core topped with ~5 cm of snow cover. This core was transported to the field station in a clean plastic bag. Visual examination of the core revealed the presence of 3 layers: a ~5 cm unconsolidated snow layer at the top; a ~20 cm opaque layer identified as deriving from snow and referred to hereafter as 'snow ice'; and a ~20 cm transparent layer identified as frozen lake water or 'lake ice'. The outer layer of the ice core was washed liberally with methanol and Milli-Q water prior to sampling, and all samples from the ice core specifically avoided the outer surface of the core that was in direct contact with the coring system. Five discrete sample layers, one from the unconsolidated snow and two each from the snow ice and lake ice, were collected from this core by manual separation with a ceramic chisel. These approximately 400 mL samples were melted in acid-cleaned 500 mL Savillex Teflon reactors prior to transportation back to Woods Hole Oceanographic Institution (WHOI).

Several sites around Itasca State Park that are potentially representative of Fe input sources to Deming Lake were sampled in August 2023. Water from a bog on the southeast margin of Deming Lake represented surface inputs, and water from springs along Nicollet Creek, and from Elk Springs on the margins of Elk Lake represent regional groundwaters. These were sampled with acid-cleaned syringes fit with 0.45 and 0.22 µm syringe filters, waters were acidified at the University of Minnesota Itasca Biological Station, and both filters and waters were returned to Iowa State University and shipped to WHOI for analysis. Both spring sites feature rusty surface mineralization and are likely Fe-rich due to anoxic subsurface conditions (Swanner et al., 2023a).

Sediment samples from the lake bottom were collected from the boat in May 2022. Ten samples capturing a few centimeters depth of the upper sediment layer were collected from depths between 1 m and 16.5 m depth along a transect from the northern shore and slope of the lake using a Wildco

Ekman dredge. Additionally, one gravity core was collected at 4 m depth that yielded 7 discrete samples from depths between 0 and 7 cm into the sediment column. All sediment samples were transferred into acid-cleaned 50 mL centrifuge tubes aboard the boat and frozen on return from the field for transportation. These samples were subsequently freeze-dried on return to WHOI using a benchtop freeze dryer with a Polytetrafluoroethylene coated stainless steel collector (Labcono FreeZone). Once dry, each sample was ground to a fine powder using a FRITSCH Mini-Mill Pulverisette 23 with zirconium oxide bowl and grinding balls.

3.2. Particulate Mn Oxide Analysis

Particulate Mn oxide abundance data were generated using the same methodologies employed in Gadol et al. (2023). On return of the filter cartridges to the laboratory at WHOI, pMn_{ox} abundances were quantified using the leucoberbelin blue (LBB) assay with a permanganate standard curve (Altmann, 1972; Oldham et al., 2015). SterivexTM cartridge filters containing lake particles were filled with 2 mL LBB at a concentration of 0.004% in 0.1% acetic acid and then resealed with Parafilm. After approximately two hours the liquid extract was removed, and absorbance was measured at 620 nm on a UV-Vis spectrophotometer.

3.3. Sample Digestion and Elemental Analysis

All sample preparation was performed in the NIRVANA class 100 clean laboratory at WHOI unless otherwise indicated. All reagents used through all preparation steps were double distilled or purchased at Optima grade, and sample preparation steps made use of Savillex Teflon reactors unless otherwise stated. Dissolved elemental compositions were determined directly from acidified water samples, while particulate, ice, and sediment samples underwent further preparation steps prior to elemental analysis.

Filtered lake particles for elemental analysis were leached from the PES membrane filters originally mounted on the Swinnex holders overnight in 0.6 M HCl at 80 °C in a volume of acid calibrated to be sufficient to leach all trace metals from filters of a given surface area, following the methodology of <u>Bishop and Wood (2008)</u>. Ice core samples were melted in 500 mL Savillex Teflon reactors at the University of Minnesota Itasca Biological Station on the same day of collection and evaporated to dryness on a hotplate at WHOI. Dried ice samples were reconstituted in 10 mL of concentrated HNO₃, transferred to smaller reactors, and dried down. To ensure

complete transfer of materials from the 500 mL reactors, these were sequentially refluxed with aqua regia (3:1 concentrated HCl:HNO₃) and 1:1 HNO₃:H₂O₂ overnight and each time the acids were transferred into the smaller volume reactors. Samples were then redried and digested in 1:1 concentrated HNO₃:H₂O₂ several times to dissolve particles, then reconstituted in 5 mL 2 % HNO₃. For sediments, approximately 50 mg of bulk powders were weighed into Savillex Teflon reactors and digested in 2 mL concentrated HF + 1 mL concentrated HNO₃. These samples were then sequentially dried down and digested in aqua regia followed by 1:1 concentrated HNO₃:H₂O₂ to destroy organics. Samples were dried down, fluxed in concentrated HNO₃, redried, and constituted in 5 mL of 2 % HNO₃.

Aliquots of all sample types, constituted in dilute HNO₃, were analyzed for their full metal element concentrations using a Thermo Fisher iCAP-Q inductively coupled plasma mass spectrometer (ICP-MS) at the WHOI Plasma Facility following dilution in 2 % HNO₃. Indium (In) was added to samples at a concentration of 1 ng/g prior to analyses to monitor and correct for instrument drift and matrix effects by normalizing to In intensities. Concentrations were calculated using a five-point calibration curve obtained by fitting of ion beam intensities measured for serial dilutions of a gravimetrically prepared multi-element standard in an artificial seawater matrix. The relative standard deviation (RSD) for five measurements of each sample was ~10% on the iCAP-Q. The accuracy and precision of similar concentration measurements on iCAP-Q at WHOI have previously been determined to be \pm 5-10 % (1SD) based on comparison with USGS reference materials AGV-1, AGV-2, BHVO-1, BHVO-2, BIR-1, and BCR-2 prepared and analyzed as unknowns during earlier runs (Jochum et al., 2016; Shu et al., 2017).

After elemental analysis provided Fe concentration data that indicated what sample quantities were required for Fe isotopic analysis, all target samples were prepared in a similar manner to eventually constitute them in 6 M HCl for column chemistry purification. Aliquots of acidified lake and spring water intended for Fe isotopic analysis (between 1 mL and 1 L) were dried down on a hotplate for digestion of organics and reconstitution in small acid volumes. The dried samples were sequentially digested in aqua regia, redried and digested in 1:1 concentrated HNO₃: H₂O₂ to destroy dissolved organic matter. Filtered particulate Fe was extracted for Fe isotopic analysis by leaching Sterivex[™] (or in the case of spring samples, removable PES membrane) filters overnight at 80 °C in 6 M HCl. The leachates were sequentially dried down and digested in aqua regia followed by 1:1 concentrated HNO₃:H₂O₂ to destroy organics. After elemental analysis determined

that concentrations of Fe in each individual depth layer sampled in the ice core were too low for Fe isotopic analysis, the three uppermost samples (1 snow sample and the 2 snow ice samples) were combined to provide a bulk isotopic sample of surficial flux accumulation on the ice cover. After an aliquot was taken for elemental analysis, bulk sediment digest samples were dried down. After necessary digestion steps, all sample types (waters, particles, ice, sediment digest) were dried down, fluxed overnight in concentrated HCl to convert the Fe to chloride form, then redried and reconstituted in 6 M HCl prior to Fe purification.

3.4. Iron Purification and Isotopic Analysis

Iron was purified using established column chemistry procedures detailed in the literature (Dauphas et al., 2004a, 2009; Craddock and Dauphas, 2011b). Samples in 6 M HCl were loaded onto 1 mL of AG1-X8 anion exchange resin in disposable Biorad PolyPrep columns. The resin was pre-cleaned with MilliQ water, 1 M HNO₃ and 0.4 M HCl and preconditioned with 2 mL of 6 M HCl. After sample loading, matrix elements including Cr and Ni were eluted in 8 mL of 6 M HCl. Sample Fe was then eluted in 9 mL 0.4 M HCl. To ensure complete purification of samples, the Fe solution was dried down, organics leached off the column were destroyed using aqua regia followed by HNO₃ + H₂O₂ digestion, and the sample was refluxed in HCl then reconstituted in 0.5 mL of 6 M HCl, for the column procedure to be repeated. Purified samples were then dried down, fluxed overnight in 1 mL of concentrated nitric acid to convert them to nitrate form, then redried and taken up in 5 ml of 2 % HNO₃ for mass spectrometry. Procedural blanks were typically 20 ng of Fe which is negligible in comparison to the mass of sample Fe, between 5 μg and 500 μg.

Iron isotopic compositions were measured in medium-resolution mode on a Thermo Scientific Neptune multi-collector inductively coupled plasma mass spectrometer (MC-ICP-MS) at WHOI. Platinum coated 'A' sampler and 'H' skimmer cones were used for improved sensitivity and stability. A quartz cyclonic spray chamber was used to introduce sample solutions containing 1 μg/g Fe in 2 % HNO3, giving a signal of ~10 V on ⁵⁶Fe, the most abundant Fe isotope. Intensities on ⁵⁴Fe⁺, ⁵⁶Fe⁺, ⁵⁷Fe⁺, and ⁵⁸Fe⁺ were measured simultaneously, in addition to ⁵³Cr⁺ and ⁶⁰Ni⁺, which were used to correct for ⁵⁴Cr⁺ and ⁵⁸Ni⁺ interferences on ⁵⁴Fe⁺ and ⁵⁸Fe⁺, respectively, using the exponential law. These corrections always had negligible impact on calculated isotopic ratios. Iron was measured on flat-topped peak shoulders to the low-mass side of molecular interference peaks resulting from argide ions (⁴⁰Ar¹⁴N⁺, ⁴⁰Ar¹⁶O⁺, ⁴⁰Ar¹⁶O¹H⁺, and ⁴⁰Ar¹⁸O⁺). Standard-sample

bracketing was used to correct Fe isotopic ratios for instrumental mass fractionation. All solutions were prepared using the same batch of 2 % HNO₃, and signal intensities on 56 Fe in sample and standard solutions were matched to within <5 % prior to isotopic analysis. Iron isotope ratios are reported in δ^x Fe notation, the per mil deviation of x Fe/ 54 Fe in the sample relative to IRMM-524, which has an identical isotopic composition to IRMM-014, where:

346
$$\delta^{x}$$
Fe (‰) = $[({}^{x}$ Fe $/{}^{54}$ Fe)_{sample} $/({}^{x}$ Fe $/{}^{54}$ Fe)_{IRMM-014} - 1] × 1000, (1a)

or in the logarithmic notation in which mass fractionation laws (MFLs) are strictly straight lines:

348
$$\delta^{\text{tx}} \text{Fe (\%)} = 1000 \ln[(^{\text{x}} \text{Fe}/^{54} \text{Fe})_{\text{sample}}/(^{\text{x}} \text{Fe}/^{54} \text{Fe})_{\text{IRMM-014}}], \tag{1b}$$

Mass dependent fractionation was confirmed by checking the relationship between δ^{156} Fe and δ^{157} Fe values, which in all cases fell well within error of the expected MFL (δ^{156} Fe = $\theta^{56/57} \times \delta^{157}$ Fe where the slope $\theta^{56/57} \approx 2/3$). We note that δ^{56} Fe and δ^{156} Fe are functionally identical at the scale of natural variations we observe, but δ^{156} Fe is strictly the correct formulation when discussing mass fractionation laws as truly linear arrays. The IF-G, BHVO-2, and AGV-2 geostandards were processed through the same preparation protocols as unknown samples, and their δ^{56} Fe values always agreed with the recommended values within error (Table S2) (Craddock and Dauphas, 2011b). Here and elsewhere unless otherwise stated, uncertainties are given at the 95% confidence interval level following 5 repeat standard-sample bracket measurements (Dauphas et al., 2009), for water column (Table S3), spring and bog (Table S4), and sediment (Table S5) samples.

3.4.1 High-precision Triple Fe Isotopic Analysis

Selected dissolved Fe samples were also analyzed at high precision to determine the precise value of the slope, $\theta^{56/57}$, for the MFL associated with Fe²⁺ oxidation in Deming Lake. Previous studies have shown that the value of $\theta^{56/57}$ can vary slightly in nature and may be used to resolve different Fe cycling pathways in the ancient sedimentary record (Nie et al., 2017; Heard et al., 2020).

The value of $\theta^{56/57}$ is determined by measuring parts per 10^4 departures, ϵ^{156} Fe, from the expected 56 Fe/ 54 Fe ratio on a reference MFL for a given 57 Fe/ 54 Fe ratio, which we express here as:

$$\epsilon^{156} \text{Fe} = (\delta^{156} \text{Fe} - \theta^{56/57}_{\text{Reference}} \times \delta^{157} \text{Fe}) \times 10. \tag{2}$$

369 The ϵ'^{56} Fe values were initially calculated as

370
$$\epsilon'^{56} \text{Fe}_{\text{exp}} = \ln \left[\left({^{56} \text{Fe}} / {^{54} \text{Fe}} \right)_{\text{sample}}^{*} / \left({^{56} \text{Fe}} / {^{54} \text{Fe}} \right)_{\text{std}}^{*} \right] \times 10^{4},$$
 (3)

where the * indicates that ratios were corrected for mass fractionation by internal normalization to a fixed ${}^{57}\text{Fe}/{}^{54}\text{Fe}_{std}$ ratio of 0.362549, the value of IRMM-014. This correction was made along the exponential law with ${}^{66/57}_{exp} = 0.672$, using the equation:

374
$$\ln({}^{i}\text{Fe}/{}^{54}\text{Fe})^{*}_{\text{sample, corrected}} = \ln({}^{i}\text{Fe}/{}^{54}\text{Fe})_{\text{sample, measured}} - \ln\frac{({}^{57}\text{Fe}/{}^{54}\text{Fe})_{\text{sample, measured}}}{({}^{57}\text{Fe}/{}^{54}\text{Fe})_{\text{fixed reference}}} \frac{\ln(m_{i_{\text{Fe}}}/m_{54_{\text{Fe}}})}{\ln(m_{57_{\text{Fe}}}/m_{54_{\text{Fe}}})}.$$
375

Subsequently, data were renormalized to make the high-temperature equilibrium limit law with $\theta^{56/57}_{eq} = 0.678$ the reference law, following conventional presentations of these datasets:

378
$$\epsilon'^{56} \text{Fe}_{\text{eq}} = \epsilon'^{56} \text{Fe}_{\text{exp}} - 10 \times (0.678 - 0.672) \times \Delta \delta'^{57} \text{Fe}.$$
 (5)

- The 'measured' slope of the MFL expressed in the Deming Lake water column can be determined by taking the slope of ϵ^{156} Fe vs. δ^{157} Fe and using the relationship:
- $\Delta \epsilon^{156} Fe_{eq} = (\theta^{56/57}_{Measured} 0.678) \times \Delta \delta^{57} Fe \times 10.$

In practical terms, total variation of ϵ^{156} Fe values is so small that measurements require far higher precision than achievable with routine Fe isotope analytical protocols. To achieve the necessary precision, measurements were made via standard-sample bracketing using the same mass spectrometric setup as described above, with the following modifications: Sample solutions were prepared at 10 µg/g Fe, analyzed in ~20 standard sample brackets, and sample and standard intensities were matched to within 1 % on the 56 Fe signal. This specific analytical protocol follows that of Hopp et al. (2022), which improved the methods employed in earlier low temperature applications of triple Fe isotope measurements (Nie et al., 2017; Heard et al., 2020). The geostandards IF-G and BHVO-2 were analyzed using the same methods during this measurement session and produced ϵ^{156} Fe values in agreement with those published in the literature (Table S6) (Nie et al., 2017; Heard et al., 2020; Hopp et al., 2022).

3.5 Mineral Saturation Calculations

Mineral saturation indices for the precipitation of vivianite and siderite were calculated for selected depths in the monimolimnion using Geochemist's Workbench (Bethke, 2022) incorporating cation-anion data, carbonate alkalinity, and sonde measurements of dissolved O₂ and pH from August 2023. As discussed in the **Results**, geochemistry of the monimolimnion is observed to be seasonally stable and thus, while carbonate alkalinity data are unavailable for our earlier sampling

dates, the results of mineral saturation calculations are anticipated to be representative of chemistry in this layer throughout the duration of our study.

4. Results

In addition to Figures, all data are available in Tables S1-7 in the Supplementary Online Material.

- 4.1 Water Column Physical Properties, pH, and O₂
- The full list of parameters analyzed with *in situ* YSI sensors have been published in an openaccess repository (Swanner et al., 2023b). Temperature, turbidity, pH and dissolved [O₂] profiles are shown in Table S1 and Figure 2.

- *4.1.1 May 2022*
- The upper 2 m of the epilimnion is well-mixed with a temperature of ~15 °C, a thermocline between 2 m and 6 m, and a mixolimnion temperature of to 4.3 °C and monimolimnion temperature of 5 °C (Fig. 2A). Turbidity increases from 1.7 FNU at the lake surface to 9.8 FNU at 16 m depth, with local maxima at 3.5 m and 6.5 m depths (Fig. 2B). Lake pH can be divided into three distinct intervals of 8.3 at 0-2 m, 6.8 at 4-10 m, and 6.3 at 12-16 m, with transitions between these intervals (Fig. 2C). Surface dissolved O₂ concentration (dO₂) is 14.1 mg/L, there is a subsurface maximum at of 16.9 mg/L at 2 - 2.5 m, and dO₂ sharply declines between 2.5 and 5 m depth, below which no O₂ is detected (detection limit: 0.01 mg/L) (Fig. 2D).

- 421 4.1.2. August 2022
 - The upper 3 m of the epilimnion is well-mixed with a temperature of ~23 °C, a thermocline between 3 m and 8 m to 4.7 °C (Fig. 2E), a mixolimnion temperature of 4.5 and monimolimnion temperature of 5 °C. Turbidity increases from 0.7 FNU at the lake surface to 8.9 FNU at 16 m depth, with sharp local maxima of 6.8 and 14.1 FNU at 4 m and 6 m depths (Fig. 2F). Lake pH Is 7.8 in the upper 3 m, peaks to 8.6 at 3.5 m, declines through a local minimum of 6.7 at 5.5 m, then gently declines to 6.3 at 16 m (Fig. 2G). Surface dO₂ is 8.6 mg/L, there is a sharp subsurface maximum at of 16.6 mg/L at 3.5 m depth, with dO₂ sharply declining between 3.5 and 6 m depth, below which no O₂ is detected (Fig. 2H).

4.1.3. March 2023

The March 2023 water column is overlain by ~40 cm of ice cover, and features an inverted temperature profile with 0.4 °C just beneath the ice cover, increasing to 5 °C at 17 m, with the steepest temperature gradient occurring in the upper 4 m (Fig. 2I). Turbidity is uniformly 2.1 to 2.7 FNU in the upper 10 m of the water column and increases at greater depths to 10.2 FNU at 17 m (Fig. 2J). Water pH is 6.6 just below the ice surface, increases gently to 6.9 at 8 m depth, then decreases again to 6.4 at 17 m (Fig. 2K). dO₂ reaches 5.5 mg/L just below the ice cover and declines to below detection levels within the upper 2.5 m of the water column (Fig. 2L).

4.2. Water Column Fe, δ^{56} Fe, Mn Oxide, and Mn/Fe Systematics

Water column dissolved and particulate Fe concentrations (dFe and pFe, where throughout, dX and pX will denote the dissolved and particulate concentrations for element X), δ^{56} Fe (where $d\delta^{56}$ Fe and $p\delta^{56}$ Fe denote dissolved and particulate values), and Mn/Fe data are shown in Table S3 and Figure 3. We define three major Fe cycling layers within the water column, which are shown schematically in Figure 4.

- I) Layer (I) encompasses the epilimnion and the part of the metalimnion above the base of the oxycline. It features low dFe, and has δ^{56} Fe, Mn/Fe, and pFe that are variable with depth and season, particularly towards the base of the oxycline.
- II) Layer (II) extends from the base of the seasonally mobile oxycline to the chemocline, defined by a sharp increase in specific conductance at \sim 12 m depth that separates the metalimnion from the monimolimnion (Swanner et al., 2023a). Layer (II) features the sharpest changes in particulate and dissolved Fe, δ^{56} Fe, and Mn/Fe with depth.
- III) Layer (III) is the monimolimnion that extends from 12 m to the maximum sampling depth of 16 to 17 m near the lake bottom. It features high dFe and almost invariant dissolved and particulate δ^{56} Fe and Mn/Fe with depth. The Fe concentration, δ^{56} Fe, and Mn/Fe of the dissolved and particulate phases are essentially identical for May 2022, August, 2022, and March 2023.

4.2.1 May 2022

Layer (I): dFe is between 12 and 15 μg/L and pFe between 33 and 105 μg/L (Fig. 3A). $d\delta^{56}$ Fe ranges from -0.28 to -0.08 ‰ and $p\delta^{56}$ Fe ranges from -0.72 to -0.46 ‰ (Fig. 3B). Dissolved Mn is

below detection limits above 4 m, and dMn/dFe increases sharply from 1.1 to 24 mol/mol between 462 4 and 5 m depth, while pMn/pFe ranges between 0.38 and 0.85 mol/mol (Fig. 3C). Almost all 463 464 depths at which pMn_{ox} is measured fall within Layer (I), with surface values of $\sim 7.5 \mu g/L$ and a subsurface peak of 66 µg/L at 4.5 m depth (Table S3).

Layer (II): Here, dFe increases dramatically beneath the oxycline from 71 µg/L at 6 m depth to 466 5.0 mg/L at 10 m depth, to 39 mg/L at 12 m, while pFe ranges from 50 to 299 µg/L (Fig. 3A). 467 Dissolved δ^{56} Fe is at a minimum of -2.06 % just below the oxycline at 6 m, increasing to -0.41 % 468

at 12 m, while $p\delta^{56}$ Fe ranges from -0.51 to 0.64 % (Fig. 3B). Dissolved Mn/Fe increases from 0.050 to 9.4 mol/mol with decreasing depth, while pMn/pFe ranges from 0.02 to 0.083 mol/mol

(Fig. 3C). Particulate Mn oxide measured at 7 and 8 m depth is around 0.5 µg/L (Table S3). 471

Layer (III): dFe ranges from 39 to 67 mg/L and pFe ranges from 180 to 390 µg/L (Fig. 3A). 472 $d\delta^{56}$ Fe ranges from -0.40 to -0.25 % and p δ^{56} Fe ranges from -0.30 to -0.07 % (Fig. 3B). dMn/dFe 473 ranges from 0.030 to 0.042 mol/mol and pMn/pFe ranges from 0.025 to 0.039 mol/mol (Fig. 3C). 474

Triple Fe isotope data for the May 2022 dissolved Fe pool between 6 and 16 m water depth (below the oxycline) define a mass fractionation array with a slope of 0.0077 ± 0.0100 in ϵ^{56} Fe_{exp} vs. δ^{157} Fe space, which corresponds to a value of 0.6788 ± 0.0010 for the slope of the MFL, $\theta^{56/57}$ (Fig. 5). All measured ϵ'^{56} Fe_{exp} values of the dissolved Fe pool were slightly negative, and the ϵ^{156} Fe_{exp} vs. δ^{157} Fe mass fractionation array for May 2022 dissolved Fe pool has a slightly negative intercept of ϵ'^{56} Fe_{exp} = -0.0275 ± 0.0139 .

481

482

483

484

485

486

487

488

489

490

491

465

469

470

475

476

477

478

479

480

4.2.2. August 2022

Layer (I): dFe is between 2.1 and 5.8 μ g/L and pFe between 33 and 47 μ g/L (Fig. 3D). $d\delta^{56}$ Fe ranges from -0.24 to 0.18 % and p δ^{56} Fe ranges from -0.94 to -0.47 % (Fig. 3E). dMn/dFe ranges from 0.21 to 414 mol/mol, while pMn/pFe ranges between 0.55 and 3.4 mol/mol (Fig. 3F). All depths at which pMn_{ox} is measured fall within Layer (I), with values of between 12 and 33 µg/L (Table S3).

Layer (II): Here, dFe increases dramatically beneath the oxycline from 870 μg/L at 6.5 m depth to 8.9 mg/L at 10 m depth, to 36 mg/L at 12 m, while pFe ranges from 62 to 349 µg/L (Fig. 3D). Dissolved δ^{56} Fe is at a minimum of -1.37 % just below the oxycline at 6 m, increasing to -0.35 % at 12 m, while p δ^{56} Fe ranges from 0.07 to 0.37 % (Fig. 3E). Dissolved Mn/Fe increases from 0.040

- to 6.5 mol/mol with decreasing depth, while pMn/pFe ranges from 0.036 to 0.11 mol/mol (Fig.
- 493 3F).
- 494 Layer (III): dFe ranges from 36 to 54 mg/L and pFe ranges from 164 to 252 μg/L (Fig. 3D).
- 495 $d\delta^{56}$ Fe ranges from -0.35 to -0.29 % and $p\delta^{56}$ Fe ranges from 0.03 to 0.05 % (Fig. 3E). dMn/dFe
- ranges from 0.032 to 0.040 mol/mol and pMn/pFe ranges from 0.025 to 0.035 mol/mol (Fig. 3F).
- 497
- 498 *4.2.3. March 2023*
- Layers (I) to (III) are less well-defined in the ice-covered March 2023 water column, but for
- simplicity we still place the layer boundaries at base of the oxycline, and the 12 m depth level.
- 501 *Ice Cover*: The pooled sample of the ~20 cm-thick snow-derived portion of the ice core has a
- δ^{56} Fe of -0.20 % (Fig. 5A), and an Mn/Fe of 0.21 mol/mol (Fig. 5B). The transparent lake water-
- derived ice layer contained insufficient Fe for an isotopic measurement.
- Layer (I): The oxygenated Layer (I) covers a very narrow (2 m) depth interval in the ice-covered
- lake, and only the upper two dissolved and particulate samples capture this layer. dFe is between
- 16 and 50 μg/L and pFe between 39 and 50 μg/L (Fig. 3G). $d\delta^{56}$ Fe ranges from -0.24 to -0.20 ‰
- and p δ^{56} Fe ranges from -0.91 to -0.86 % (Fig. 3H). dMn/dFe ranges from 0.60 to 0.89 mol/mol,
- while pMn/pFe ranges between 0.27 and 0.31 mol/mol (Fig. 3I). Particulate Mn oxide abundance
- is 5.5 μ g/L in waters immediately below the ice and peaks at 14 μ g/L at 2 m depth (Table S3).
- Layer (II): this layer features much less dramatic variations with depth than those observed in
- May and August 2022. dFe ranges from 129 to 760 μg/L, while pFe ranges from 12 to 314 μg/L
- 512 (Fig. 3G). Dissolved δ^{56} Fe is ranges from -0.97 to -0.35 ‰, while $p\delta^{56}$ Fe ranges from -0.66 to -0.15
- 513 % (Fig. 3H). Dissolved Mn/Fe ranges from 0.042 to 1.4 mol/mol, while pMn/pFe ranges from
- 514 0.025 to 0.39 mol/mol (Fig. 3I).
- Layer (III): dFe ranges from 36 to 61 mg/L and pFe ranges from 301 to 372 μg/L, except for an
- extremely low value of $2.3 \mu g/L$ (omitted from Figure 3) at 14 m that likely reflects a failure in
- sample filtration given that this depletion is seen in all elements (Fig. 3G). $d\delta^{56}$ Fe ranges from -0.35
- to -0.22 % and p δ^{56} Fe ranges from -0.36 to -0.30 % (Fig. 3H). dMn/dFe ranges from 0.031 to
- 519 0.042 mol/mol and pMn/pFe ranges from 0.025 to 0.34 mol/mol (Fig. 3I).
- 520
- 521 *4.3. Springs and Bog*

- For the Deming Lake bog, dFe is 120 to 680 μ g/L and pFe is 76 to 120 μ g/L (Table S4). Dissolved and particulate δ^{56} Fe are -0.57 to -0.56 ‰ and -0.59 to -0.29 ‰, respectively (Fig. 6A), and dMn/dFe is 0.06-0.13 mol/mol. No particulate sample for trace elements was analyzed (Fig. 6B). For the samples from Elk Spring, dFe is 7.4 to 7.7 mg/L and pFe is 150 to 510 μ g/L (Table S4). Dissolved and particulate δ^{56} Fe are -0.27 to -0.15 ‰ and -0.04 ‰, respectively (Fig. 6A). Dissolved and particulate Mn/Fe are 0.037 mol/mol and 0.015 mol/mol, respectively (Fig. 6B). For the samples from the spring near Nicollet Creek, dFe is 340 to 400 μ g/L and pFe is 750 to
- μ g/L (Table S4). Dissolved and particulate δ^{56} Fe are -0.77 to -0.74 ‰ and -0.85 to 0.75 ‰, respectively (Fig. 6A). Dissolved and particulate Mn/Fe are 0.33 to 0.38 mol/mol and 0.13
- mol/mol, respectively (Fig. 6B).

4.4. Lake Sediments

Selected bulk compositional information for the lake sediments collected along the shallow to deep transect in Deming Lake is presented in Table S5. Sediment samples are almost invariant with respect to Fe isotopes, both with depth in the lake or depth within the sediment column for the gravity core sample (Fig. 6A, B). Sediments from lake depths between 1 and 16.5 m have average δ^{56} Fe = 0.09 ± 0.09 % (2 SD), with individual values ranging from 0.00 % at 14 m depth to 0.15 % at 3 m depth (Fig. 6B). While there is a slight trend of decreasing δ^{56} Fe with increasing lake depth, most samples agree within individual measurement error bars. All core samples from 0-7 cm depth within a gravity core taken at 4 m lake depth have identical δ^{56} Fe within error, with an average value of 0.13 ± 0.03 % (2 SD; Fig. 6A). For reference, the bulk upper continental crustal value of δ^{56} Fe is 0.09 to 0.12 % (Dauphas et al., 2017; X.-M. Liu et al., 2022).

From 1 to 12 m depth, sediments feature mostly invariant Mn/Fe between 0.015 and 0.030 mol/mol with no systematic depth dependence, with elevated values of 0.057 mol/mol occurring at 14 m and 16.5 m depth (Fig. 6C). Most values are moderately elevated relative to the upper continental crust (UCC) value of 0.017 mol/mol (Taylor and McLennan, 1995). Sediments from 1-12 m depth feature Fe/Al within \pm 20 % of the UCC value of 0.21 mol/mol (Fig. 6D). At 14 to 16.5 m depth, Fe/Al sharply increases to 0.43 – 0.47 (Fig. 6D), which is approximately twice the crustal value.

5. Discussion

5.1. Iron Sources to Deming Lake

Deming Lake has no inlet or outlet streams, so its potential sources of Fe include eolian input, surface outflow from boggy areas surrounding the lake, and subsurface groundwater inflow (Lascu et al., 2012; Swanner et al., 2023a). Factors to consider when we assess the relative importance of these different inputs to the Fe budget of Deming Lake include direct measurements of the chemical and isotopic characteristics of material that might be representative of these fluxes, and the depth distribution of Fe in the water column. To compare source fluxes to the whole lake, we calculate column-averaged, volume- and dFe-weighted $d\delta^{56}$ Fe for the Deming Lake water column ($d\delta^{56}$ Fe_{column}) using numerical integration and depth-dependent volume estimates for Deming Lake from Swanner et al. (2023a);

$$d\delta^{56} Fe_{column} = \sum d\delta^{56} Fe(z) \times dFe(z) \times V(z) / \sum dFe(z) \times V(z),$$
 (6)

where $d\delta^{56}Fe(z)$, dFe(z), and V(z) are the $d\delta^{56}Fe$, dFe, and water volume within 0.5 m depth intervals in the lake, and summation was carried out over the full sampled lake depth. We find that the average of $d\delta^{56}Fe$, which accounts for the vast majority of all Fe in the lake, has essentially identical values of -0.34 ‰ in May 2022, -0.36 ‰ in August 2022, and -0.35 ‰ in March 2023 (Fig. 6A).

We can estimate the composition and flux of eolian inputs to Deming Lake from the material collected in the 'snow ice' portion of the ice core sampled in March 2023. This portion of the ice core derives from snowfall over the preceding winter months and therefore should have also accumulated all eolian particles deposited at the lake surface over this time. It is possible that eolian fluxes to Deming Lake change in the winter months compared to the rest of the year, but this integrated sampling provides a first order estimate of atmospheric Fe delivery. The snow ice layer was ~20 cm thick and has an Fe concentration of 75 ng/g, equating to 1.4 μ g Fe/cm². Assuming this Fe mass represents the accumulation of eolian material over ~4 months of ice coverage on the lake, this equates to an annual eolian Fe flux of ~4 μ g Fe/cm²/yr. Over the entire 5×10^8 cm² Deming Lake surface, this gives an estimated Fe mass delivery rate of 2,000 g Fe/yr with an Fe isotopic composition of δ^{56} Fe = -0.20 % (Fig. 6A). This mass delivery rate represents less than 0.1 % of the standing Fe reservoir in Deming Lake of 2.9-3.6×10⁶ g Fe, calculated using numerical integration. The δ^{56} Fe value of the eolian input is slightly more positive than the columnaveraged $d\delta^{56}$ Fe value for the lake waters and similar to the inferred authigenic sedimentary outputs from the lake, but the eolian flux is more than an order of magnitude lower than the inferred

authigenic Fe output flux from the lake (Section 5.4). Therefore, eolian input is unlikely to be the dominant Fe source to the lake.

584

585

586

587

588

589

590

591

592

593

594

595

596

597

598

599

600

601

602

603

604

605

606

607

608

609

610

611

612

613

The other possible surficial input of Fe to Deming Lake, runoff from nearby bogs, has a $d\delta^{56}$ Fe of approximately -0.6 % that is substantially isotopically lighter than the $d\delta^{56}$ Fe_{column} of ~-0.35 % (Fig. 6A), and inferred authigenic sedimentary outputs from the lake of -0.3 to -0.2 % (**Section 5.4**). While a mass flux from bog runoff is not possible to calculate, the low 100s of μ g/L dFe of the bog make this a less likely source of Fe to the lake.

Turning to subsurface Fe sources, groundwater inputs to Deming Lake are expected to be calcium, magnesium, and carbonate/bicarbonate-rich, consistent with the geochemistry of the lake water itself, due to reaction of waters with the calcareous Itasca moraine (Megard et al., 1993; Swanner et al., 2023a). While subsurface groundwater inflow sources of Fe into Deming lake were not directly sampled due to the lack of infrastructure, two nearby surface springs we sampled provide useful insights on their chemical attributes. Elk Spring and the Nicollet Creek Spring have the Ca-Mg systematics expected, as both feature high dCa (Elk ~90 mg/L, Nicollet ~55 mg/L) and dMg (Elk ~23 mg/L, Nicollet ~16 mg/L), and have dCa/dMg ratios of 2.1 to 2.4 mol/mol that agree with values for the Deming Lake water column (Table S7). The Fe geochemistry of Elk Spring provides a good match for the Deming Lake water column, with $d\delta^{56}$ Fe of -0.27 ± 0.11 to $-0.15 \pm$ 0.11 % overlapping with the water column averaged values and with the deep water dissolved δ^{56} Fe specifically (Figs. 3, 6A). Perhaps more importantly, the Elk Spring input flux closely resembles the δ^{56} Fe of the inferred authigenic sedimentary flux out of Deming Lake, discussed in detail in Section 5.4. The dMn/dFe ratio of Elk Spring water of 0.037 mol/mol (Fig. 6B) is also in very good agreement with deep water dMn/dFe ratios in Deming Lake (Fig. 3). The vast majority of Fe and Mn in the Elk spring samples was measured in the dissolved rather than the particulate phase, so these water samples are likely to be representative of bulk groundwater $d\delta^{56}$ Fe and dMn/dFe and have undergone little modification by particle precipitation (Table S4). Nicollet Spring waters appear to have undergone more oxidative particle precipitation after exposure to air, with more than half of the total Fe being trapped on particle filters (Table S4). However, the water and particulate phases both feature similar, very negative δ^{56} Fe values of -0.85 to -0.74 ‰ (Fig. 6A), so the formation of a particulate phase in Nicollet Spring waters does not appear to impact the isotopic signature we infer for it.

Guided by the data described above, we consider it highly likely that subsurface groundwater supply is the dominant source of Fe to Deming Lake. Elk Spring waters feature very similar dCa/dMg, dMn/dFe, and d8⁵⁶Fe to the averaged water column (Figs. 3, 6), and to the inferred authigenic removal flux from the lake (Section 5.4). While not providing a perfect match for Deming Lake waters, notably in having an overall lower dFe/dCa ratio by an order of magnitude (0.06 mol/mol in Elk Spring vs. approximately 0.85 mol/mol column average in Deming Lake deep waters), Elk Spring provides clear evidence that Fe-rich groundwaters with the required d8⁵⁶Fe and dMn/dFe exist in the vicinity of Deming Lake and may be the most viable source of Fe. The specific higher dFe and dFe/dCa of Deming Lake vs. any accessible groundwater source in Itasca State Park may reflect the flow of Deming Lake input waters along an extended subsurface path through high-permeability tunnel valley deposits as described by Swanner et al. (2023a). Flowing groundwaters may accumulate additional Fe during anoxic alteration of host rocks, while a longer residence time of dFe than dCa in the lake, driven by redox cycling, is also discussed below as a potential driver of this elevated dFe/dCa relative to inputs, in Section 5.4.

5.2. Distinct Iron Systematics in Water Column Layers

The three layers defined by different dominant Fe cycling behaviors we define in the Deming Lake water column are shown schematically in Figure 4. These layers are particularly evident in May and August but appear to persist to some degree in March under the ice cover (Figs. 3, 4). This suggests that some similar processes operate in the lake year-round. Layer (I), above the oxycline, is defined by uniformly very low dFe that is up to several times lower than pFe. The particulate fraction has lower δ^{56} Fe than the dissolved fraction by approximately 0.2 to 1.0 ‰, with an offset that varies through the year but shows no clear depth dependence. Layer (II), extending from the base of the oxycline to the 12 m depth, features increasing dFe and δ^{56} Fe with increasing depth, particularly immediately below the oxycline. Dissolved Mn/Fe and pFe peak near the base of the oxycline. Particulate δ^{56} Fe is significantly higher than δ^{56} Fe throughout the upper parts of Layer (II) but trends towards similar values to the dissolved fraction approaching the chemocline at ~12 m. Layer (III), beneath the chemocline, is defined by extremely high dFe, δ^{56} Fe and Mn/Fe that are mostly unfractionated between dissolved and particulate phases, and little seasonal variation. As detailed further below, we interpret the Fe systematics of Layer (I) to be dominated by biological Fe uptake with variable lithogenic input (Section 5.2.1), Layer (III) to be

dominated by Fe^{2+}_{aq} oxidation and Fe^{3+} mineral precipitation (**Section 5.2.2**), and Layer (III) to be dominated by anoxic Fe^{2+} mineral precipitation (**Section 5.2.3**) (Fig. 4).

5.2.1. Layer (I): Biological Fe Uptake with Variable Lithogenic Input

Above the oxycline, $p\delta^{56}$ Fe values are more negative than $d\delta^{56}$ Fe values, by -0.18 to -1.15 ‰ (Fig. 7). This difference implies the particulate phase in the oxygenated mixolimnion preferentially takes up isotopically light Fe relative to the dissolved pool. The majority of total Fe in Layer (I) resides in the particulate phase, with pFe/Fe_T = 0.60-0.88 in May, 0.85-0.94 in August, and 0.58-0.70 in March (Fe_T = dFe + pFe; Fig. 7A). Under the assumption that Fe is predominantly advected upwards from depth in the lake, preferential uptake of isotopically light Fe to particles can also explain how $d\delta^{56}$ Fe values recover from such strongly negative values just below the oxycline to the slightly negative to slightly positive values seen in Layer (I) (Fig. 3).

Above the oxycline, low dFe levels are likely present as Fe³⁺ stabilized by complexation with dissolved organic matter that is abundant in Deming Lake and the source of its brown coloration (Swanner et al., 2023a). The subsequent uptake of isotopically light Fe into the particulate phase is explainable through biological uptake of this stabilized Fe pool. Biomass is abundant in the upper water column even during the ice-covered winter months, and selective Fe uptake by phytoplankton has been demonstrated in marine (Ellwood et al., 2020; Sieber et al., 2021) and lacustrine settings (K. Liu et al., 2022), to preferentially incorporate isotopically light Fe in cells and enrich the remaining dissolved pool in isotopically heavy Fe. In another lake study, Ellwood et al. (2019) attributed a switch in Fe isotope fractionation behavior above the oxycline of meromictic Lake Cadagno, Switzerland, to rapid kinetic precipitation of ferric oxides from aqueous Fe³⁺. The systematics observed in that setting are essentially identical to those observed and attributed to biological uptake here and in other studies. It is also not clear how rapid Fe³⁺ precipitation as oxides to drive a large kinetic isotope effect could be sustained several meters above the depth of high dFe and peak oxidation rates as in Lake Cadagno as reported by Ellwood et al. (2019). We suggest that such phenomena can uniformly be explained by the biological driver. The observed magnitude of the isotopic offset between particulate and dissolved Fe

The observed magnitude of the isotopic offset between particulate and dissolved Fe $(p\delta^{56}Fe - d\delta^{56}Fe)$, referred to hereafter as $\Delta^{56}Fe_{p-d}$, varies from -0.18 to -1.15 ‰ (Fig. 7B). The largest fractionation of -1.15 ‰ is comparable to the maximum $\Delta^{56}Fe_{p-d}$ observed in Lake Cadagno (-0.9 ‰; Ellwood et al., 2019), two boreal study lakes in Northwestern Ontario (-1.0 ‰; K. Liu et

al., 2022), and the upper Southern Ocean in a cold core eddy (~-1 ‰; Ellwood et al., 2020). In Deming Lake, the maximum and average Δ^{56} Fe_{p-d} in Layer (I) increase in magnitude from May (max -0.57 ‰, average -0.35 ‰), through August (max -0.94 ‰, average -0.76 ‰), into the following March (max -1.15 ‰, average -0.90 ‰). Particulate and dissolved δ^{56} Fe in Layer (I) show no systematic variations with depth, dFe, or pFe/Fe_T that may be expected with varied extents of exchange during biological Fe uptake (Fig. 7A).

676

677

678

679

680

681

682

683

684

685

686

687

688

689

690

691

692

693

694

695

696 697

698

699

700

701

702

703

704

705

706

One plausible control on observed Δ^{56} Fe_{p-d} values in Layer (I) that is consistent with other observations of Layer (I) chemistry is variable contributions of lithogenic Fe from surficial, possible eolian, deposition within this mixed upper layer (Figs 6, 7B). As such, eolian input may impact the low-Fe upper layers of the lake even though this flux is not a significant contributor to the overall lake Fe budget. Such a process could act to dilute both dissolved and particulate Fe pools with near-zero δ^{56} Fe material and mute any isotopic variability expressed between them. This is observed in the Al-rich upper few meters of the water column of Lake Cadagno (Ellwood et al., 2019), where Al is reasonably taken as an indicator of lithogenic material. Dissolved and particulate Al concentrations in Layer (I) are both highest in May 2022 and lowest in March 2023. and Fe_T/Al_T values in Layer (I) are lowest in May 2022 and highest in March 2023 (Figs. 6C, 7B; Table S3). The lowest Fe_T/Al_T in the May 2022 water column, observed at 0 m depth, is 0.83 mol/mol, the lowest value observed in Layer (I) in any season. This Fe/Al ratio is similar to the value of 0.74 mol/mol determined from the snow ice cover sampled in March 2023 and taken as a compositional proxy for atmospheric inputs to the lake (Fig. 6C). The δ^{56} Fe value of -0.20 % for the snow ice cover is isotopically heavier than $p\delta^{56}$ Fe observed in Layer (I) (Fig. 6A), so addition of this inferred eolian Fe component to the dFe and pFe pools would contribute to a smaller apparent Δ^{56} Fe_{d-p}. Qualitatively, the increase in magnitude of the apparent Δ^{56} Fe_{d-p} from May 2022 to March 2023 is consistent with our expectations for the changing flux of this eolian material throughout the year. Layer (I) in the May 2022 water column should bear the imprints of recent melting of winter ice and inmixing of eolian particles that accumulated on the ice cover throughout winter. August should feature a decreased influence from this post-winter component. In March 2023, ice cover would prevent direct aerosol input to Layer (I). Therefore, the expression of the largest Layer (I) Δ^{56} Fe_{p-d} in March 2023 likely reflects the endmember Fe isotopic fractionation associated with biogenic Fe uptake, a value consistent with maximum fractionations observed in the mixed layer of other water bodies (Ellwood et al., 2019, 2020; K. Liu et al., 2022).

707

732

733

734

735

736

5.2.2. Layer (II): Precipitation of Ferric Iron-Bearing Phases 708 709 Layer (II) features consistent behaviors in May and August, while Fe cycling is sufficiently distinct in March that we discuss it separately in Section 5.3. Unlike in Layer (I), deeper layers in the lake 710 feature pAl more than an order of magnitude lower than pFe, so detrital contributions of Fe to the 711 particulate populations of the metalimnion and monimolimnion are not considered hereafter. 712 Beneath the oxycline in May and August, dFe and $d\delta^{56}$ Fe sharply increase with depth, as observed 713 previously in Fe-rich anoxic lakes and attributed to Fe partitioning between soluble ferrous and 714 insoluble ferric phases (Malinovsky et al., 2005; Teutsch et al., 2009; Busigny et al., 2014; Ellwood 715 et al., 2019; Yang et al., 2022; K. Liu et al., 2022). The maximum Δ^{56} Fe_{p-d} values observed in 716 Layer (II) are +1.54 and +1.74 % in May and August respectively (Figs 3B, E), which overlap 717 with values between +0.59 and +2.14 % recorded beneath the oxycline in previous anoxic lake 718 studies (Malinovsky et al., 2005; Ellwood et al., 2019; K. Liu et al., 2022). In all cases, these 719 fractionations are interpretable through equilibrium fractionation between ferric and ferrous Fe 720 that enriches the insoluble ferric phase in heavy Fe isotopes. In this layer, pMn/pFe is persistently 721 lower than dMn/dFe (Figs 3C, F), as expected following the formation of Fe³⁺-rich particulates, 722 because Fe²⁺_{aq} and Mn²⁺ exhibit similar behaviors but Mn⁴⁺ particles only form at higher redox 723 potentials than Fe^{3+} and in the absence of Fe^{2+}_{aq} (Robbins et al., 2023). 724 Teutsch et al. (2009) suggested that this pattern of fractionation is driven in Lake Nyos, 725 726 Cameroon, by the progressive dissolution of ferric oxyhydroxides sinking beneath a layer of quantitative oxidation at the oxycline; as a result of microbial dissimilatory Fe³⁺ reduction (DIR) 727 which preferentially releases light Fe into Fe²⁺_{aq}. While such an interpretation is consistent with 728 the large fractionation known to be induced by DIR (Beard et al., 1999; Crosby et al., 2007), its 729 formulation assumes quantitative oxidation of Fe²⁺_{aq} solely at the oxycline, which is difficult to 730 731

quantitative oxidation at the oxycline; as a result of microbial dissimilatory Fe^{3+} reduction (DIR) which preferentially releases light Fe into Fe^{2+}_{aq} . While such an interpretation is consistent with the large fractionation known to be induced by DIR (Beard et al., 1999; Crosby et al., 2007), its formulation assumes quantitative oxidation of Fe^{2+}_{aq} solely at the oxycline, which is difficult to reconcile with positively fractionated $p\delta^{56}Fe$ values already forming several meters below the oxycline that we observe in Deming Lake. However, while it may not be the dominant control on water column $\delta^{56}Fe$ systematics, DIR of sinking Fe^{3+} precipitates likely is occurring in Layer (II) of Deming Lake. Such a process can explain why a peak in particulate Fe around the oxycline is not propagated downward through Layer (II) by particle sinking. As discussed in **Section 5.4**, recycling of ferric precipitates is likely the dominant processes that retains Fe^{2+}_{aq} in the lake water

737 column for far longer than the water residence time (Campbell and Torgersen, 1980; Swanner et al., 2023a).

739 Studies of anoxic Fe rich lakes have more commonly attributed the systematics we observe in Layer (II) in May and August to progressive oxidation of upwelling Fe²⁺_{aq} that removes 740 isotopically heavy Fe from solution as Fe³⁺ particles. Experimental studies have documented an 741 equilibrium isotopic fractionation of 3.0 % in δ^{56} Fe between Fe²⁺_{ag} and Fe³⁺_{ag} that enriches the 742 latter in ⁵⁶Fe (Johnson et al., 2002; Welch et al., 2003). In near-neutral aqueous conditions like the 743 ones that exist in the majority of marine and lacustrine settings, Fe³⁺ is highly insoluble and rapidly 744 hydrolyses to form precipitates of Fe³⁺-oxyhydroxides or other hydrous ferric minerals, such as 745 phyllosilicates or phosphates, according to the prevailing solution chemistry (e.g. Cosmidis et al., 746 2014; Hinz et al., 2021; Millero, 1998; Millero et al., 1987). Experiments produce a range of net 747 Fe isotopic fractionations during the formation of Fe³⁺-oxyhydroxides following the oxidation of 748 Fe²⁺_{aq}, reflecting in part a range in fractionations between short-lived Fe³⁺_{aq} and the mineral 749 precipitates where additional equilibrium and/or kinetic isotope effects accompany precipitation 750 (Bullen et al., 2001; Skulan et al., 2002; Croal et al., 2004; Balci et al., 2006; Beard et al., 2010; 751 Wu et al., 2011; Nie et al., 2017). The two-step transformation from Fe^{2+}_{aq} to solid Fe^{3+} precipitates 752 during oxidation of ferruginous waters can therefore be associated with variable sizes of net Fe 753 isotopic fractionation of 1 to 3 ‰, but in all cases the precipitates should be isotopically heavier. 754 The Δ^{56} Fe_{p-d} values we observe within Layer (II) are consistent with the formation of particulate 755 Fe³⁺ by oxidation processes occurring at and beneath the oxycline. 756

Free O_2 is likely the major oxidant for Fe^{2+}_{aq} in the shallower levels of Layer (II) (Figs. 8A-B). Particulate Fe concentration peaks around the base of the oxycline and slightly below the SCML in the May and August water columns (Figs. 8C-D), where O_2 should be supplied photosynthetically but rapidly consumed by oxidation. The convergence of dFe and dO_2 profiles at near zero values around this depth layer are consistent with the expectations of simple 1D reaction-transport models for the oxidation of upwelling ferruginous waters by an oxygenated overlying photic zone (Czaja et al., 2012; Heard et al., 2020). The development of strongly negative $d\delta^{56}$ Fe values (Figs. 8 E-F) and a sharp decrease in dFe compared to deeper waters are explainable by extensive oxidation of Fe^{2+}_{aq} by O_2 and precipitation of isotopically heavy Fe^{3+} . The occurrence of these isotopic signatures near the SCML could also directly implicate cyanobacteria in driving the large positive Δ^{56} Fe_{p-d} because both oxidation of Fe^{2+}_{aq} mediated by

757

758

759

760

761

762

763

764

765

766

767

cyanobacteria, and adsorption of Fe³⁺_{aq} to their cells, are observed in experiments to enrich the particulate phase in ⁵⁶Fe by 1.8 to 2.9 % relative to Fe²⁺_{aq} (Mulholland et al., 2015; Swanner et al., 2017).

Sinking Mn oxide particles formed by the O_2 -induced oxidation of Mn^{2+}_{aq} in overlying waters can also play a role in Fe^{2+}_{aq} oxidation. In both the May and August water columns, the depth of maximum Fe^{2+}_{aq} oxidation is marked by a sharp increase in dMn and a sharp decrease in pMn and pMn_{ox} relative to overlying waters (Figs. 8A-B). These covariations are consistent with Fe^{2+}_{aq} oxidation at the expense of the reduction of sinking Mn oxides, due to the higher redox potential of the Mn^{2+} - Mn^{4+} redox couple. The simplified net reaction:

$$2Fe^{2+} + MnO_2 + 4H_2O = 2Fe(OH)_3 + 2H^+ + Mn^{2+}$$
(7)

has been inferred at Lac Pavin (Busigny et al., 2014), where Fe(OH)₃ represents potential Fe³⁺-bearing mineral precipitates. From a stoichiometric perspective, Busigny et al. (2014) argued that at Lac Pavin, the change in dissolved dMn occurring around the redoxcline was an order of magnitude smaller than the change in dFe and thus sinking MnO₂ could only account for a fraction of the total Fe²⁺_{aq} oxidation taking place. By contrast, around the top of Layer (II), the sharp ~1,000 μ g/L drop in dFe is of a similar magnitude to the ~300 (in May) to 1,000 μ g/L (in August) increase in dMn that occurs at the same depth in the Deming Lake water column (Figs 8A-B). However, pMn and pMn_{ox} change by only up to tens of μ g/L in May and August, significantly less than the ~300 μ g/L spike in pFe at this depth, which introduces some ambiguity into the relative role of Mn-oxide driven Fe²⁺_{aq} oxidation at the top of Layer (II). It thus appears plausible that up to tens of percent of the total oxidative Fe drawdown in August at this depth level may be driven by Mn oxide reduction, but direct O₂ oxidation is likely also required.

While the sharpest changes in dFe and pFe occur within 1 m of the oxycline and can be reasonably attributed to oxidation by O_2 (either directly or via Mn oxides), dFe and $d\delta^{56}$ Fe continue increasing with depth to the base of Layer (II) (Fig. 3). This suggests that oxidation of upward-diffusing Fe^{2+}_{aq} begins at greater depth within the anoxic portion of the water column, and indeed, a large $\Delta^{56}Fe_{p-d} > 1$ ‰ down to 10 m depth is still observed in the May water column where particulate data are available. Beneath 6 m depth, dissolved dO_2 is below the ~0.01 mg/L detection level of the YSI sensor. At such low dissolved dO_2 , direct abiotic Fe^{2+}_{aq} oxidation would be hindered, unless *in situ* cyanobacterial O_2 production at these depths acts as a cryptic O_2 source that is balanced by rapid consumption during oxidation. Alternatively, low-oxygen or anoxic

biological oxidation pathways, such as microbial Fe^{2+} oxidation by microaerophilic chemoautotrophs or anoxygenic photoautotrophs, could drive the formation of isotopically heavy Fe^{3+} -dominated particulates under low dO_2 conditions to at least 10 m depth in May. Similar systematics of heavy Fe isotope removal to particulates many meters below the redoxcline are observed in numerous other ferruginous lakes and have been similarly attributed to these pathways (Ellwood et al., 2019; Yang et al., 2022; K. Liu et al., 2022). Microaerophilic chemoautotrophs can function at single digit micromolar O_2 concentrations below our detection limit (Chan et al., 2016) and produce Fe^{3+} precipitates with positive $\Delta^{56}Fe_{p-d}$ similar to other known oxidation mechanisms (Bullen et al., 2001; Croal et al., 2004; Balci et al., 2006; Rouxel et al., 2018). Alternatively, anoxygenic photosynthetic bacteria have also been observed to drive $\Delta^{56}Fe_{p-d}$ values consistent with our observations in Deming Lake (Croal et al., 2004; Swanner et al., 2015b). At this time we are unable to determine whether anoxygenic phototrophs are present in Deming Lake, whether they would be utilizing Fe^{2+}_{aq} rather than even a trace sulfide pool in the anoxic portion of the water column as observed in ferruginous Lake Matano, Indonesia (Crowe et al., 2014), or if there is sufficient light to drive photosynthesis at those depths.

While persistently positive, Δ^{56} Fe_{p-d} values in Layer (II) decrease in magnitude with increasing depth and increasing dissolved Fe²⁺_{aq} (Fig. 9), suggesting additional factors beyond fractionation during Fe²⁺_{aq} oxidation. Kinetic isotope effects are unlikely to be driving this variability because these would drive lower net Δ^{56} Fe_{p-d} values at the depth of maximum Fe²⁺_{aq} oxidation rates. These rates are highest at the top of Layer (II), where observed Δ^{56} Fe_{p-d} values are in fact the largest. More likely contributors to variable Δ^{56} Fe_{p-d} values include changing ferric/ferrous Fe proportions in mineral precipitates, the adsorption of Fe²⁺_{aq} to ferric mineral surfaces, and the adsorption of Fe³⁺_{aq} to cells (Crowe et al., 2011; Cosmidis et al., 2014; Busigny et al., 2014; Swanner et al., 2017). The partial survival of sinking particles formed at shallower depths with more negative δ^{56} Fe could also decrease the observed Δ^{56} Fe_{p-d} deeper in Layer (II), and as discussed below in the context of Layer (III) (**Section 5.2.3**), this phenomenon may be enhanced in August 2023 due to major particle formation and coagulation at around the SCML.

Iron isotopic interpretations often simplify the Fe^{3+} -bearing precipitate phase to a Fe^{3+} oxyhydroxide. However, detailed mineralogical analysis of suspended particles in Lac Pavin, from depths where anoxic Fe^{2+}_{aq} oxidation was inferred, indicated a mixture of Fe^{3+} -bearing phyllosilicates, oxyhydroxides, bacterially-associated amorphous ferric-ferrous phosphates, and

vivianite (Fe₃(PO₄)₂·8(H₂O)), a ferrous phosphate mineral (Cosmidis et al., 2014). Among these putative phases, it is notable that Layer (II) particles in Deming Lake feature pP values that are significant relative to pFe (Table S7; Fig. 10). Any phosphate-associated Fe²⁺ component should be less ⁵⁶Fe-enriched than purely Fe³⁺-bearing phases and increased contributions of such phases with increasing dFe at depth provide one possible explanation for the depth dependence of Δ^{56} Fe_{p-d}. Particulate Fe/P ratios between 1.0 and 8.9 mol/mol (Table S7; Fig. 10) are consistent with variable combinations of Fe³⁺ oxyhydroxides with surfaced-adsorbed phosphate, and/or a Fe phosphate phase that may host some Fe²⁺, and these ratios also agree with observations from Lac Pavin (Cosmidis et al., 2014). We discuss the potential importance of vivianite specifically in Layer (III) further in **Section 5.2.3** below. A lack of correlation between pFe/pP and Δ^{56} Fe_{p-d} suggests, however, that other less fractionated particulate Fe phases must also be present in Layer (II).

Another pathway to incorporating isotopically lighter Fe²⁺ in deeper Layer (II) particles is through the partial precipitation of authigenic magnetite (Fe²⁺Fe³⁺₂O₄) and/or carbonated green rust [Fe²⁺_(1-x)Fe³⁺_x(OH)₂]^{x+}·[(x/2)CO₃²⁻· (m/2)H₂O]^{x-}) in the water column, as has been observed in Lakes Towuti and Matano, Indonesia (Zegeye et al., 2012; Bauer et al., 2020), and in flow-through reactor experiments (Benner et al., 2002). These biomineralization pathways involve partial reduction of Fe³⁺-oxyhydroxides coupled to organic matter respiration; and may be expressed more clearly in August than May due to increased production of organic matter in the overlying SCML in August.

In addition to mineralogical controls, the $\Delta^{56}Fe_{p-d}$ deeper in Layer (II) may be impacted by adsorption of Fe^{2+}_{aq} to mineral surfaces, which will increase at higher dFe (Busigny et al., 2014). Adsorption of Fe^{2+}_{aq} to ferric oxyhydroxide mineral surfaces has been observed experimentally to produce an adsorbed pool with $\Delta^{56}Fe_{p-d}$ between 0.30 and 0.87 ‰ (Crosby et al., 2007). An increased fraction of adsorbed Fe^{2+}_{aq} (Crowe et al., 2011) with a lower but still positive $\Delta^{56}Fe_{p-d}$ values with increasing depth in Layer (II) provides a further pathway to generating the depth-dependent $\Delta^{56}Fe_{p-d}$ we observe, and is supported by a clear negative correlation between $\Delta^{56}Fe_{p-d}$ and dFe in Layer (II) (Fig. 9).

859 4.2.3. Layer (III): Anoxic Precipitation of Ferrous Minerals

Layer (III) lies below the chemocline in Deming Lake and is defined by dramatically elevated total dissolved solutes, particularly dissolved Fe, Ca, and Mg. Both $d\delta^{56}$ Fe and dMn/dFe are nearly invariant at depths greater than 12 m across the three seasons (Fig. 3). Particulate Fe removal at these depths appears to have limited impact on the dissolved Fe mass balance in Layer (III), with >99 % of Fe in the dissolved phase. Particle formation also drives muted fractionation, with dissolved and particulate Mn/Fe being indistinguishable in Layer (III) in all seasons and Δ^{56} Fe_{p-d} being within error of 0 % in May and March. The two available Layer (III) datapoints from August feature non-zero Δ^{56} Fe_{p-d} values of 0.32 to 0.36 % and as discussed below, may reflect enhanced survival of sinking Layer (II) particles at this time.

These observations suggest that Layer (III) is defined by stable precipitation of a small fraction of the dissolved Fe pool into ferrous minerals which, unlike Fe^{2+}_{aq} oxidation, minimally fractionates $\delta^{56}Fe$ and Mn/Fe. The high dissolved Fe^{2+}_{aq} levels in Layer (III) should strongly buffer oxidant species, while photosynthetically active radiation <0.01 μ M photons/m²/s (Swanner et al., 2023b) should inhibit anoxygenic photosynthesis. Ferrous minerals at or above saturation equilibrium and thus able to precipitate in the deepest waters of Deming Lake may include vivianite, and Fe-bearing carbonates, both of which have been observed to form in other ferruginous water columns (Crowe et al., 2008; Jones et al., 2011; Cosmidis et al., 2014; Herndon et al., 2018; Vuillemin et al., 2020, 2022; Wittkop et al., 2020b).

The precipitation of vivianite in Layer (III) is suggested by elevated pP beneath the chemocline, increasing with depth in a manner that tracks increasing dP (Table S7; Fig.10). To assess if vivianite precipitation in Layer (III) is reasonable, we calculated the vivianite saturation index (SI) for waters in Deming Lake for August 2023, when return sampling enabled determination of requisite cation-anion data (Rico et al., in prep), using measured pH, dP and dFe, and a published solubility product constant (K_{sp}) for vivianite of 10^{-35.8} (Al-Borno and Tomson, 1994). We find that the SI values for vivianite— calculated as log(Q/K), where Q = lon activity product and K = lon = l

or theoretical data exist for the Fe isotopic systematics of vivianite. However, the fact that Δ^{56} Fe_{p-d} values are unresolvable from 0.0 ‰ even in samples (Fig. 9) where over 2/3 of pFe appears to be hosted in vivianite, strongly suggests that the precipitation of vivianite from oversaturated anoxic solutions is associated with little Fe isotopic fractionation.

Saturation of Fe and Mn carbonates in the monimolimnion of anoxic lakes and accumulation in underlying sediments is well-documented (Crowe et al., 2008; Jones et al., 2011; Lambrecht et al., 2018; Herndon et al., 2018; Wittkop et al., 2020b; Vuillemin et al., 2022). Using dissolved inorganic carbon (DIC) concentrations from a multiparameter database for Deming Lake (Swanner et al., 2023b), and assuming relative year-to-year stability of solutes in the lake over this timeframe, we estimated the SI for siderite, FeCO₃. The siderite SI was 1.20 at 14 m depth, lower than 1 for all depths shallower than 14 m, and lower than 0 for all depths shallower than 9 m. Therefore, precipitation of Fe-bearing carbonates appears feasible within Layer (III).

The particulate profiles of common carbonate-hosted cations Mg²⁺, Ca²⁺, Mn²⁺, and Fe²⁺ (corrected for vivianite) show clear covariation in Layer (III) of Deming Lake (Table S7; Fig. 11A, C, E). This can be seen most clearly between 12 and 14 m depth in May where all four elements peak in concentration (Fig. 11A). Here, pMg, pCa, and pMn are all strongly positively correlated. Bulk pFe is not correlated with these elements, but after correcting for Fe hosted in vivianite $(pFe_{corr} = pFe - pFe_{vivianite})$, pFe_{corr} also shows a positive relationship with the other three divalent cations in May (Fig 11B). We take these covariations to indicate that carbonate is the dominant mineral precipitate in Layer (III) for Mg, Ca, and Mn, and a significant carrier, at least in May, of non-vivianite-hosted Fe. As pure calcite, dolomite, and rhodochrosite are undersaturated at these depths, a mixed cation carbonate phase such as ankerite, Ca(Fe,Mg,Mn)(CO₃)₂, a ferroan dolomite, or an amorphous precursor to these mineral phases, could be the major host for these elements. Taking pFe_{corr} to approximate carbonate-hosted Fe for May, we find that carbonate pFe/pMg, pFe/pCa, and pFe/pMn ratios are respectively 0.93-2.8 mol/mol, 0.56-1.4 mol/mol, and 9.6-23 mol/mol. These ratios are consistent with ankerite and siderite, or amorphous precursors to these phases, being the dominant carbonate minerals forming in Deming Lake. At the high dMn levels in Deming Lake, formation of kutnohorite, CaMn(CO₃)₂, may also be possible (Wittkop et al., 2014, 2020b; Herndon et al., 2018). Particulate Mg, Ca, and Mn are lower in August and March, suggesting less overall carbonate precipitation (Fig. 11), and are uncorrelated with pFe_{corr} in these

months. This lack of correlation likely reflects the dilution of any less abundant carbonate-hosted Fe by other authigenic Fe phases.

921

922

923

924

925

926

927

928

929

930

931

932

933

934

935

936

937

938

939

940

941

942

943

944

945

946

947

948

949

950

The Δ^{56} Fe_{p-d} values observed in Layer (III) (Figs. 3, 9) suggest that Fe isotopic fractionation associated with carbonate precipitation is not significant. Experimental constraints on the Fe isotopic fractionation between siderite and Fe²⁺_{aq} range from Δ^{56} Fe_{sid-Fe2+aq} = -0.48 ± 0.22 % during abiotic precipitation from solution (Wiesli et al., 2004) to Δ^{56} Fe_{sid-Fe2+aq} = 0.0 % during siderite precipitation following microbial DIR (Johnson et al., 2005). Thus, Fe carbonate precipitation should induce a zero to slightly negative Δ^{56} Fe_{p-d} value. Our finding that Δ^{56} Fe_{p-d} is indistinguishable from zero in Layer (III) in May and March therefore agrees with the experimental results, given that we can infer that between 1/3 and 2/3 of particulate Fe is hosted in carbonate in these months.

The positive Δ^{56} Fe_{p-d} of ~ 0.33 % observed in Layer (III) in August (Figs. 3E, 9) may in part reflect the persistence of sinking Fe³⁺-bearing phases either as minerals that are observed to be capable of partial surviving sinking and burial in ferruginous sediments (Crowe et al., 2008; Friese et al., 2021; Gadol et al., 2022; Akam et al., 2024), or cells with adsorbed Fe³⁺_{ag} (Swanner et al., 2017), in the anoxic portion of the water column. In all cases, these heavy isotopic signatures would be diluted by unfractionated carbonates and vivianite. Delivery of magnetite to the sediment-water interface (Lascu et al., 2012) offers a means to transfer isotopically heavy ferric Fe precipitated in Layer (II) downward to Layer (III), as might the sinking of mixed-valence green rust (Zegeye et al., 2012). Last, adsorption of Fe²⁺_{aq} onto Fe³⁺-oxyhydroxide surfaces may protect ferric particles in the fully anoxic portion of the water column by rendering the Fe³⁺ mineral surface inaccessible to DIR-operating bacteria and thus 'deactivating' these sinking minerals (Roden and Urrutia, 1999, 2002; Royer et al., 2004; Friese et al., 2021). Turbidity around 6 m depth is dramatically higher in August and overlaps with the SCML. The presence of abundant particulate organic matter may thus aid the export of ferric particulates deep into the water column. Physical settling rates may be higher where ferric particulates coagulate with sinking cellular material to increase particles size. Meanwhile, close associations of sinking Fe³⁺-oxyhydroxides with abundant particulate organic matter may promote partial microbial reduction and biomineralization of mixed-valence Fe phases like magnetite and green rust and the adsorption of $\mathrm{Fe^{2+}_{aq}}$. All of those processes would decrease the observed $\Delta^{56}\mathrm{Fe_{p-d}}$ within Layer (II) but,

conversely, increase the survivability of sinking partially ferric precipitates, matching our observations of particulate Fe isotopic variability in August.

5.3. Impacts of Ice Cover and Winter Mixing on Fe Cycling

The water column sampled in March 2023 has distinct geochemical profiles compared to May and August 2022 (Figs. 2, 3), with features attributable to the effects of ice cover, and vertical mixing above 12 m driven by thermocline collapse (Swanner et al., 2023a). Ice cover should inhibit atmospheric exchange, driving shallowing of the oxycline to 2.5 m and lower dO_2 in surface waters (Fig. 2L); impose light limitation on photosynthetic biomass and dO_2 production; and shut down lithogenic particle delivery from atmospheric dust (Fig. 7B). These factors result in elevated dFe in surface waters compared to May and August 2022 (Fig. 3G) and larger negative Δ^{56} Fe_{p-d} values (Fig. 7).

The water column between the oxycline and the chemocline has a distinct geochemistry in March. A sharp increase in dFe beneath the shallowed oxycline reflects the restriction of strong biological and oxidative Fe^{2+}_{aq} removal to depths shallower than 3 m (Fig. 3G). At 3 m, $\Delta^{56}Fe_{p-d}$ = 0.19 ‰ (Fig. 3H), which may reflect offsetting effects of isotopically heavier Fe^{3+} precipitates and isotopically light biological material forming in the same depth range. Dissolved $\delta^{56}Fe$ does not reach values lower than -0.85 ‰ at the base of the oxycline, suggesting less extensive oxidation of Fe^{2+}_{aq} in March due to lower dO₂ (Fig. 2L).

At greater depths in the March Layer (II), dFe plateaus at levels 10 times lower than those observed in the same layer in ice-free seasons and remains at these lower levels to as deep as \sim 10 m, beneath which it increases sharply to seasonally stable dFe levels beneath the chemocline (Fig. 3G). March d δ^{56} Fe profiles between 3 and 10 m depth show muted variation, with values between -0.99 ‰ at 9 m depth -0.71 ‰ at 4.5 m depth (Fig. 3H). Particulate Fe concentrations are an order of magnitude lower in March throughout this section of the water column than during May and August, while Δ^{56} Fe_{p-d} varies in a narrow range from 0.42-0.58 ‰ (Figs. 3G-H). Similarly, dMn/dFe in this depth range shows muted variation over a factor of less than 4, with pMn/pFe values that are consistently 0.2 to 0.3 times the dissolved value (Fig 3I). These data collectively suggest that the Layer (II) water column establishes a new configuration during winter with a stable particulate formation regime defined by low fractions of dFe precipitation, Δ^{56} Fe_{p-d} of \sim 0.5 ‰, and modest depletion of pMn/pFe (Figs. 3, 9).

Physical processes can provide the best explanation for the reconfigured water column Fe chemistry in March. During cooling of surface waters beginning in late fall, Deming Lake becomes isothermal and loses its thermal stratification, undergoing vertical mixing of the epilimnion and metalimnion (Swanner et al., 2023). The monimolimnion waters are denser with much higher dissolved loads and thus resist this mixing. The result of vertical mixing should be to homogenize the upper ~ 10 m of a 'late summer' water column that would roughly resemble the ice-free May to August 2022 water columns (Fig. 12). This would mix low dFe, near-zero d δ^{56} Fe Layer (I) waters containing some O_2 , with anoxic Layer (II) waters featuring highly variable Fe chemistry but generally higher dFe and more negative d δ^{56} Fe. Within the upper few meters of this homogenized water column, limited extents of Fe²⁺aq oxidation and biological Fe uptake would subsequently be superimposed on the new chemical profile.

To test this hypothesis of vertical homogenization of a late summer water column above the chemocline, we estimate column-averaged May and August dFe and $d\delta^{56}$ Fe values in the lake volume above 10 m depth using numerical integration as in **Section 5.1**. For May, the column-averaged values for dissolved dFe (dFe_{col}) and $d\delta^{56}$ Fe ($d\delta^{56}$ Fe_{col}) above 10 m are 762 µg/L and -0.86 ‰, respectively, and for August, dFe_{col} = 980 µg/L and $d\delta^{56}$ Fe_{col} = -0.81 ‰ (Figs. 12A-B). These values compare favorably with the range of dFe and $d\delta^{56}$ Fe in the March water column (Fig. 12A). Calculating the same total column averages above 10 m for March would produce dFe_{col} = 570 µg/L and $d\delta^{56}$ Fe_{col} = -0.81 ‰. The lower dFe_{col} value suggests some net removal of dFe, likely in the upper few meters of the water column through Fe³⁺ oxyhydroxide precipitation and cellular Fe uptake after more Fe-rich waters were mixed upward. Removal of the requisite 192-410 µg/L over the upper 9 m of water depth by particle formation, sinking, and redissolution below the chemocline would create no detectable change in dissolved dFe in Layer (III).

An apparent ~2.5 m-high perturbation centered around 5.5 m depth with higher dFe (by ~100-150 μ g/L or ~20%) and d δ^{56} Fe (by ~0.10 ‰) and lower dMn/dFe (by ~0.6 mol/mol) relative to over- and underlying waters (Figs. 3G-I) is not explained by this vertical homogenization process. This feature cannot reflect the breakdown of sinking particulate Fe, as pFe is uniformly low (<20 μ g/L), and p δ^{56} Fe is higher at 5.5 m than in overlying waters (Fig 3G). We suggest instead that this water column feature reflects a depth interval of enhanced Fe input from the lakebed. Such an input flux would need to have higher dFe and d δ^{56} Fe and lower dMn/dFe than '*in situ*' waters at this depth in the lake water column. A supply of dFe to the water column at this depth that is only

evident during winter months may derive from reductive dissolution of sediments on the lakebed. In May and August, peak Fe³⁺-oxyhydroxide precipitation occurs at 6 to 6.5 m depth (Figs. 3, 8). Sediments formed from water column particles precipitated around this depth contain abundant isotopically heavy, reducible Fe with low Mn/Fe, and may seasonally undergo reductive dissolution (driven by microbial DIR) when the oxycline migrates to above these depths during winter. A ~15-25 % contribution of dFe from quantitative dissolution of Fe³⁺ oxyhydroxide sediment with δ^{56} Fe = 0 to 0.5 % can account for the ~0.1 % positive shift in $d\delta^{56}$ Fe within this depth region of slightly elevated dFe.

Iron particle formation in the March mid-depth water column is muted, with pFe several times lower than that seen in Layer (II) in May and August (Fig. 3G). This limited particle formation is associated with Δ^{56} Fe_{p-d} ~0.5 ‰ (Figs. 3H, 9). Given the lack of significant atmospheric O₂ penetration, these muted fractionations deeper in the water column likely reflect the formation of a mixed-valence Fe phase where isotopically heavy Fe³⁺ is diluted by unfractionated Fe²⁺. These mixed valence phases may include green rust, magnetite, or ferric-ferrous amorphous phosphates observed to form in other ferruginous water columns (Zegeye et al., 2012; Cosmidis et al., 2014; Bauer et al., 2020) that were inferred to form deeper in Layer (II) in August. Particulate Fe/P ratios <1 mol/mol in the March mid-depth water column (Fig. 10F) support that an amorphous (mixed-valence) Fe phosphate could be a significant pFe carrier, but vivianite is undersaturated at these depths.

5.4. Sedimentary Outputs, Residence Time, and Recycling of Iron in Deming Lake

Deming Lake sediments sampled between 1 and 16.5 m water depth are far more uniform in their chemistry and δ^{56} Fe than the particulates forming in the overlying water column (Fig. 6). Based on the observation that sediments between 1 and 12 m depth feature δ^{56} Fe values indistinguishable from the bulk upper continental crust (UCC) value of 0.09 to 0.12 ‰ (Dauphas et al., 2017; X.-M. Liu et al., 2022), with Fe/Al and Mn/Fe ratios within \pm 20 % and a factor of two of the UCC estimates, respectively (Fe/Al_{UCC} = 0.21 mol/mol, Mn/Fe_{UCC} = 0.017 mol/mol; Taylor and McLennan, 1995), any contribution of authigenic Fe to the bulk sediment is likely minor. At 14 and 16.5 m depth, Fe/Al in the lake sediments (0.43-0.47 mol/mol) is slightly more than double the UCC value and Mn/Fe (0.057 mol/mol) is more than three times the UCC value, while δ^{56} Fe values are slightly lower than the 1 to 12 m sediment values and UCC value, at 0.00 \pm

0.049 % and 0.038 ± 0.049 %. We estimate the authigenic Fe fraction in the 14-16 m sediment to be ~0.53 (Table S5). The implied ~1:1 mixture of crustal-like (δ^{56} Fe = 0.1 %) Fe, and authigenic Fe from Layer (III) (with δ^{56} Fe = -0.30 to 0.03 %) would reproduce the δ^{56} Fe values of the 14 and 16 m sediments provided that slightly higher δ^{56} Fe August water column particles contribute part of the sedimentary Fe budget at this depth. Our conclusions would not change qualitatively if we instead compared sedimentary values to local lithogenic sources best represented by the MN till samples CSS-43 and WAD-25, with Fe/Al = 0.29 mol/mol and Mn/Fe = 0.022 mol/mol (Wittkop et al., 2020a).

Overall, our data suggest that some particulate authigenic Fe formed in the water column below 12 m depth survives sedimentary burial, while little particulate Fe survives burial at shallower depths in the lake. Across all seasons and depths, water column pFe/pAl ranges from 1.1 to 60 mol/mol, with values generally increasing with depth, pFe, and from May (most lithogenic input) to March (least lithogenic input; Fig. 6D, Table S3). Particulate Fe/Al is always >10 mol/mol in Layer (III). Therefore, Deming Lake bottom sediments with Fe/Al ~0.20 mol/mol are depleted in Fe by more than 6 times, but often upwards of 100 times, relative to suspended particles. Sedimentary Fe/Al is also more than three times lower than the inferred atmospheric lithogenic source sampled from the ice core with Fe/Al = 0.74 mol/mol (Fig. 6D). The crustal δ^{56} Fe signature of Deming Lake bottom sediments deposited above 12 m water depth therefore likely reflects the survival solely of unreactive lithogenic minerals.

High organic carbon burial in Deming Lake (Lascu et al., 2012) should promote efficient reductive dissolution of Fe³⁺-bearing minerals deposited on the lakebed. Meanwhile, aerobic respiration of cyanobacterial organic matter in Layer (I) would release cell-bound Fe back into the water column and prevent accumulation of isotopically light biogenic Fe in sediments in the upper ~6 m of the lake. These two processes appear to occur withing the upper ~1 cm of the sediment, because δ^{56} Fe values of 1 cm intervals between 0 and 7 cm depth in the sediment pile obtained via the push core at 4 m lake depth are uniform and crustal (Fig. 6A). Authigenic Fe enrichments only survive in sediments deposited well below the chemocline where we interpret that pFe is dominated by ferrous minerals such as vivianite and Fe bearing carbonates. These minerals should more easily survive burial under reducing conditions alongside organic matter. In support of the survival and significant contribution of vivianite to the authigenic Fe sedimentary load, the 14-16.5 m sediments contain approximately 1600 µg/g of P, more than two times the average P

concentration of 740 µg/g we observed in sediments formed at 1-12 m depth. As reduced phases precipitated in Layer (III) appear to be the dominant removal flux of Fe from the lake, the net removal flux should have an δ^{56} Fe value of -0.30 to -0.20 ‰ (or perhaps up to 0.03 ‰, as observed in August) similar to particles sampled beneath 12 m water depth. This δ^{56} Fe for the removal flux overlaps with the $d\delta^{56}$ Fe values for waters from Elk Spring inferred to be the most plausible source of Fe to Deming Lake (Section 5.1).

The total flux of authigenic Fe is quantifiable for sediments deposited at 14 and 16 m depth, because Fe/Al ratios are significantly higher than the UCC value (Fig. 6D), and ²¹⁰Pb- and ¹⁴Cderived sedimentary accumulation rates are available for the deepest part of the lake (Lascu et al., 2012). Dry sediment mass accumulation rates in the deepest part of Deming Lake over the last several decades are approximately 20-50 mg/cm²/yr. We calculate the average authigenic Fe concentration in these sediments, after correcting for detrital Fe using the measured Al concentration and the published Fe/Al of the UCC (Taylor and McLennan, 1995), to be 1.77 wt%. We thus estimate an authigenic Fe burial rate below 12 m depth of 0.35-0.89 mg Fe/cm²/yr. A \sim 6.3 \times 10⁷ cm² area of the lake floor underlies water of at least 12 m, giving a total authigenic Fe burial rate of $\sim 2.2-5.5 \times 10^4$ g Fe/yr. As the majority of authigenic Fe burial in sediments appears to take place below 12 m depth, we take this value to be a conservative estimate for the authigenic Fe burial rate of the entire lake. For comparison, we estimated above in Section 5.1 that atmospheric surficial inputs may have delivered $\sim 2 \times 10^3$ g Fe/yr. Even accounting for seasonal variations in atmospheric Fe fluxes, this input flux is more than an order of magnitude lower than the conservative lower limit for the mass of authigenic Fe accumulating in deep lake sediments. This underlines that the dominant supplies of Fe to support high dFe and authigenic mineral accumulation at depth must be from subsurface groundwater fluxes that are large relative to the eolian flux.

Using the numerical integration described above, we estimate that the column-averaged, volume-weighted dissolved dFe for Deming Lake is 13-15 mg/L, and thus the total dissolved Fe load in the lake is 2.9-3.6×10⁶ g Fe. Assuming that authigenic burial below 12 m depth is the dominant output of Fe, we calculate a residence time of 55 to 148 years for Fe in Deming Lake. These residence times are approximately 200-600 times longer than the estimated water residence time of the lake (~90 days; Swanner et al., 2023a). This scaling factor between water and Fe residence times is considerably higher than estimates for another ferruginous meromictic lake, in

Canada, studied by Campbell and Torgersen (1980). They found an Fe residence time that was 4-5 times longer than that of lake water and conservative cations like Ca and K. Qualitatively, the elongated residence time of Fe in Deming Lake offers an explanation for why the water column dissolved dFe/dCa is more than an order of magnitude greater than the geochemically closest matching groundwater input of Elk Spring (**Section 5.1**). As recognized by Campbell and Torgersen (1980), effective redox cycling takes place between Fe²⁺_{aq}, which is oxidized upon upward approach to the oxycline, and reductive dissolution of sinking Fe³⁺ oxyhydroxide particles. Through cycling in this 'ferrous wheel', the same Fe can be retained in the water column for longer periods of time than conservative elements.

Because we see only limited net authigenic Fe sedimentation through formation of stable ferrous mineral phases deep in the anoxic monimolimnion, but groundwater recharge in the lake is vigorous (Swanner et al., 2023a), it is possible that an additional, or even dominant output flux of Fe from Deming Lake via groundwater outflow exists. In this scenario, Deming Lake itself could be acting as a pass-through for groundwater flow within permeable tunnel valley channel deposits that connect it to neighboring Arco and Josephine Lakes. In such a case, the relative enrichment of dFe/dCa in the Deming Lake water column compared to groundwater sources may provide another means to estimate the Fe residence time relative to the Ca residence time (equivalent to the water residence time). This would imply an Fe residence time of ~8 years ([dFe/dCa]_{lake}/[dFe/dCa]_{Elk} s_{pring} × 90 days). Coincidentally, a groundwater removal flux would likely have the same δ^{56} Fe as the major sedimentary removal flux to Layer (III) authigenic sediments, because the majority of the dissolved Fe pool in Deming Lake resides in waters below 12 m depth that are extremely Fe rich and impacted solely by precipitation of particles that are unfractionated with respect to δ^{56} Fe.

5.5. Lessons from Deming Lake as an Ancient Ocean Analog

The chemistry and Fe isotopic compositions of Deming Lake sediments suggest limited survival of Fe³⁺-bearing authigenic Fe precipitates through burial, most likely due to the extremely high sedimentary organic carbon contents (Lascu et al., 2012). The Deming Lake sedimentary record is thus a poor analog for Fe-rich, organic poor chemical sediments such as IFs formed in ancient ferruginous oceans. However, following the widely held assumption that chemical sediments like IFs are archives of mineral precipitation processes occurring in the water column (Konhauser et

al., 2017), it is possible that the dynamic cycling of Fe between dissolved and particulate pools in Deming Lake may still provide insight into the primary mineral precipitation processes that drove deposition of ancient ferruginous chemical sediments.

5.5.1. Implications for Fe Isotope Records of Sturtian Glacial Iron Formations

The most significant example of an ice-covered ferruginous water column in Earth history is the occurrence of synglacial IFs in sedimentary successions formed during the 717 to 661 Ma Sturtian glaciation (Macdonald et al., 2010; Rooney et al., 2020), the first Neoproterozoic Snowball Earth episode. Sturtian IF deposition is generally accepted to have been driven by the oxidation of ferruginous deep seawater established in snowball oceans through a lack of extensive ocean-atmosphere exchange, and Fe-rich, S-poor hydrothermal venting imposed by a depleted marine sulfate pool and lower mid-ocean-ridge overpressure (Kirschvink, 1992; Kump and Seyfried, 2005; Ilyin, 2009; Hoffman et al., 2017). It has been argued that $\text{Fe}^{2+}_{\text{aq}}$ oxidation near the continents was driven by the delivery of atmospheric O_2 beneath ice sheets, either into the surface ocean via atmospheric gas trapped in bubbles, or via meltwater streams at the grounding lines of glaciers (Lechte and Wallace, 2016; Busigny et al., 2018; Lechte et al., 2019). All Sturtian IFs are characterized by variable δ^{56} Fe values, extending to extremely positive values up to 2.7 % (Halverson et al., 2011; Cox et al., 2016; Busigny et al., 2018; Lechte et al., 2019). These values approach the theoretical equilibrium fractionation between Fe²⁺ and Fe³⁺ and have generally been interpreted to reflect low-degree partial oxidation under O_2 -limited conditions.

The muted Δ^{56} Fe_{p-d} range observed in the ice-covered March water column (Figs. 3H, 9) in Deming Lake suggests that this system does not represent a good analog for ferruginous snowball oceans, despite superficial similarities. Apparently, the ice-covered water column conditions at Deming Lake, extremely depleted in O_2 , are unconducive to the precipitation of purely ferric minerals with strongly positive δ^{56} Fe. In contrast, we observe large positive Δ^{56} Fe_{p-d} values in Layer (II) of the ice-free water columns of May and August, even in deeper waters where dFe is still in the mg/L range (Figs. 3, 9). The distinguishing feature of these water columns is the presence of an overlying, effectively infinite O_2 -rich layer that enables the precipitation of enough isotopically heavy Fe³⁺ for this to be the dominant particulate phase.

Qualitatively, our observations from Deming Lake support interpretations that isotopically heavy Sturtian IFs formed at redox gradients where Fe^{2+}_{aq} oxidation dominated the total particulate

Fe export to the seafloor. This dominant export of isotopically heavy Fe³⁺-bearing precipitates may either indicate that deep-water Fe²⁺_{aq} concentrations were too low for mixed valence mineral precipitation or Fe²⁺_{aq} adsorption to be significant, and/or that oxidants were sufficiently abundant for Fe³⁺ oxidation products to dominate the overall particulate Fe pool. In practical terms this constraint favors a concentrated and potentially open system delivery of oxidants that could maintain Fe³⁺ production during sustained upwelling of Fe²⁺-rich ocean waters. This favors oxidant supplies from subglacial streams at grounding lines or via atmospheric exchange in patches of ice-free open ocean, and disfavors models that feature a diffuse, closed system input of O₂ from air bubbles in the underside of marine ice sheets (Lechte and Wallace, 2016; Busigny et al., 2018; Lechte et al., 2019). It is worth noting that while reaction-transport models simulating the latter scenario can reproduce Sturtian IF δ^{56} Fe at sub-nanomolar dO₂ (Busigny et al., 2018), these models are not able to consider the isotopic consequences of such small Fe³⁺ precipitation fluxes in a stillferruginous water column where subsequent mixed-valence mineral formation and Fe²⁺_{aq} adsorption can take place (Fig. 9). Regardless of the source of oxidants, preservation of elevated δ^{56} Fe in Sturtian IFs must have required organic poor conditions in the water column and sediments, in contrast to the abundance of water column and sedimentary organic carbon in Deming Lake (Lascu et al., 2012).

5.5.2. Implications for Archean-Paleoproterozoic IF Depositional Processes

The canonical model for IF deposition prior to the Great Oxidation Event (GOE) ~2.4 Ga ago involves the oxidation of Fe²⁺_{aq} and precipitation of Fe³⁺-oxyhydroxide mineral precursors that underwent diagenetic transformations and later metamorphism to produce the assemblage of ferric and ferrous minerals observed in IFs today. In this model, Fe oxidation in the water column was driven by some combination of cyanobacterial O₂ (Cloud, 1973), anoxygenic photoferrotrophy (Konhauser et al., 2002; Kappler et al., 2005), and UV photo-oxidation (Braterman et al., 1983; François, 1986; Nie et al., 2017). The Fe isotopic record of IFs has generally been interpreted in the context of the large (1-3 ‰) fractionation that imparts positive δ^{56} Fe signatures to Fe³⁺ precipitates formed via any of these processes (Dauphas et al., 2017; Heard and Dauphas, 2020). A similarly large range in δ^{56} Fe values of Fe rich carbonates in IFs is generally explained in the context of this model through closed-system diagenetic transfer of Fe from Fe³⁺ precipitates to carbonates forming in the Archean-Paleoproterozoic sediment pile following microbial DIR

(Heimann et al., 2010; Craddock and Dauphas, 2011a). However, more recently Siahi et al. (2020), motivated by observations of primary Fe and Mn-bearing carbonate precipitation in the water columns of ferruginous lakes (Lambrecht et al., 2018; Vuillemin et al., 2020, 2022; Wittkop et al., 2020b), proposed that the carbonate-dominated 2.43 Ga Griquatown IF, South Africa, may have formed through water-column precipitation of the Fe-rich carbonates siderite and ankerite. Based on textural associations and chemical correlations of different carbonates within the Griquatown IF, Siahi et al. (2020) proposed that water-column DIR of sinking Fe³⁺-oxyhydroxides closely coupled with organic matter would have locally concentrated cations and DIC beneath the Paleoproterozoic ocean redoxcline and enabled saturation of carbonate minerals.

A test for any model for the genesis of variably carbonate-rich IFs should be its ability to reproduce negative log-linear correlations of Mn/Fe νs . δ^{56} Fe, which are widely observed in the largest early Paleoproterozoic IF successions of South Africa and Western Australia (Fig. 13; Haugaard et al., 2016; Heard et al., 2022; Kurzweil et al., 2016; Lantink et al., 2018; Thibon et al., 2019; Tsikos et al., 2010; Wang et al., 2023). In the canonical model, these relationships are interpreted in the context of a Rayleigh distillation-type evolution of an upwelling water mass on the margins of an IF-depositing basin, where the removal of Mn poor, high δ^{56} Fe Fe³⁺ oxyhydroxides produces progressively higher dMn/dFe, lower d δ^{56} Fe water masses from which subsequent ferric precipitates formed (Kurzweil et al., 2016; Thibon et al., 2019; Nie et al., 2020; Heard et al., 2022). The enclosed nature of Deming Lake compared to a laterally extensive IF depositional basin complicates any direct analogy being drawn between the two. However, Deming Lake data can reveal whether instantaneous dissolved-particulate fractionation of Mn/Fe and δ^{56} Fe in a ferruginous water column supports such a simple distillation model for early Paleoproterozoic IF Mn/Fe νs . δ^{56} Fe systematics (Fig. 13).

Ferric oxyhydroxide formation in Layer (II) imparts a clear negative log-linear correlation in dMn/Fe vs. d δ^{56} Fe (Fig. 13A-D). This is consistent with the expectations for a distillation process driven by removal of isotopically heavy, low Mn/Fe particulates (Nie et al., 2020; Heard et al., 2022). However, particulate data do not follow a complementary negative correlation in this space (Fig. 13A-C; E). Therefore, correlations in the dissolved phase likely only reflect Fe removal, with limited partitioning of Mn into particulates leaving most Mn remaining in solution and not systematically tracking the evolution of dMn/dFe. Taken at face value, this is evidence against a simple Fe³⁺ oxyhydroxide precursor as the driver of Mn/Fe vs. δ^{56} Fe systematics in pre-GOE IFs.

Conversely, Δ^{56} Fe_{p-d} values in Layer (III) of Deming Lake are generally near-zero, and dMn/dFe and pMn/pFe are within a factor of two (Fig. 3). We estimated in **Section 5.2.3** that a large fraction of pFe in Layer (III) is carbonate-hosted. This carbonate appears to be a reasonable archive of $d\delta^{56}$ Fe and dMn/dFe. If such relationships held in the pre-GOE ferruginous oceans, water column carbonates could provide a reasonable archive of seawater $d\delta^{56}$ Fe or dMn/dFe values. Carbonate precipitates could not, however, have driven the large and correlated δ^{56} Fe and Mn/Fe variability seen in major early Paleoproterozoic IF successions.

We therefore speculate that while behaviors expressed by endmember Fe^{3+} oxyhydroxide and carbonate-dominated particulates in Deming Lake may each be responsible for, or record, some aspect of ferruginous water column dMn/dFe vs. d δ^{56} Fe evolution envisaged in Paleoproterozoic IF models (Fig. 13A; Heard et al., 2022; Kurzweil et al., 2016; Thibon et al., 2019; Tsikos et al., 2010), neither phase alone can reproduce the desired trends shown in Figure 13F. We therefore suggest that geochemical studies into the origin of IFs will benefit from more explicitly exploring the simultaneous deposition of multiple mineral precipitates. These studies should include authigenic Fe-bearing phyllosilicates, which have a dominant proposed role in more recent alternative models for IF deposition (Rasmussen et al., 2021, and references therein), and for which the trace element and Fe isotopic fractionation behavior are in the nascent stages of being explored (Heard et al., 2023; Tostevin and Ahmed, 2023).

5.6. Triple Fe Isotope Mass Fractionation Law for Aqueous Fe Oxidation in Nature

Triple Fe isotope data for dFe within the Layer (II) oxidation interval defined a slope in ϵ^{156} Fe vs. δ^{157} Fe space that corresponds to $\theta^{56/57} = 0.6788 \pm 0.0010$ (Fig. 4). This value falls within error of the slope for the theoretical high-temperature equilibrium law with $\theta^{56/57}_{eq} = 0.678$ (Young et al., 2002; Dauphas and Schauble, 2016); the slope measured for UV-photooxidation of Fe^{2+}_{aq} with $\theta^{56/57}_{UV} = 0.6785 \pm 0.0010$ (Nie et al., 2017); and the slope measured for an array of highly fractioned pre-GOE IFs with $\theta^{56/57} = 0.6779 \pm 0.0006$ (Heard et al., 2020). As the oxidant for Fe^{2+}_{aq} in Layer (II) in at least the most strongly fractionated portion of the lake is mostly dissolved O_2 (Fig. 8), high precision $\theta^{56/57}$ values have now been recorded for two (O_2 , UV photons) of the three widely hypothesized oxidants to drive Fe^{3+} -oxyhydroxide formation and the deposition of IFs before the GOE (Cloud, 1973; Braterman et al., 1983; Nie et al., 2017), with only direct microbial oxidation by anoxygenic photoferrotrophy remaining to be explored with these measurements. The

values of $\theta^{56/57}$ are apparently indistinguishable for O_2 and UV oxidation, and both agree with the theoretical high-temperature equilibrium law (Young et al., 2002; Dauphas and Schauble, 2016), which suggests that regardless of abiotic oxidation mechanism, Fe^{2+}_{aq} and Fe^{3+} precipitates produced during oxidation reach isotopic equilibrium.

It is unlikely that high-precision triple Fe isotope measurements will be able to identify the dominant oxidation mechanism involved in the deposition of pre-GOE IFs, if indeed they did form as oxide precipitates. However, two outstanding details need resolving before this proxy approach can be fully disregarded as a means to determine pre-GOE oxidation pathways. First, it will be imperative to conduct Fe²⁺_{aq} oxidation experiments in photoferrotrophy cultures and make high precision ϵ^{156} Fe vs. δ^{157} Fe measurements of the reactants and products, to confidently assert that this oxidation mechanism also follows the $\theta^{56/57}$ for isotopic equilibrium. This result is expected. because of the similar δ^{56} Fe systematics of previous photoferrotrophy experiments to the results of other oxidation pathways (Croal et al., 2004; Swanner et al., 2015b). Second, some of the most highly fractionated Fe isotope data for IFs that are observed to adhere to the equilibrium MFL (Heard et al., 2020), derive from Mn-rich deposits formed at the onset of the GOE or in earlier 'oxygen oases' (Tsikos et al., 2010; Planavsky et al., 2014). Such samples are the most likely IFs to record the impact of O₂-driven Fe²⁺_{aq} oxidation. However, if other oxidation mechanisms were also important for the deposition of less Mn-rich IFs, and if extensive analysis of these more 'typical' IFs reveals any diversity in $\theta^{56/57}$ values, this may be attributable to a distinct photoferrotrophy MFL, and, thus, a different formation pathway for IFs deposited at different times in Earth history (Wang et al., 2023).

12811282

1283

1284

1285

1286

1287

1288

1289

1290

1261

1262

1263

1264

1265

1266

1267

1268

1269

1270

1271

1272

1273

1274

1275

1276

1277

1278

1279

1280

6. Conclusions

We present the Fe isotopic and selected chemical characteristics of sediments, putative sources, and seasonal dissolved and particulate phases from the water column of Deming Lake, a small ferruginous meromictic lake that undergoes seasonal surface freezing. Deming Lake is an endmember site to study Fe cycling in purely ferruginous conditions due to its negligible sulfur pool, making it an excellent natural laboratory for investigating water column and early diagenetic processes in a setting analogous to that which may have dominated the oceans for large swathes of Earth history.

Deming Lake is dominantly supplied its Fe by a groundwater source at depth and maintains a strong chemocline beneath 12 meters water depth. A Ca-Mg-carbonate-type groundwater is likely the dominant source of Fe to the lake, with locally accessible springs providing examples of waters with Fe isotopic and major dissolved elemental ratios that are a good match for the groundwater source to Deming Lake. Modest eolian inputs at its surface deliver a few percent of the total Fe burial flux at depth on an annual basis.

Under ice-free conditions, Deming Lake features a \sim 6 meter deep oxic surface layer, with a subsurface chlorophyll maximum layer residing around the oxycline. Within the upper oxic layer, the dissolved Fe pool is low in concentration and isotopically heavy relative to particles, reflecting the uptake of isotopically light dissolved Fe into particulate biomass with seasonally variable additions of eolian lithogenic material. Deeper, Fe-rich waters in the Deming Lake water column are rapidly depleted in dFe and $d\delta^{56}$ Fe by oxidation on approach to the oxycline and removal to an isotopically heavy particulate phase likely dominated by Fe³⁺-oxyhydroxides. Oxidation and removal of isotopically heavy Fe begins several meters beneath the oxycline and may reveal the activity of microaerophilic Fe oxidizers or anoxygenic photoferrotrophs in addition to direct O₂ oxidation of Fe²⁺_{aq} at shallower depths. Beneath the \sim 12 m deep chemocline, extremely high dissolved concentrations of Fe, P, Ca, Mg, and Mn, support the supersaturation and precipitation of the Fe²⁺ phosphate vivianite, and a mixed assemblage of Fe-, Ca-, Mg-, and Mn-bearing carbonates. Iron isotopic fractionations between dissolved and particulate Fe are close to zero in the water column below 12 m, suggesting that both vivianite and a range of authigenic carbonate compositions may be faithful recorders of water column Fe isotopic compositions.

Under ice cover in the winter, the oxycline shallows to <3 m, bringing elevated dFe to shallower depths. Less fractionated, and more vertically homogeneous Fe chemical and isotopic profiles in the winter-time water column likely reflect fall-time vertical mixing and homogenization of Layers (I) and (II), driven by thermocline collapse. Calculations show that the winter dFe and $d\delta^{56}$ Fe profiles can be approximately reproduced by vertical homogenization of the May or August water columns above 10 m depth, followed by precipitation and removal of a few tens of % of the dFe that is mixed upward into the shallowest waters.

Despite large Fe isotopic fractionations between dissolved Fe and sinking particles in the Deming Lake water column, authigenic Fe enrichments only survive in lake floor sediments deposited below >12 m water depth. This is likely a result of the high organic burial rates in

Deming Lake that enable effective DIR of Fe³⁺-bearing authigenic precipitates deposited above the chemocline. We estimate that the annual authigenic Fe burial flux on the Deming Lake floor underlying water depths of >12 m is more than an order of magnitude greater than the lithogenic input flux of Fe at the lake surface, necessitating a dominant Fe source from groundwater. Using this Fe output flux, we estimate a water column residence time of dissolved Fe in the lake of between 50 and 150 years.

Fractionations in δ^{56} Fe and Mn/Fe between dissolved and particulate pools in the Deming Lake water column can provide insights on the origin of organic-poor iron formations from different episodes in the Precambrian. By comparison with particulate δ^{56} Fe systematics near the oxycline in ice-free and ice-covered water columns at Deming Lake, we suggest that isotopically heavy IF deposited during the Sturtian Snowball Earth glaciation must have formed in the presence of sufficient oxidants to prevent mixed-valence Fe particle formation under high dissolved Fe²⁺ conditions. Meanwhile, through a comparison of dissolved and particulate systematics in Deming Lake with extensive early Paleoproterozoic IFs formed shortly before the GOE in South Africa and Western Australia, we suggest that simultaneous burial of more than one authigenic Fe phase is required to explain negative δ^{56} Fe νs . Mn/Fe trends observed in these IFs.

Acknowledgements

This work was supported by an Agouron Postdoctoral Fellowship (to AWH), NSF-EAR 2129034 (to CMO, SGN), NSF-EAR 1944946 and NSF-EAR 2128939 (to EDS), and the WHOI Postdoctoral Scholarship program (to AWH, CMO). Sajjad Akam, Michelle Chamberlain, Guy Evans, and Zak Stevenson are thanked for helping during sample collection. We thank Chris Harding for providing an updated bathymetric dataset and map of Deming Lake. We thank staff at the University of Minnesota Itasca Biological Station, particularly Director Jonathan Schilling for logistical support, and the catering staff. Jurek Blusztajn and Gretchen Swarr are thanked for analytical support. AWH thanks Nicolas Dauphas for supplying generous quantities of the IRMM-524 and IF-G geostandard materials that made the re-establishment of high-precision iron isotopic analyses at WHOI possible. Sarah Aarons is thanked for advice on clean handling of ice core material. This manuscript benefited from thoughtful discussions with Colleen Hansel and Yi Wang.

- **CRediT Author Statement** 1353
- Andy W. Heard: Conceptualization, Investigation, Writing Original Draft, Visualization 1354
- 1355 Chadlin M. Ostrander: Resources, Investigation, Writing – Review & Editing, Funding
- Acquisition Elizabeth D. Swanner: Resources, Investigation, Writing Review and Editing, 1356
- Funding Acquisition Kathryn Rico: Investigation, Writing Review and Editing, Sune G. 1357
- **Nielsen** Resources, Writing Review & Editing, Supervision, Funding Acquisition. 1358

1360

1361

Data Availability

Data are available through Mendeley Data at: https://doi.org/10.17632/pthxwdtfzz.1 1362

1363 1364

References

- 1365 Akam S. A., Chuang P.-C., Katsev S., Wittkop C., Chamberlain M., Dale A. W., Wallmann K., Heathcote 1366 A. J. and Swanner E. D. (2024) Methane-carbon budget of a ferruginous meromictic lake and 1367 implications for marine methane dynamics on early Earth. Geology.
- 1368 Al-Borno A. and Tomson M. B. (1994) The temperature dependence of the solubility product constant of vivianite. Geochim. Cosmochim. Acta 58, 5373-5378. 1369
- Altmann H. J. (1972) Bestimmung von in Wasser gelöstem Sauerstoff mit Leukoberbelinblau I. Fresenius 1370 1371 Z. Für Anal. Chem. 262, 97-99.
- Baker A. and Brook A. (1971) Optical density profiles as an aid to the study of microstratified 1372 phytoplankton populations in lakes. Arch. Für Hydrobiol. 69, 214–233. 1373
- 1374 Balci N., Bullen T. D., Witte-Lien K., Shanks W. C., Motelica M. and Mandernack K. W. (2006) Iron isotope fractionation during microbially stimulated Fe(II) oxidation and Fe(III) precipitation. 1375 Geochim. Cosmochim. Acta 70, 622-639. 1376
- Bauer K. W., Byrne J. M., Kenward P., Simister R. L., Michiels C. C., Friese A., Vuillemin A., Henny C., 1377 Nomosatryo S., Kallmeyer J., Kappler A., Smit M. A., Francois R. and Crowe S. A. (2020) 1378 Magnetite biomineralization in ferruginous waters and early Earth evolution. Earth Planet. Sci. 1379 1380 Lett. 549, 116495.
- Beard B. L., Handler R. M., Scherer M. M., Wu L., Czaja A. D., Heimann A. and Johnson C. M. (2010) 1381 1382 Iron isotope fractionation between aqueous ferrous iron and goethite. Earth Planet. Sci. Lett. 295, 241-250. 1383
- 1384 Beard B. L., Johnson C. M., Cox L., Sun H., Nealson K. H. and Aguilar C. (1999) Iron Isotope 1385 Biosignatures. *Science* **285**, 1889–1892.
- Bekker A., Slack J. F., Planavsky N., Krapež B., Hofmann A., Konhauser K. O. and Rouxel O. J. (2010) 1386 1387 Iron Formation: The Sedimentary Product of a Complex Interplay among Mantle, Tectonic, Oceanic, and Biospheric Processes. Econ. Geol. 105, 467–508. 1388
- Benner S. G., Hansel C. M., Wielinga B. W., Barber T. M. and Fendorf S. (2002) Reductive Dissolution 1389 1390 and Biomineralization of Iron Hydroxide under Dynamic Flow Conditions. Environ. Sci. Technol. 1391 **36**, 1705–1711.
- Bethke C. M. (2022) Geochemical and Biogeochemical Reaction Modeling. 3rd ed., Cambridge 1392 1393 University Press, Cambridge.
- 1394 Bishop J. K. B. and Wood T. J. (2008) Particulate matter chemistry and dynamics in the twilight zone at 1395 VERTIGO ALOHA and K2 sites. Deep Sea Res. Part Oceanogr. Res. Pap. 55, 1684–1706.

- Braterman P. S., Cairns-Smith A. G. and Sloper R. W. (1983) Photo-oxidation of hydrated Fe2+—significance for banded iron formations. *Nature* **303**, 163–164.
- Bullen T. D., White A. F., Childs C. W., Vivit D. V. and Schulz M. S. (2001) Demonstration of significant abiotic iron isotope fractionation in nature. *Geology* **29**, 699–702.
- Busigny V., Planavsky N. J., Goldbaum E., Lechte M. A., Feng L. and Lyons T. W. (2018) Origin of the Neoproterozoic Fulu iron formation, South China: Insights from iron isotopes and rare earth element patterns. *Geochim. Cosmochim. Acta* **242**, 123–142.
 - Busigny V., Planavsky N. J., Jézéquel D., Crowe S., Louvat P., Moureau J., Viollier E. and Lyons T. W. (2014) Iron isotopes in an Archean ocean analogue. *Geochim. Cosmochim. Acta* **133**, 443–462.
 - Campbell P. and Torgersen T. (1980) Maintenance of Iron Meromixis by Iron Redeposition in a Rapidly Flushed Monimolimnion. *Can. J. Fish. Aguat. Sci.* **37**, 1303–1313.
 - Chan C. S., Emerson D. and Luther III G. W. (2016) The role of microaerophilic Fe-oxidizing microorganisms in producing banded iron formations. *Geobiology* **14**, 509–528.
- 1409 Church T., Tillotson M. and Wendler L. (1989) *Survey of the meromictic Demming Lake*., University of 1410 Minnesota.
 - Cloud P. (1973) Paleoecological Significance of the Banded Iron-Formation. *Econ. Geol.* **68**, 1135–1143.
- 1412 Cosmidis J., Benzerara K., Morin G., Busigny V., Lebeau O., Jézéquel D., Noël V., Dublet G. and
 1413 Othmane G. (2014) Biomineralization of iron-phosphates in the water column of Lake Pavin
 1414 (Massif Central, France). *Geochim. Cosmochim. Acta* 126, 78–96.
 - Cox G. M., Halverson G. P., Poirier A., Le Heron D., Strauss J. V. and Stevenson R. (2016) A model for Cryogenian iron formation. *Earth Planet. Sci. Lett.* **433**, 280–292.
 - Craddock P. R. and Dauphas N. (2011a) Iron and carbon isotope evidence for microbial iron respiration throughout the Archean. *Earth Planet. Sci. Lett.* **303**, 121–132.
 - Craddock P. R. and Dauphas N. (2011b) Iron Isotopic Compositions of Geological Reference Materials and Chondrites. *Geostand. Geoanalytical Res.* **35**, 101–123.
 - Croal L. R., Johnson C. M., Beard B. L. and Newman D. K. (2004) Iron isotope fractionation by Fe(II)-oxidizing photoautotrophic bacteria 1. *Geochim. Cosmochim. Acta* **68**, 1227–1242.
 - Crosby, Roden Eric E., Johnson Clark M., and Beard Brian L. (2007) The mechanisms of iron isotope fractionation produced during dissimilatory Fe(III) reduction by Shewanella putrefaciens and Geobacter sulfurreducens. *Geobiology* **5**, 169–189.
 - Crowe S. A., Katsev S., Leslie K., Sturm A., Magen C., Nomosatryo S., Pack M. A., Kessler J. D., Reeburgh W. S., Roberts J. A., González L., Douglas Haffner G., Mucci A., Sundby B. and Fowle D. A. (2011) The methane cycle in ferruginous Lake Matano: Methane cycle in ferruginous Lake Matano. *Geobiology* **9**, 61–78.
- 1430 Crowe S. A., Maresca J. A., Jones C., Sturm A., Henny C., Fowle D. A., Cox R. P., Delong E. F. and
 1431 Canfield D. E. (2014) Deep-water anoxygenic photosythesis in a ferruginous chemocline.
 1432 *Geobiology* 12, 322–339.
- 1433 Crowe S. A., O'Neill A. H., Katsev S., Hehanussa P., Haffner G. D., Sundby B., Mucci A. and Fowle D.
 1434 A. (2008) The biogeochemistry of tropical lakes: A case study from Lake Matano, Indonesia.
 1435 Limnol. Oceanogr. 53, 319–331.
- Czaja A. D., Johnson C. M., Roden E. E., Beard B. L., Voegelin A. R., Nägler T. F., Beukes N. J. and
 Wille M. (2012) Evidence for free oxygen in the Neoarchean ocean based on coupled iron—molybdenum isotope fractionation. *Geochim. Cosmochim. Acta* 86, 118–137.
- Dauphas N., Heard A. W., Rego E. S., Rouxel O., Marin-Carbonne J., Pasquier V., Bekker A. and Rowley D. (2024) Past and present dynamics of the iron biogeochemical cycle. In *Reference Module in Earth Systems and Environmental Sciences* Elsevier.
- Dauphas N., Janney P. E., Mendybaev R. A., Wadhwa M., Richter F. M., Davis A. M., van Zuilen M.,
 Hines R. and Foley C. N. (2004a) Chromatographic Separation and Multicollection-ICPMS
 Analysis of Iron. Investigating Mass-Dependent and -Independent Isotope Effects. *Anal. Chem.*

76, 5855–5863.

1403

1404

1405

1406 1407

1408

1411

1415

1416

1417 1418

1419

1420

1421

14221423

1424

1425 1426

14271428

- Dauphas N., John S. G. and Rouxel O. (2017) Iron Isotope Systematics. *Rev. Mineral. Geochem.* **82**, 415–1447 510.
- Dauphas N., Pourmand A. and Teng F.-Z. (2009) Routine isotopic analysis of iron by HR-MC-ICPMS: How precise and how accurate? *Chem. Geol.* **267**, 175–184.
- Dauphas N. and Schauble E. A. (2016) Mass Fractionation Laws, Mass-Independent Effects, and Isotopic Anomalies. *Annu. Rev. Earth Planet. Sci.* **44**, 709–783.
- Dauphas N., Zuilen M. van, Wadhwa M., Davis A. M., Marty B. and Janney P. E. (2004b) Clues from Fe
 Isotope Variations on the Origin of Early Archean BIFs from Greenland. *Science* **306**, 2077–
 2080.
- Ellwood M. J., Hassler C., Moisset S., Pascal L., Danza F., Peduzzi S., Tonolla M. and Vance D. (2019)
 Iron isotope transformations in the meromictic Lake Cadagno. *Geochim. Cosmochim. Acta* **255**, 205–221.
- Ellwood M. J., Strzepek R. F., Strutton P. G., Trull T. W., Fourquez M. and Boyd P. W. (2020) Distinct iron cycling in a Southern Ocean eddy. *Nat. Commun.* 11, 825.
 - Eroglu S., Schoenberg R., Pascarelli S., Beukes N. J., Kleinhanns I. C. and Swanner E. D. (2018) Open ocean vs. continentally-derived iron cycles along the Neoarchean Campbellrand-Malmani Carbonate platform, South Africa. *Am. J. Sci.* **318**, 367–408.
 - François L. M. (1986) Extensive deposition of banded iron formations was possible without photosynthesis. *Nature* **320**, 352–354.

1461

1462 1463

1464

1465

1466

1467 1468

1469

14701471

14721473

1474

1475

1479

1480 1481

1482

1483

1484

1485

- Friese A., Bauer K., Glombitza C., Ordoñez L., Ariztegui D., Heuer V. B., Vuillemin A., Henny C., Nomosatryo S., Simister R., Wagner D., Bijaksana S., Vogel H., Melles M., Russell J. M., Crowe S. A. and Kallmeyer J. (2021) Organic matter mineralization in modern and ancient ferruginous sediments. *Nat. Commun.* 12, 2216.
 - Gadol H. J., Elsherbini J. and Kocar B. D. (2022) Methanogen Productivity and Microbial Community Composition Varies With Iron Oxide Mineralogy. *Front. Microbiol.* **12**.
 - Gadol H. J., Ostrander C. M., Villarroel L., Taenzer L., Wankel S. D., Carignan V. E. and Hansel C. M. (2023) Particle- and Light-Mediated Processes Control Seasonal Manganese Oxide Cycling in a Meromictic Pond. *ACS Earth Space Chem.* 7, 1181–1194.
 - Gorham E. and Boyce F. M. (1989) Influence of Lake Surface Area and Depth Upon Thermal Stratification and the Depth of the Summer Thermocline. *J. Gt. Lakes Res.* **15**, 233–245.
- Gumsley A. P., Chamberlain K. R., Bleeker W., Söderlund U., Kock M. O. de, Larsson E. R. and Bekker A. (2017) Timing and tempo of the Great Oxidation Event. *Proc. Natl. Acad. Sci.* **114**, 1811–1816.
 - Halevy I., Alesker M., Schuster E. M., Popovitz-Biro R. and Feldman Y. (2017) A key role for green rust in the Precambrian oceans and the genesis of iron formations. *Nat. Geosci.* **10**, 135–139.
 - Halverson G. P., Poitrasson F., Hoffman P. F., Nédélec A., Montel J.-M. and Kirby J. (2011) Fe isotope and trace element geochemistry of the Neoproterozoic syn-glacial Rapitan iron formation. *Earth Planet. Sci. Lett.* **309**, 100–112.
 - Haugaard R., Pecoits E., Lalonde S., Rouxel O. and Konhauser K. (2016) The Joffre banded iron formation, Hamersley Group, Western Australia: Assessing the palaeoenvironment through detailed petrology and chemostratigraphy. *Precambrian Res.* **273**, 12–37.
- Heard A. W., Bekker A., Kovalick A., Tsikos H., Ireland T. and Dauphas N. (2022) Oxygen production
 and rapid iron oxidation in stromatolites immediately predating the Great Oxidation Event. *Earth Planet. Sci. Lett.* 582, 117416.
- Heard A. W. and Dauphas N. (2020) Constraints on the coevolution of oxic and sulfidic ocean iron sinks from Archean–Paleoproterozoic iron isotope records. *Geology* **48**, 358–362.
- Heard A. W., Dauphas N., Guilbaud R., Rouxel O. J., Butler I. B., Nie N. X. and Bekker A. (2020) Triple
 iron isotope constraints on the role of ocean iron sinks in early atmospheric oxygenation. *Science* 370, 446–449.
- Heard A. W., Dauphas N., Hinz I. L., Johnson J. E., Blanchard M., Alp E. E., Hu M. Y., Zhao J., Lavina
 B., Fornace M. E., Hu J. Y., Roskosz M., Kin I Sio C., Nie N. X. and Baptiste B. (2023) Isotopic

- 1497 Constraints on the Nature of Primary Precipitates in Archean–Early Paleoproterozoic Iron
 1498 Formations from Determinations of the Iron Phonon Density of States of Greenalite and 2L- and
 1499 6L-Ferrihydrite. *ACS Earth Space Chem.* 7, 712–727.
- Heimann A., Johnson C. M., Beard B. L., Valley J. W., Roden E. E., Spicuzza M. J. and Beukes N. J. (2010) Fe, C, and O isotope compositions of banded iron formation carbonates demonstrate a major role for dissimilatory iron reduction in ~2.5 Ga marine environments. *Earth Planet. Sci. Lett.* **294**, 8–18.
- Herndon E. M., Havig J. R., Singer D. M., McCormick M. L. and Kump L. R. (2018) Manganese and
 iron geochemistry in sediments underlying the redox-stratified Fayetteville Green Lake. *Geochim. Cosmochim. Acta* 231, 50–63.
 - Hinz I. L., Nims C., Theuer S., Templeton A. S. and Johnson J. E. (2021) Ferric iron triggers greenalite formation in simulated Archean seawater. *Geology* **49**, 905–910.
- Hoffman P. F., Abbot D. S., Ashkenazy Y., Benn D. I., Brocks J. J., Cohen P. A., Cox G. M., Creveling J.
 R., Donnadieu Y., Erwin D. H., Fairchild I. J., Ferreira D., Goodman J. C., Halverson G. P.,
 Jansen M. F., Le Hir G., Love G. D., Macdonald F. A., Maloof A. C., Partin C. A., Ramstein G.,
 Rose B. E. J., Rose C. V., Sadler P. M., Tziperman E., Voigt A. and Warren S. G. (2017)
 Snowball Earth climate dynamics and Cryogenian geology-geobiology. *Sci. Adv.* 3, e1600983.
 - Holland H. D. (1984) *The Chemical Evolution of the Atmosphere and Oceans*., Princeton University Press.
 - Hopp T., Dauphas N., Spitzer F., Burkhardt C. and Kleine T. (2022) Earth's accretion inferred from iron isotopic anomalies of supernova nuclear statistical equilibrium origin. *Earth Planet. Sci. Lett.* 577, 117245.
- 1519 Ilyin A. V. (2009) Neoproterozoic banded iron formations. *Lithol. Miner. Resour.* 44, 78.

1514

1515 1516

1517 1518

1520

15211522

1526 1527

- Jochum K. P., Weis U., Schwager B., Stoll B., Wilson S. A., Haug G. H., Andreae M. O. and Enzweiler J. (2016) Reference Values Following ISO Guidelines for Frequently Requested Rock Reference Materials. *Geostand. Geoanalytical Res.* **40**, 333–350.
- Johnson C. M., Roden E. E., Welch S. A. and Beard B. L. (2005) Experimental constraints on Fe isotope fractionation during magnetite and Fe carbonate formation coupled to dissimilatory hydrous ferric oxide reduction. *Geochim. Cosmochim. Acta* **69**, 963–993.
 - Johnson C. M., Skulan J. L., Beard B. L., Sun H., Nealson K. H. and Braterman P. S. (2002) Isotopic fractionation between Fe(III) and Fe(II) in aqueous solutions. *Earth Planet. Sci. Lett.* **195**, 141–153.
- Jones C., Crowe S. A., Sturm A., Leslie K. L., MacLean L. C. W., Katsev S., Henny C., Fowle D. A. and
 Canfield D. E. (2011) Biogeochemistry of manganese in ferruginous Lake Matano, Indonesia.
 Biogeosciences 8, 2977–2991.
- Kappler A., Pasquero C., Konhauser K. O. and Newman D. K. (2005) Deposition of banded iron formations by anoxygenic phototrophic Fe(II)-oxidizing bacteria. *Geology* **33**, 865–868.
- Kirschvink J. L. (1992) Late Proterozoic Low-Latitude Global Glaciation: the Snowball Earth. In *J. W.* Schopf & C. Klein (eds.), The Proterozoic Biosphere: A Multidisciplinary Study Cambridge
 University Press.
- Konhauser K. O., Hamade T., Raiswell R., Morris R. C., Ferris F. G., Southam G. and Canfield D. E. (2002) Could bacteria have formed the Precambrian banded iron formations? *Geology* **30**, 1079–1082.
- Konhauser K. O., Planavsky N. J., Hardisty D. S., Robbins L. J., Warchola T. J., Haugaard R., Lalonde S.
 V., Partin C. A., Oonk P. B. H., Tsikos H., Lyons T. W., Bekker A. and Johnson C. M. (2017)
 Iron formations: A global record of Neoarchaean to Palaeoproterozoic environmental history.
 Earth-Sci. Rev. 172, 140–177.
- Kump L. R. and Seyfried W. E. (2005) Hydrothermal Fe fluxes during the Precambrian: Effect of low oceanic sulfate concentrations and low hydrostatic pressure on the composition of black smokers. *Earth Planet. Sci. Lett.* **235**, 654–662.

- Kurzweil F., Wille M., Gantert N., Beukes N. J. and Schoenberg R. (2016) Manganese oxide shuttling in pre-GOE oceans evidence from molybdenum and iron isotopes. *Earth Planet. Sci. Lett.* **452**, 69–78.
- Lambrecht N., Wittkop C., Katsev S., Fakhraee M. and Swanner E. D. (2018) Geochemical
 Characterization of Two Ferruginous Meromictic Lakes in the Upper Midwest, USA. *J. Geophys. Res. Biogeosciences* 123, 3403–3422.
- Lantink M. L., Oonk P. B. H., Floor G. H., Tsikos H. and Mason P. R. D. (2018) Fe isotopes of a 2.4 Ga hematite-rich IF constrain marine redox conditions around the GOE. *Precambrian Res.* **305**, 218–235.
- Lascu I., McLauchlan K. K., Myrbo A., Leavitt P. R. and Banerjee S. K. (2012) Sediment-magnetic
 evidence for last millennium drought conditions at the prairie–forest ecotone of northern United
 States. *Palaeogeogr. Palaeoclimatol. Palaeoecol.* 337–338, 99–107.
- Lechte M. A., Wallace M. W., Hood A. van S., Li W., Jiang G., Halverson G. P., Asael D., McColl S. L.
 and Planavsky N. J. (2019) Subglacial meltwater supported aerobic marine habitats during
 Snowball Earth. *Proc. Natl. Acad. Sci.*
- Lechte M. and Wallace M. (2016) Sub–ice shelf ironstone deposition during the Neoproterozoic Sturtian glaciation. *Geology* **44**, 891–894.
- Liu K., Schiff S. L., Wu L., Molot L. A., Venkiteswaran J. J., Paterson M. J., Elgood R. J., Tsuji J. M. and Neufeld J. D. (2022) Large Fractionation in Iron Isotopes Implicates Metabolic Pathways for Iron Cycling in Boreal Shield Lakes. *Environ. Sci. Technol.* **56**, 14840–14851.
 - Liu X.-M., Gaschnig R. M., Rudnick R. L., Hazen R. M. and Shahar A. (2022) Constant iron isotope composition of the upper continental crust over the past 3 Gyr. *Geochem. Perspect. Lett.* **22**, 16–19.
- Macdonald F. A., Schmitz M. D., Crowley J. L., Roots C. F., Jones D. S., Maloof A. C., Strauss J. V.,
 Cohen P. A., Johnston D. T. and Schrag D. P. (2010) Calibrating the Cryogenian. *Science* 327,
 1241–1243.
- Malinovsky D. N., Rodyushkin I. V., Shcherbakova E. P., Ponter C., Öhlander B. and Ingri J. (2005) Fractionation of Fe Isotopes As a Result of Redox Processes in a Basin. **43**.
 - McLauchlan K. K., Lascu I., Myrbo A. and Leavitt P. R. (2013) Variable ecosystem response to climate change during the Holocene in northern Minnesota, USA. *GSA Bull.* **125**, 445–452.
- Megard R. O., Bradbury J. P. and Dean W. E. (1993) Climatic and limnologic setting of Elk Lake. In *Elk Lake, Minnesota: Evidence for Rapid Climate Change in the North-Central United States* (eds. J.
 Piatt Bradbury and W. E. Dean). Geological Society of America. p. 0.
- 1580 Millero F. J. (1998) Solubility of Fe(III) in seawater. Earth Planet. Sci. Lett. 154, 323–329.

1568 1569

1575

- Millero F. J., Sotolongo S. and Izaguirre M. (1987) The oxidation kinetics of Fe(II) in seawater. *Geochim. Cosmochim. Acta* **51**, 793–801.
- Mulholland D. S., Poitrasson F., Shirokova L. S., González A. G., Pokrovsky O. S., Boaventura G. R. and Vieira L. C. (2015) Iron isotope fractionation during Fe(II) and Fe(III) adsorption on cyanobacteria. *Chem. Geol.* **400**, 24–33.
- Nie N. X., Dauphas N. and Greenwood R. C. (2017) Iron and oxygen isotope fractionation during iron
 UV photo-oxidation: Implications for early Earth and Mars. *Earth Planet. Sci. Lett.* **458**, 179–
 1588
- Nie N. X., Dauphas N., Villalon K. L., Liu N., Heard A. W., Morris R. V. and Mertzman S. A. (2020)

 Iron isotopic and chemical tracing of basalt alteration and hematite spherule formation in Hawaii:

 A prospective study for Mars. *Earth Planet. Sci. Lett.* **544**, 116385.
- Oldham V. E., Owings S. M., Jones M. R., Tebo B. M. and Luther G. W. (2015) Evidence for the presence of strong Mn(III)-binding ligands in the water column of the Chesapeake Bay. *Mar. Chem.* **171**, 58–66.
- Planavsky N. J., Asael D., Hofmann A., Reinhard C. T., Lalonde S. V., Knudsen A., Wang X., Ossa Ossa F., Pecoits E., Smith A. J. B., Beukes N. J., Bekker A., Johnson T. M., Konhauser K. O., Lyons

- T. W. and Rouxel O. J. (2014) Evidence for oxygenic photosynthesis half a billion years before the Great Oxidation Event. *Nat. Geosci.* 7, 283–286.
- Planavsky N., Rouxel O. J., Bekker A., Hofmann A., Little C. T. S. and Lyons T. W. (2012) Iron isotope composition of some Archean and Proterozoic iron formations. *Geochim. Cosmochim. Acta* **80**, 158–169.
- Poulton S. W., Bekker A., Cumming V. M., Zerkle A. L., Canfield D. E. and Johnston D. T. (2021) A 200-million-year delay in permanent atmospheric oxygenation. *Nature*, 1–5.

1605

1606

1607 1608

1609

1610

1615 1616

1617

1618 1619

1620

1621 1622

1623 1624

1625

1626 1627

- Poulton S. W. and Canfield D. E. (2011) Ferruginous Conditions: A Dominant Feature of the Ocean through Earth's History. *Elements* 7, 107–112.
- Raiswell R., Hardisty D. S., Lyons T. W., Canfield D. E., Owens J. D., Planavsky N. J., Poulton S. W. and Reinhard C. T. (2018) The iron paleoredox proxies: A guide to the pitfalls, problems and proper practice. *Am. J. Sci.* **318**, 491–526.
- Rasmussen B., Muhling J. R. and Krapež B. (2021) Greenalite and its role in the genesis of early Precambrian iron formations A review. *Earth-Sci. Rev.*, 103613.
- 1611 Reiter C., Schmitz J. and Helfman S. (1998) *A limnological study of Deming Lake.*, University of Minnesota.
- Rico K. I., Ostrander C. M., Heard A. W. and Swanner E. D. (in prep) Major and trace element data from Deming Lake, MN, USA (2022-2023).
 - Robbins L. J., Fakhraee M., Smith A. J. B., Bishop B. A., Swanner E. D., Peacock C. L., Wang C.-L., Planavsky N. J., Reinhard C. T., Crowe S. A. and Lyons T. W. (2023) Manganese oxides, Earth surface oxygenation, and the rise of oxygenic photosynthesis. *Earth-Sci. Rev.* **239**, 104368.
 - Robbins L. J., Lalonde S. V., Planavsky N. J., Partin C. A., Reinhard C. T., Kendall B., Scott C., Hardisty D. S., Gill B. C., Alessi D. S., Dupont C. L., Saito M. A., Crowe S. A., Poulton S. W., Bekker A., Lyons T. W. and Konhauser K. O. (2016) Trace elements at the intersection of marine biological and geochemical evolution. *Earth-Sci. Rev.* **163**, 323–348.
 - Roden E. E. and Urrutia M. M. (1999) Ferrous Iron Removal Promotes Microbial Reduction of Crystalline Iron(III) Oxides. *Environ. Sci. Technol.* **33**, 1847–1853.
 - Roden E. E. and Urrutia M. M. (2002) Influence of Biogenic Fe(II) on Bacterial Crystalline Fe(III) Oxide Reduction. *Geomicrobiol. J.* **19**, 209–251.
 - Rooney A. D., Yang C., Condon D. J., Zhu M. and Macdonald F. A. (2020) U-Pb and Re-Os geochronology tracks stratigraphic condensation in the Sturtian snowball Earth aftermath. *Geology* **48**, 625–629.
- Rouxel O. J., Bekker A. and Edwards K. J. (2005) Iron Isotope Constraints on the Archean and Paleoproterozoic Ocean Redox State. *Science* **307**, 1088–1091.
- Rouxel O., Toner B., Germain Y. and Glazer B. (2018) Geochemical and iron isotopic insights into hydrothermal iron oxyhydroxide deposit formation at Loihi Seamount. *Geochim. Cosmochim. Acta* **220**, 449–482.
- Royer R. A., Dempsey B. A., Jeon B.-H. and Burgos W. D. (2004) Inhibition of Biological Reductive Dissolution of Hematite by Ferrous Iron. *Environ. Sci. Technol.* **38**, 187–193.
- Shu Y., Nielsen S. G., Zeng Z., Shinjo R., Blusztajn J., Wang X. and Chen S. (2017) Tracing subducted sediment inputs to the Ryukyu arc-Okinawa Trough system: Evidence from thallium isotopes. *Geochim. Cosmochim. Acta* 217, 462–491.
- Siahi M., Tsikos H., Rafuza S., Oonk P. B. H., Mhlanga X. R., van Niekerk D., Mason P. R. D. and Harris C. (2020) Insights into the processes and controls on the absolute abundance and distribution of manganese in Precambrian iron formations. *Precambrian Res.* **350**, 105878.
- Sieber M., Conway T. M., de Souza G. F., Hassler C. S., Ellwood M. J. and Vance D. (2021) Isotopic fingerprinting of biogeochemical processes and iron sources in the iron-limited surface Southern Ocean. *Earth Planet. Sci. Lett.* **567**, 116967.
- Skulan J. L., Beard B. L. and Johnson C. M. (2002) Kinetic and equilibrium Fe isotope fractionation between aqueous Fe(III) and hematite. *Geochim. Cosmochim. Acta* **66**, 2995–3015.

- Swanner E. D., Bayer T., Wu W., Hao L., Obst M., Sundman A., Byrne J. M., Michel F. M., Kleinhanns
 I. C., Kappler A. and Schoenberg R. (2017) Iron Isotope Fractionation during Fe(II) Oxidation
 Mediated by the Oxygen-Producing Marine Cyanobacterium Synechococcus PCC 7002. Environ.
 Sci. Technol. 51, 4897–4906.
- Swanner E. D., Harding C., Akam S., Lascu I., Ledesma G., Poudel P., Sun H., Duncanson S., Bandy K.,
 Branham A., Bryant-Tapper L., Conwell T., Jamison O. and Netz L. (2023a) Thermal
 stratification and meromixis in four dilute temperate zone lakes. *EGUsphere*, 1–23.
- Swanner E. D., Lambrecht N., Wittkop C., Harding C., Katsev S., Torgeson J. and Poulton S. W. (2020)
 The biogeochemistry of ferruginous lakes and past ferruginous oceans. *Earth-Sci. Rev.* **211**,
 103430.

1659

1660

1661

1662

1663 1664

1665 1666

1667

1668

16711672

1673 1674

1675

1676 1677

1678 1679

1680

- Swanner E. D., Lascu I., Ledesma G., Leung T., Akam S., Chamberlain M., Ostrander C. M. and Heard A. W. (2023b) Water properties of Arco Lake, Budd Lake, Deming Lake, and Josephine Lake in Itasca State Park from 2006-2009 and 2019-2023. ver 4.
- Swanner E. D., Mloszewska A. M., Cirpka O. A., Schoenberg R., Konhauser K. O. and Kappler A. (2015a) Modulation of oxygen production in Archaean oceans by episodes of Fe(II) toxicity. *Nat. Geosci.* **8**, 126–130.
- Swanner E. D., Wu W., Schoenberg R., Byrne J., Michel F. M., Pan Y. and Kappler A. (2015b) Fractionation of Fe isotopes during Fe(II) oxidation by a marine photoferrotroph is controlled by the formation of organic Fe-complexes and colloidal Fe fractions. *Geochim. Cosmochim. Acta* **165**, 44–61.
- Taylor S. R. and McLennan S. M. (1995) The geochemical evolution of the continental crust. *Rev. Geophys.* **33**, 241–265.
- Teutsch N., Schmid M., Müller B., Halliday A. N., Bürgmann H. and Wehrli B. (2009) Large iron isotope fractionation at the oxic–anoxic boundary in Lake Nyos. *Earth Planet. Sci. Lett.* **285**, 52–60.
 - Thibon F., Blichert-Toft J., Tsikos H., Foden J., Albalat E. and Albarede F. (2019) Dynamics of oceanic iron prior to the Great Oxygenation Event. *Earth Planet. Sci. Lett.* **506**, 360–370.
 - Tostevin R. and Ahmed I. A. M. (2023) Micronutrient availability in Precambrian oceans controlled by greenalite formation. *Nat. Geosci.*, 1–6.
 - Tsikos H., Matthews A., Erel Y. and Moore J. M. (2010) Iron isotopes constrain biogeochemical redox cycling of iron and manganese in a Palaeoproterozoic stratified basin. *Earth Planet. Sci. Lett.* **298**, 125–134.
 - Vuillemin A., Friese A., Wirth R., Schuessler J. A., Schleicher A. M., Kemnitz H., Lücke A., Bauer K. W., Nomosatryo S., von Blanckenburg F., Simister R., Ordoñez L. G., Ariztegui D., Henny C., Russell J. M., Bijaksana S., Vogel H., Crowe S. A., Kallmeyer J. and the Towuti Drilling ProjectScience team (2020) Vivianite formation in ferruginous sediments from Lake Towuti, Indonesia. *Biogeosciences* 17, 1955–1973.
- Vuillemin A., Mayr C., Schuessler J. A., Friese A., Bauer K. W., Lücke A., Heuer V. B., Glombitza C.,
 Henny C., von Blanckenburg F., Russell J. M., Bijaksana S., Vogel H., Crowe S. A. and
 Kallmeyer J. (2022) A one-million-year isotope record from siderites formed in modern
 ferruginous sediments. *GSA Bull.* 135, 504–522.
- Wang C., Robbins L. J., Planavsky N. J., Beukes N. J., Patry L. A., Lalonde S. V., Lechte M. A., Asael
 D., Reinhard C. T., Zhang L. and Konhauser K. O. (2023) Archean to early Paleoproterozoic iron formations document a transition in iron oxidation mechanisms. *Geochim. Cosmochim. Acta* 343, 286–303.
- Welch S. A., Beard B. L., Johnson C. M. and Braterman P. S. (2003) Kinetic and equilibrium Fe isotope fractionation between aqueous Fe(II) and Fe(III). *Geochim. Cosmochim. Acta* 67, 4231–4250.
- Wiesli R. A., Beard B. L. and Johnson C. M. (2004) Experimental determination of Fe isotope
 fractionation between aqueous Fe(II), siderite and "green rust" in abiotic systems. *Chem. Geol.* 211, 343–362.
- Wittkop C., Bartley J. K., Krueger R., Bouvier A., Georg R. B., Knaeble A. R., St. Clair K., Piper C. and Breckenridge A. (2020a) Influence of provenance and transport process on the geochemistry and

radiogenic (Hf, Nd, and Sr) isotopic composition of Pleistocene glacial sediments, Minnesota, USA. *Chem. Geol.* **532**, 119390.

- Wittkop C., Swanner E. D., Grengs A., Lambrecht N., Fakhraee M., Myrbo A., Bray A. W., Poulton S. W. and Katsev S. (2020b) Evaluating a primary carbonate pathway for manganese enrichments in reducing environments. *Earth Planet. Sci. Lett.* **538**, 116201.
 - Wittkop C., Teranes J., Lubenow B. and Dean W. E. (2014) Carbon- and oxygen-stable isotopic signatures of methanogenesis, temperature, and water column stratification in Holocene siderite varves. *Chem. Geol.* **389**, 153–166.
 - Wu L., Beard B. L., Roden E. E. and Johnson C. M. (2011) Stable Iron Isotope Fractionation Between Aqueous Fe(II) and Hydrous Ferric Oxide. *Environ. Sci. Technol.* **45**, 1847–1852.
 - Yang X., Guo Q., Boyko V., Avetisyan K., Findlay A. J., Huang F., Wang Z. and Chen Z. (2022) Isotopic reconstruction of iron oxidation-reduction process based on an Archean Ocean analogue. *Sci. Total Environ.* **817**, 152609.
 - Young E. D., Galy A. and Nagahara H. (2002) Kinetic and equilibrium mass-dependent isotope fractionation laws in nature and their geochemical and cosmochemical significance. *Geochim. Cosmochim. Acta* **66**, 1095–1104.
- Zegeye A., Bonneville S., Benning L. G., Sturm A., Fowle D. A., Jones C., Canfield D. E., Ruby C.,
 MacLean L. C., Nomosatryo S., Crowe S. A. and Poulton S. W. (2012) Green rust formation
 controls nutrient availability in a ferruginous water column. *Geology* 40, 599–602.

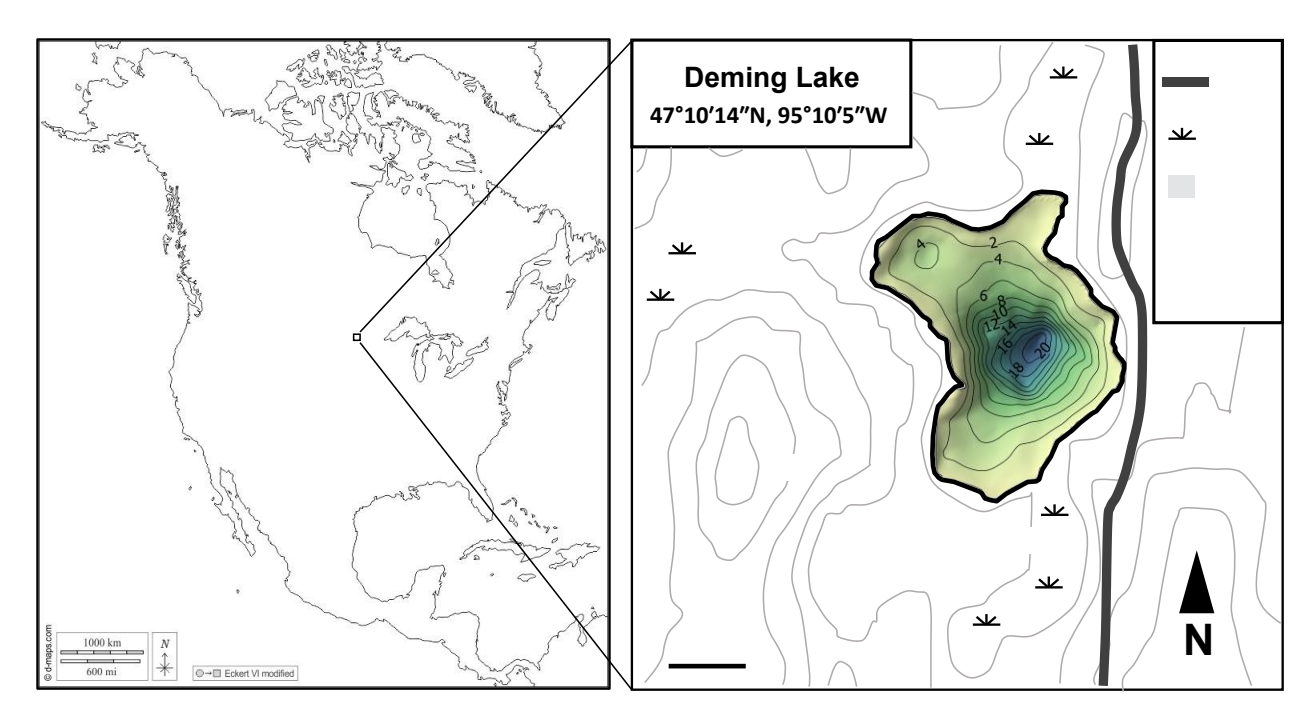


Figure 1: Map of Deming Lake, MN, USA. Left: Location of Deming Lake on the North American Continent. Right: Deming Lake. Bathymetric contours are 2 m, and topographic contours are 10 m. Geographic information adapted from Swanner et al. (2023a).

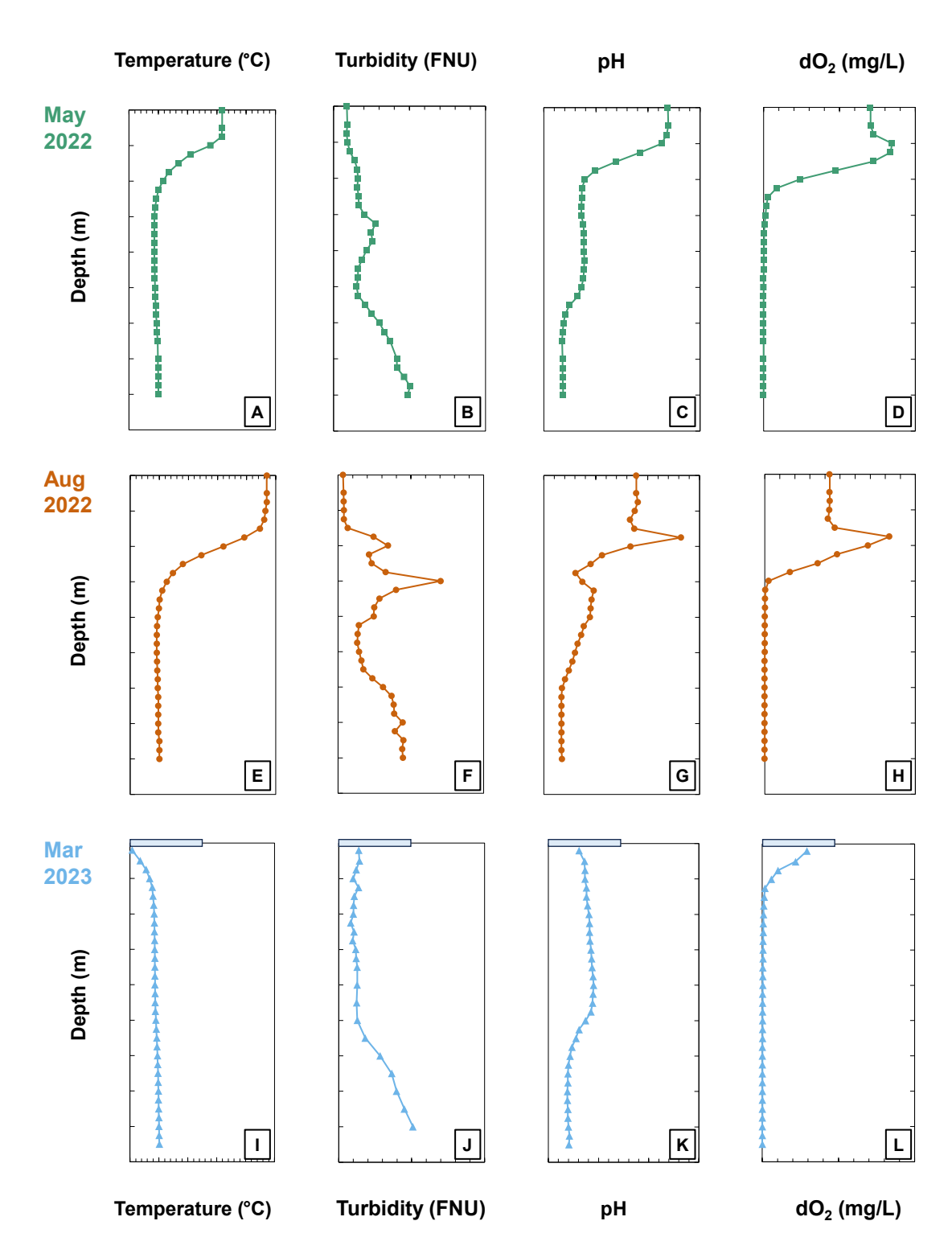


Figure 2: Water column properties in Deming Lake. Temperature, turbidity, pH, and dissolved O_2 in May 2022 (A-D), August 2022 (E-H), and the ice-covered water column in March 2023 (I-L). Horizontal axis scales are the same for all panels in each column.

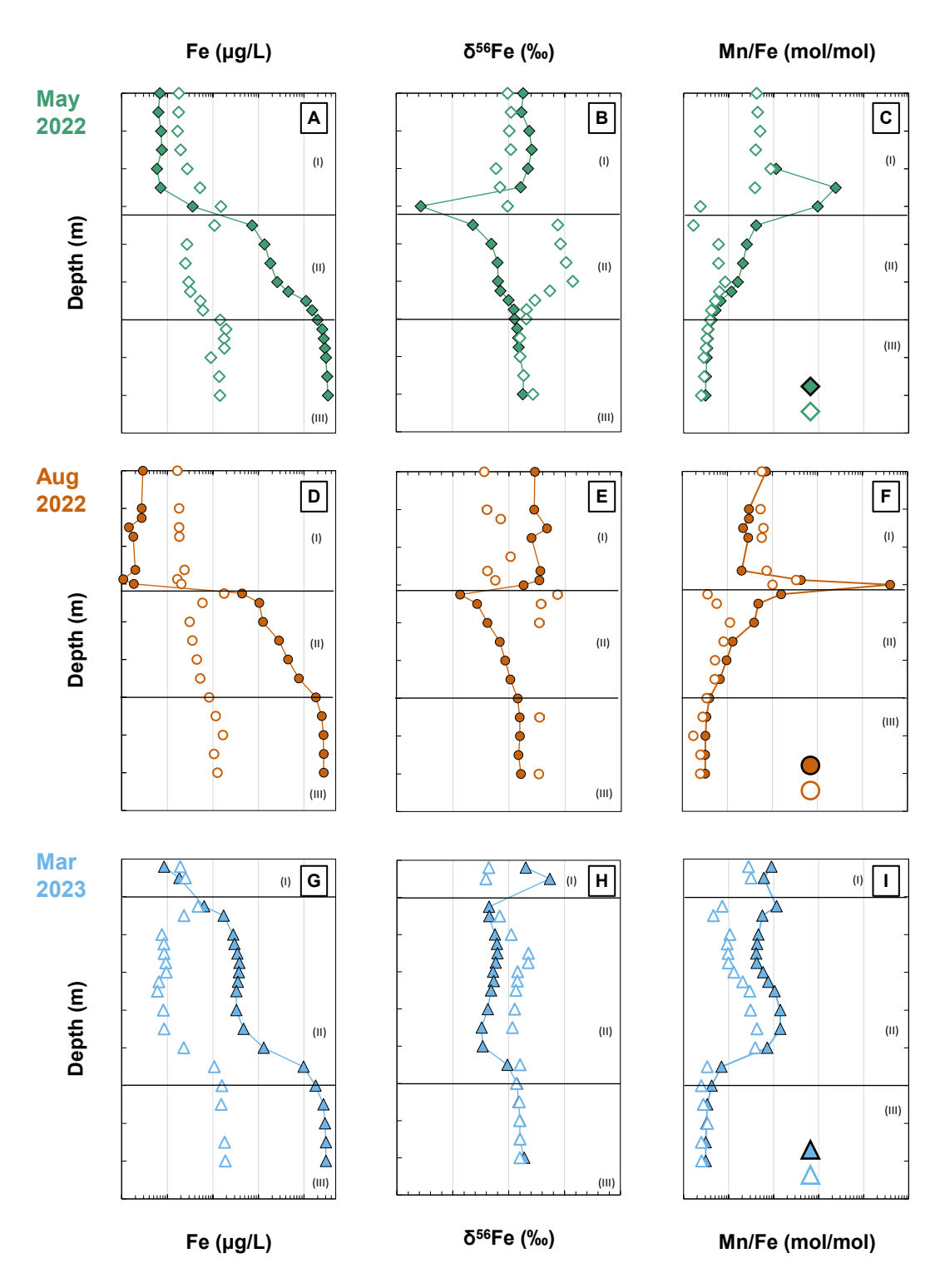


Figure 3: Water column Fe, δ^{56} Fe, and Mn/Fe systematics at Deming Lake. Dissolved (filled symbols) and particulate (open symbols) Fe, δ^{56} Fe, and Mn/Fe in May 2022 (A-C), August 2022 (D-F), and March 2023 (G-I). Error bars for δ^{56} Fe are smaller than the datapoints. Horizontal axis scales are the same for all panels in each column. (I), (II), (III) labels and horizontal black lines indicate the position of Layers (I), (II), and (III), and the boundaries between them, respectively.

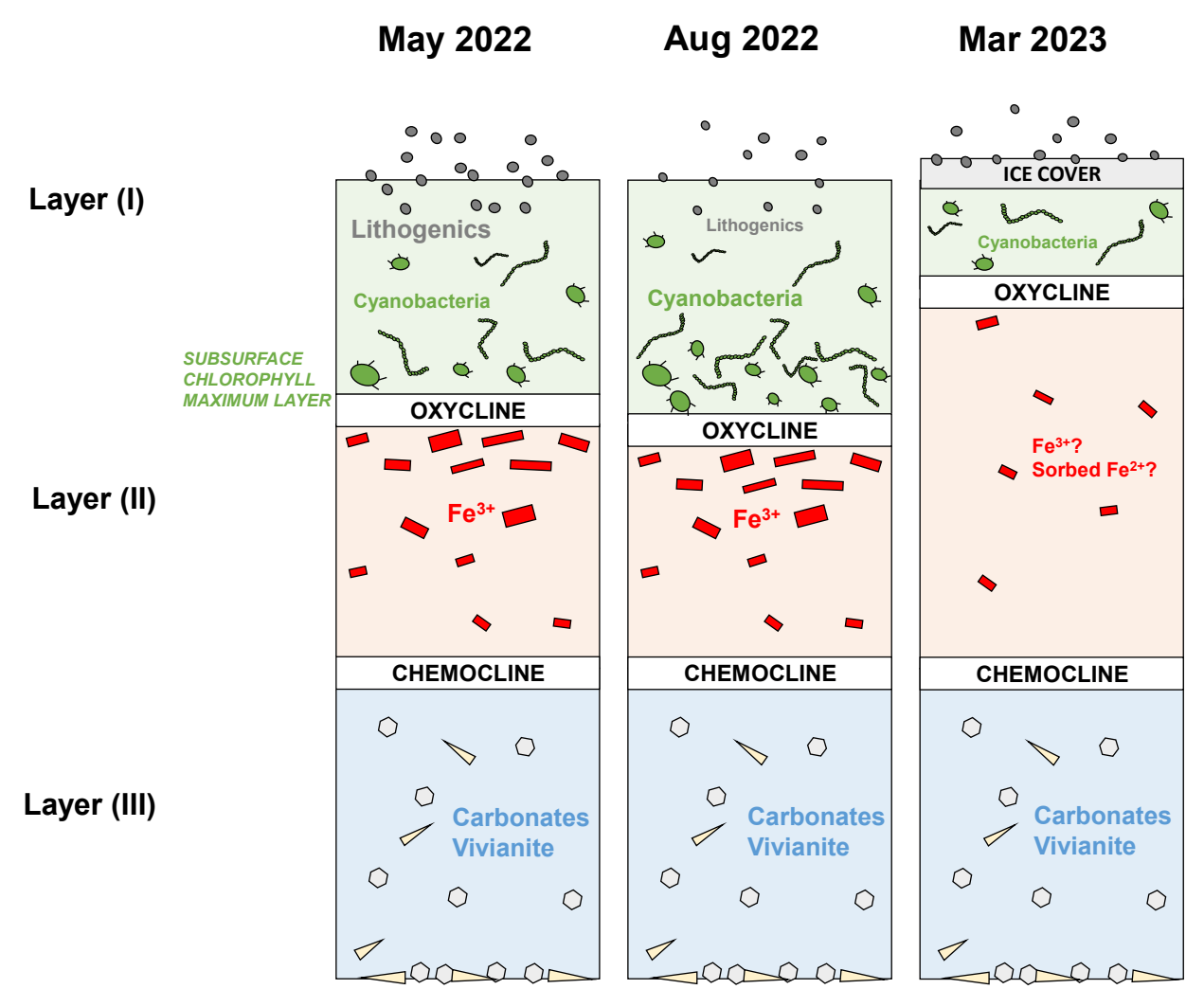


Figure 4: Cartoon depiction of three major Fe cycling layers in Deming Lake through three sampling seasons. Layer (I) above the oxycline has an Fe cycle dominated by biological Fe uptake and seasonally variable lithogenic particle delivery. Layer (II) immediately beneath the redoxcline sees oxidation of Fe^{2+}_{aq} -rich anoxic deep waters, resulting in extensive Fe^{3+} particle precipitation. Beneath the ~12 m seasonally stable chemocline, anoxic conditions and precipitation of Fe^{2+} carbonates and vivianite dominates. During the winter months as seen in March 2023, ice cover prevents lithogenic input and causes shallowing of the oxycline. Mid-depth waters in winter see very limited particle formation after an initial vertical homogenization of waters above 12 m depth driven by winter cooling and destratification.

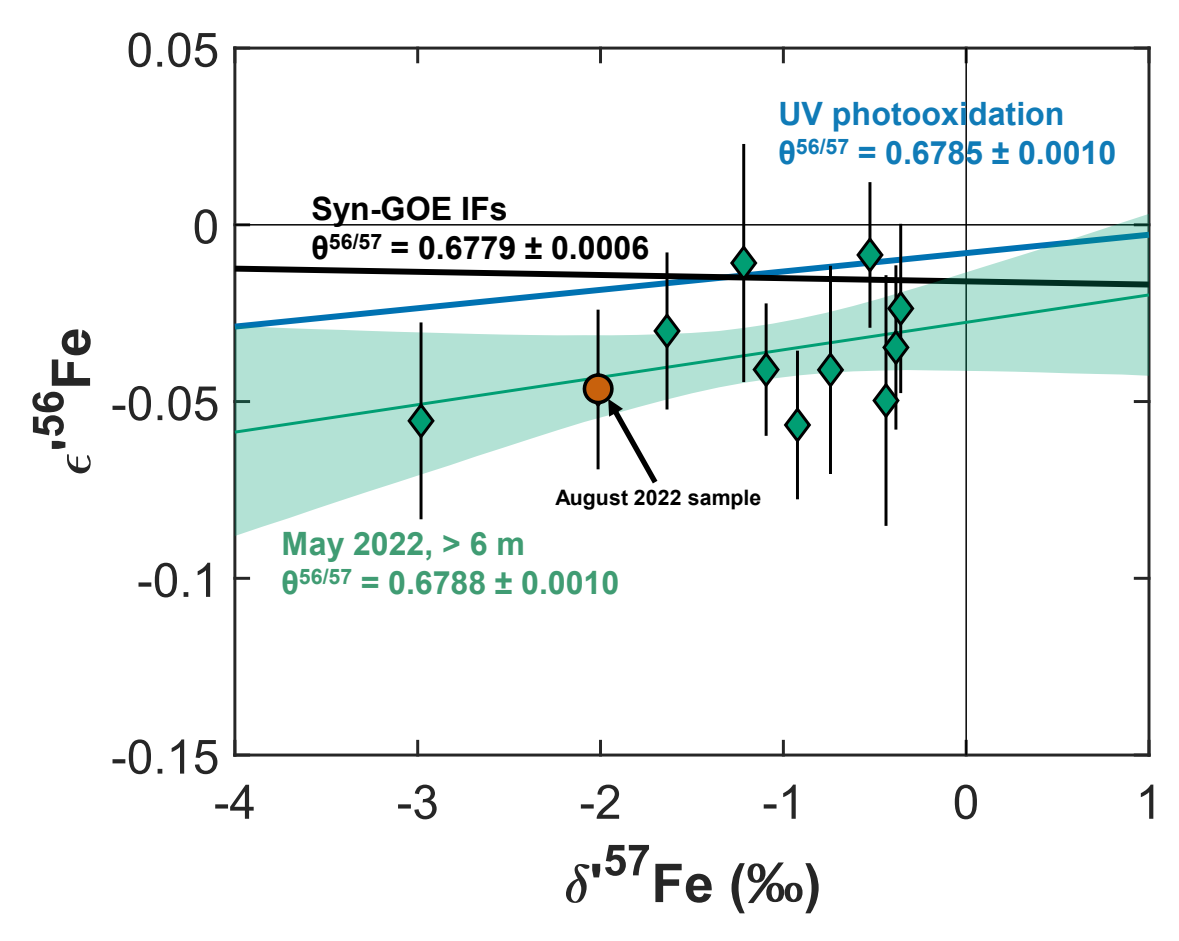


Figure 5: High-precision triple Fe isotope systematics for a natural ferruginous water column redoxcline. Datapoints are for the dissolved Fe pool sample from the May 2022 water column beneath the oxycline (with one sample from August 2022 indicated by the black arrow). High-precision ϵ^{156} Fe values are parts per 10,000 deviations in 56 Fe/ 54 Fe from the expected value of the high-temperature limit equilibrium mass fractionation law passing through the origin. The slope for the Deming Lake water column mass fractionation array is within error of the high temperature limit equilibrium law and previous determinations of the mass fractionation law for syn-GOE Mn-rich IFs, and laboratory UV photooxidation.

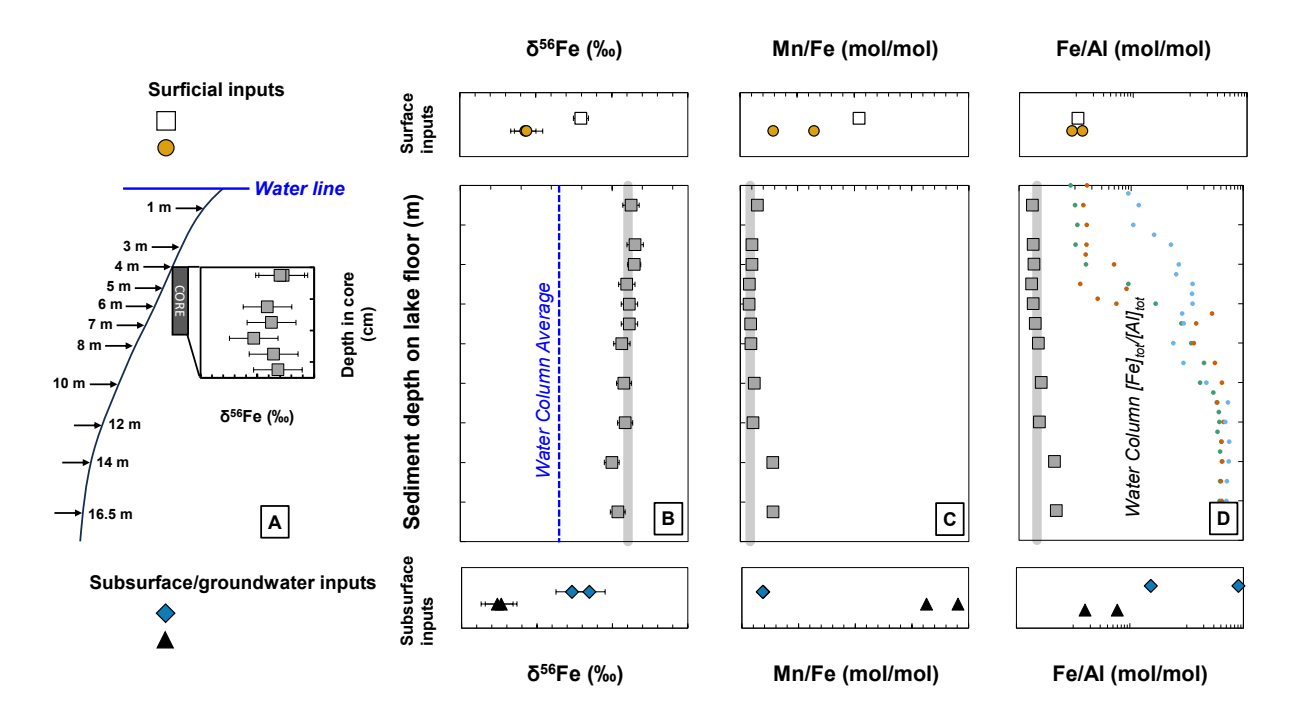


Figure 6: Iron isotopic geochemical systematics of sedimentary outputs and potential inputs for Deming Lake. A: Schematic of lake floor depth profile sampling (vertically exaggerated), with inset δ^{56} Fe values for a 7 cm gravity core taken at 4 m lake depth. **B:** δ^{56} Fe for Deming Lake bottom sediments from a shallow to depth transect (grey squares), ice core-trapped eolian particles (white square), dissolved Fe in nearby bog waters (orange circles), and groundwaters sampled at springs near Elk Lake (dark blue diamonds) and Nicollet Creek (black triangles). Blue dashed line and grey shaded line show values for the Fe-weighted average water column, and the upper continental crust (UCC; from X –M Liu et al., 2022), respectively. **C:** Mn/Fe systematics, with symbols the same as for **B.** UCC value from Taylor and McLennan (1995). **D:** Fe/Al systematics, with symbols the same as for **B.** UCC value from Taylor and McLennan (1995). Small circles show total (dissolved + particulate) Fe/Al ratios for the Deming Lake water column in May 2022 (teal), August 2022 (brown), and March 2023 (light blue).

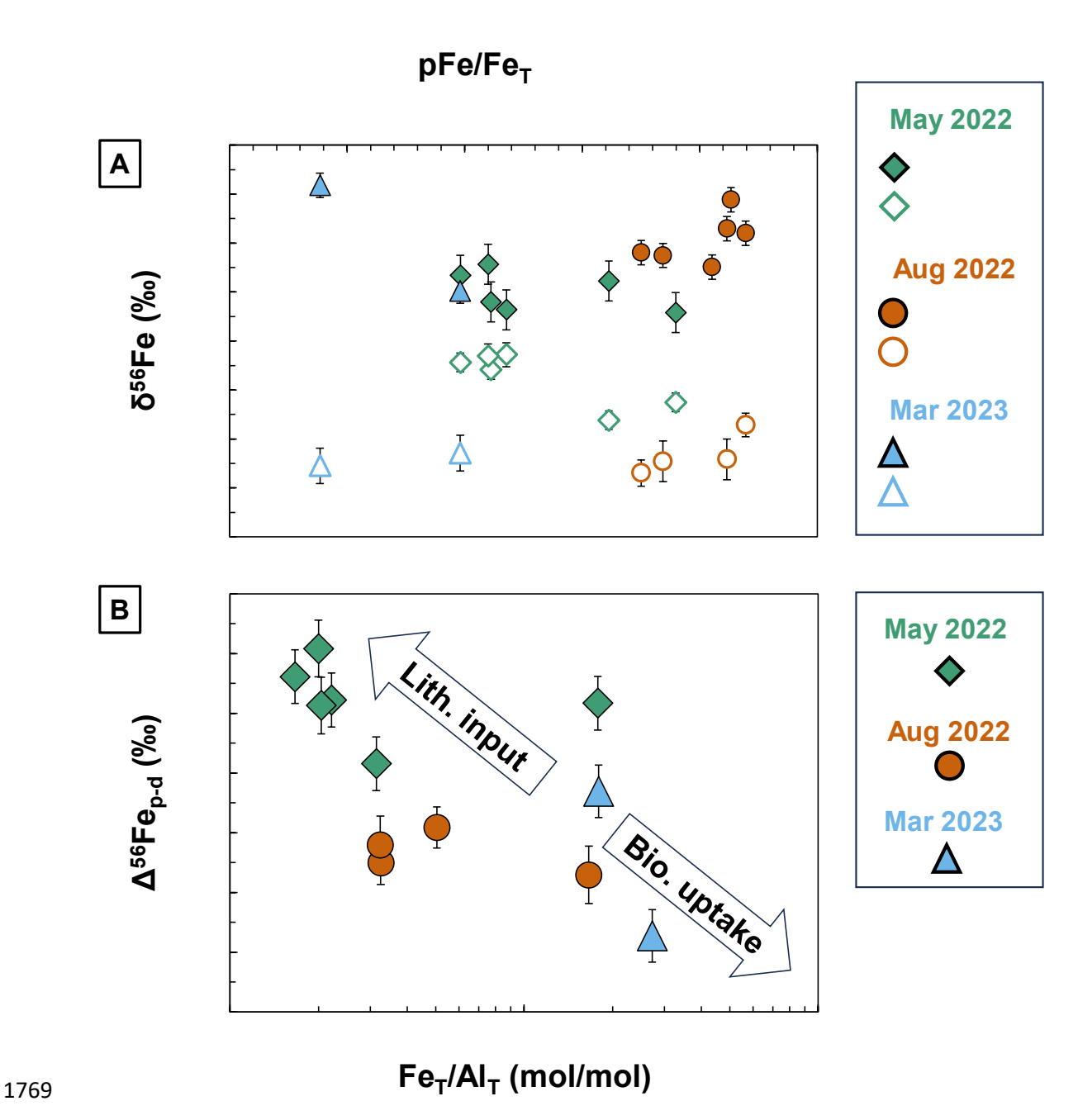


Figure 7: Iron isotope fractionation dynamics above the oxycline in Layer (I) of Deming Lake. A: Iron isotopic compositions of dissolved (filled symbols) and particulate (open symbols) fractions vs. the fraction of total Fe (dissolved + particulate) in Layer (I). Difference in δ^{56} Fe between dissolved and particulate are not simply explained by variable degrees of particulate uptake with a constant fractionation factor. **B:** Iron isotopic fractionation between particulate and dissolved Fe (Δ^{56} Fe_{p-d}) vs. total Fe:Al ratio in Layer (I). Most variation in Δ^{56} Fe_{p-d} in Layer (I) appears to be explainable with dilution of a large biologically induced negative fractionation effect by addition of lithogenic material with δ^{56} Fe ≈ 0 % to both the dissolved and particulate Fe pools. Lithogenic addition is most pronounced in May 2022 and least pronounced in March 2023 when the lake surface is under ice cover.

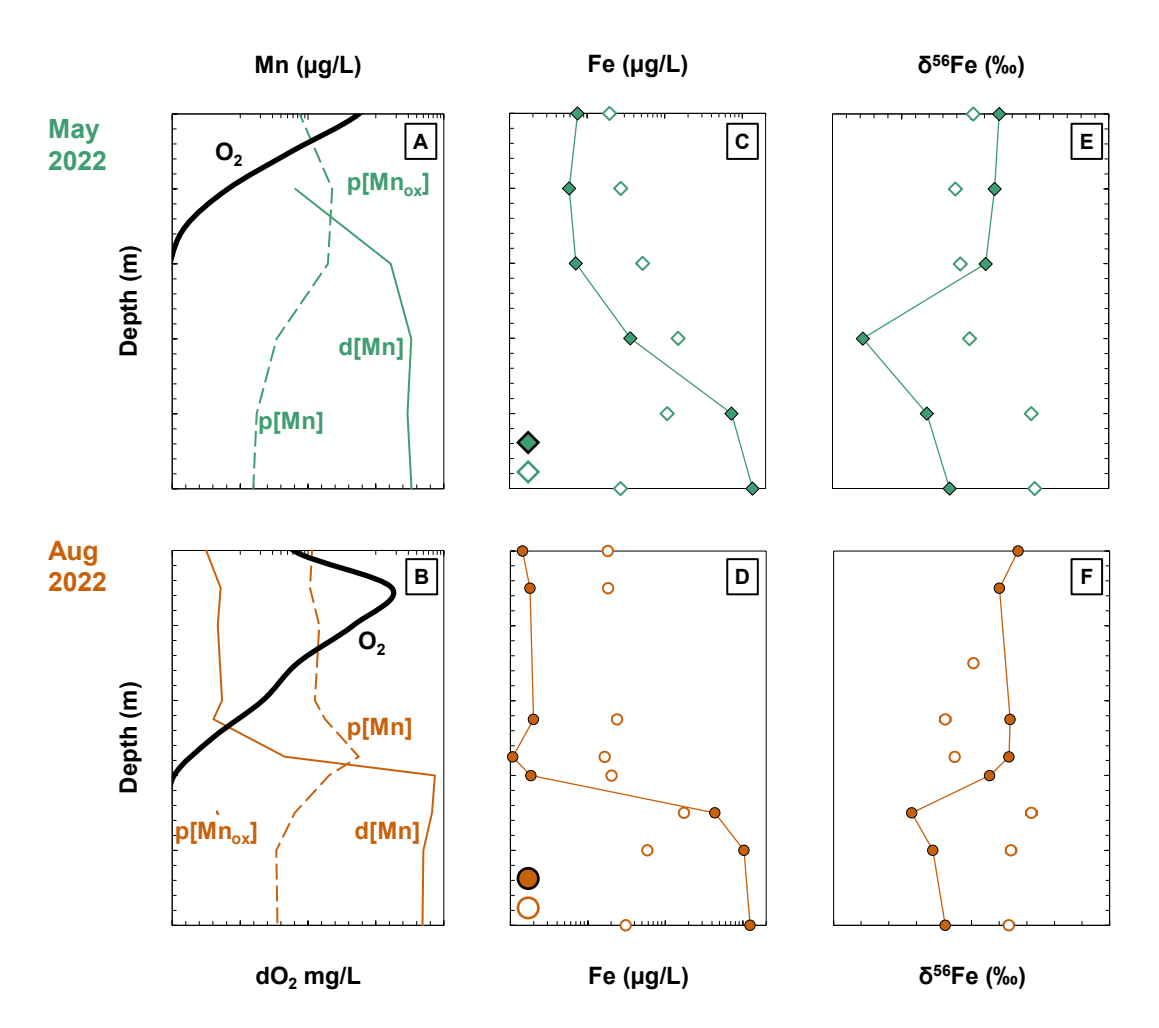


Figure 8: Water redox systematics impacting Fe cycling around the oxycline and top of Layer (II). A: May 2022, and B: Augusts 2022 dissolved O_2 dissolved, bulk particulate, and particulate oxide Mn. C: May 2022, and D: August 2022 dissolved and particulate Fe. E: May 2022, and F: August 2022 dissolved and particulate δ^{56} Fe. Symbols in C-F are the same as in Figure 3. Oxygen and oxidized Mn species decline just above the onset of the most extensive dissolved Fe removal and Fe³⁺ particle formation, suggesting that atmospheric and *in situ*-produced O_2 , and/or sinking Mn oxides are being reduced in the process of oxidizing dissolved Fe²⁺_{aq}.



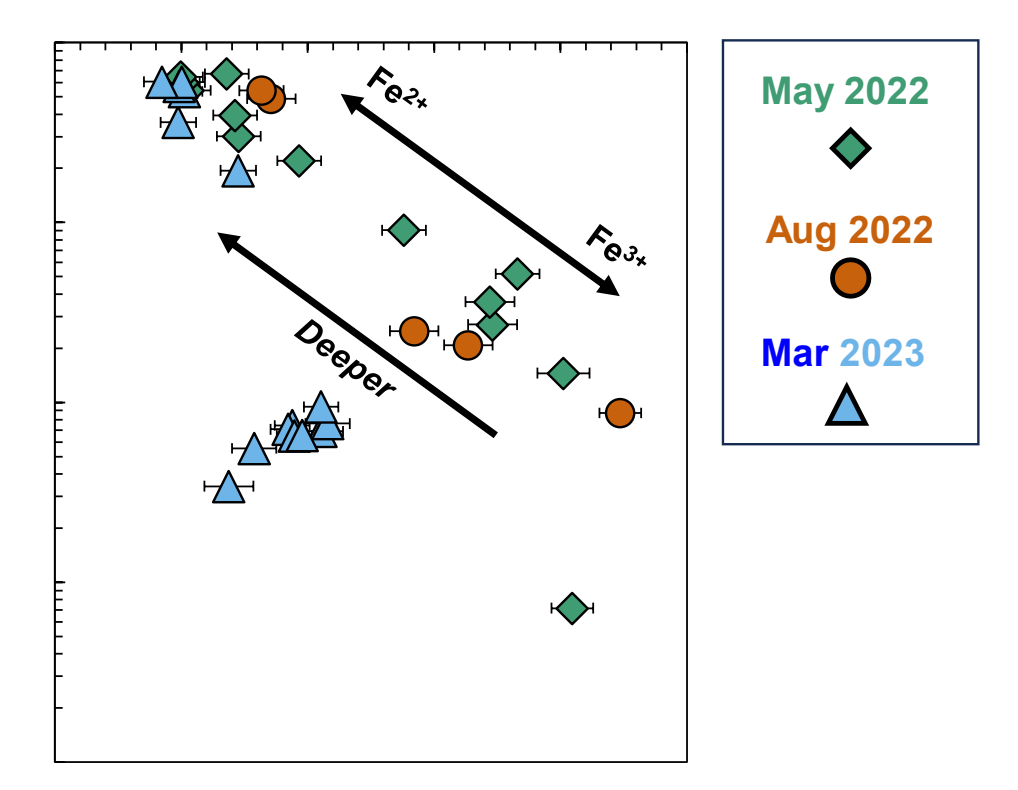


Figure 9: Impact of dissolved Fe^{2+}_{aq} on Fe isotopic fractionation between dissolved and particulate Fe beneath the oxycline. Negative correlations between $\Delta^{56}Fe_{p-d}$ and dFe (which increases with depth) in May and August 2022 are consistent with an increase in the fraction of particulate Fe hosted in Fe^{2+} -bearing minerals or adsorbed to ferric minerals as Fe^{2+}_{aq} in more Fe-rich waters found deeper below the oxycline. A smaller range of $\Delta^{56}Fe_{p-d}$ values in March 2023 at lower dFe levels is consistent with limited availability of oxidants in the ice-covered water column.

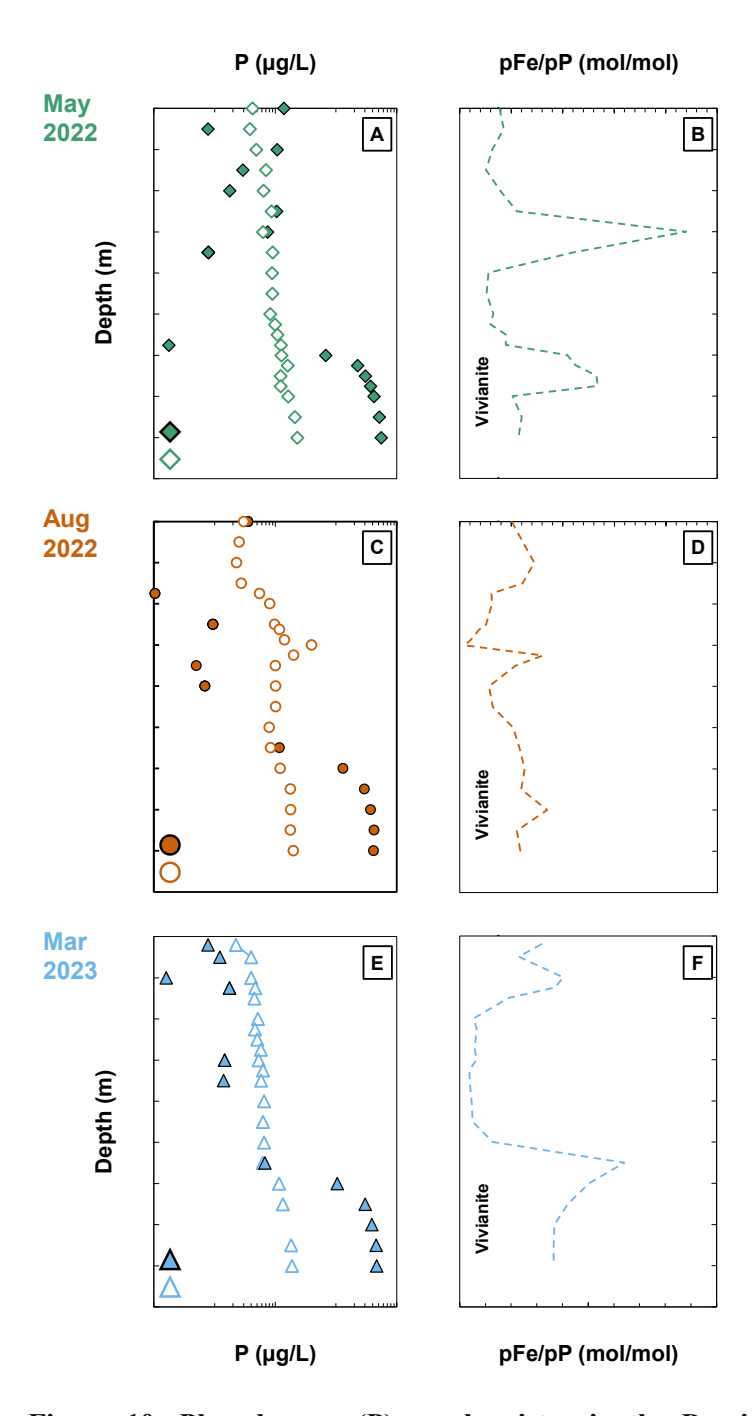


Figure 10: Phosphorous (P) geochemistry in the Deming Lake water column. Dissolved (filled symbols) and particulate (open symbols) P, and particulate Fe/P ratio, in May 2022 (**A-B**), August 2022 (**C-D**), and March 2023 (**E-F**). The 1.5 Fe/P stochiometric ratio of vivianite is shown as a black dotted line. Vivianite is saturated in the water column below 11 m depth. Horizontal axis scales are the same for all panels in each column.

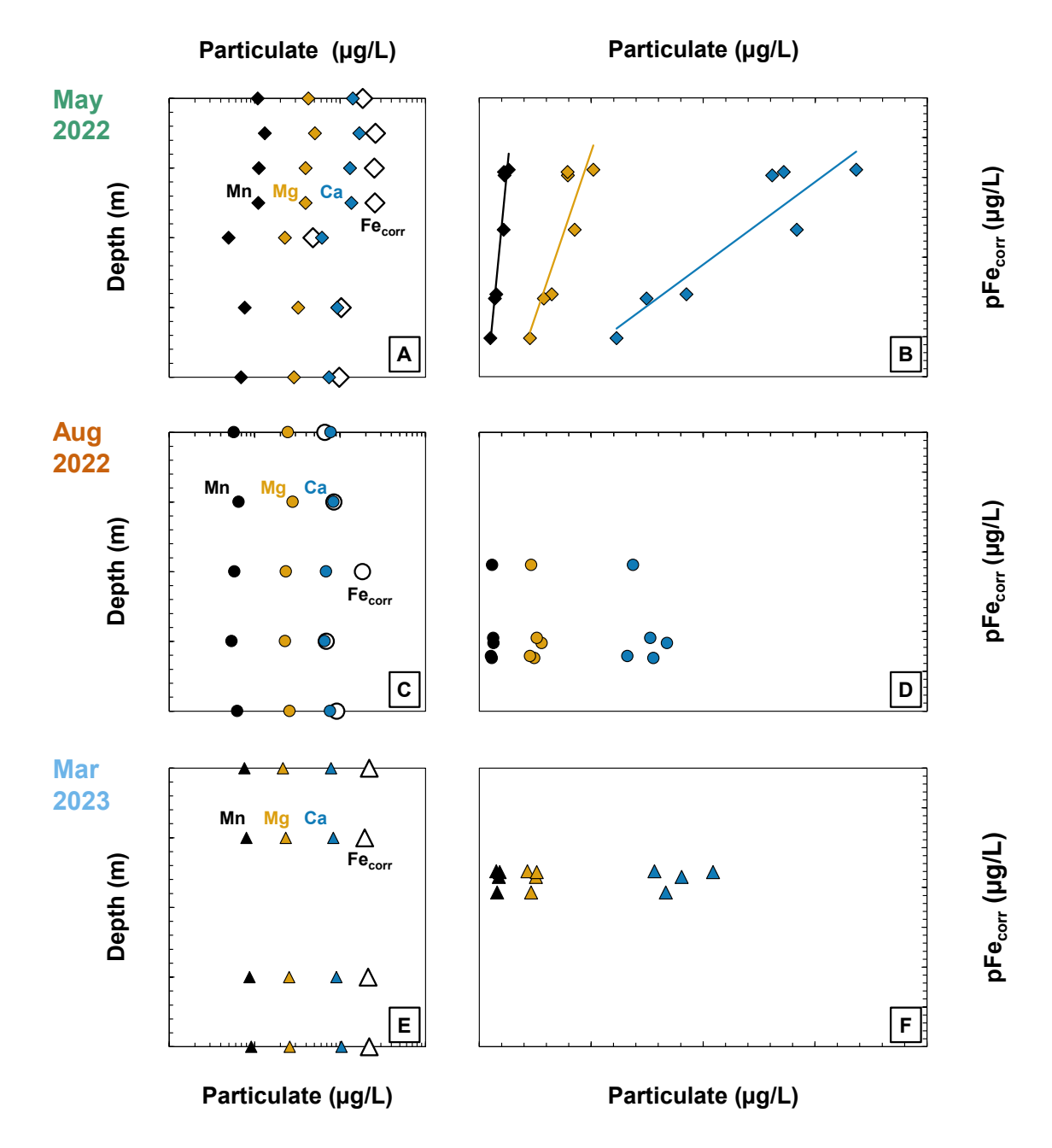


Figure 11: Particulate concentrations for likely carbonate-associated metals beneath the chemocline in Layer (III) of the Deming Lake water column. A: Particulate Mn (purple), Mg (gold), Ca (pale blue), and Fe corrected for vivianite (Fe_{corr}, open symbols) concentrations in May 2022. **B:** Particulate Mn, Mg, and Ca vs. pFe_{corr} in May 2022. Positive correlations suggest the majority of non-vivianite-associated particulate Fe is associated with carbonates (e.g. siderite, ankerite). **C-D**, and **E-F:** As for **A-B**, for August 2022 and March 2023 respectively. Note that no positive correlations are observed in **D** and **F**, which may suggest additional phases host Fe in particles beneath the chemocline in these seasons (see text for discussion). Horizontal axis scales are the same for all panels in each column.

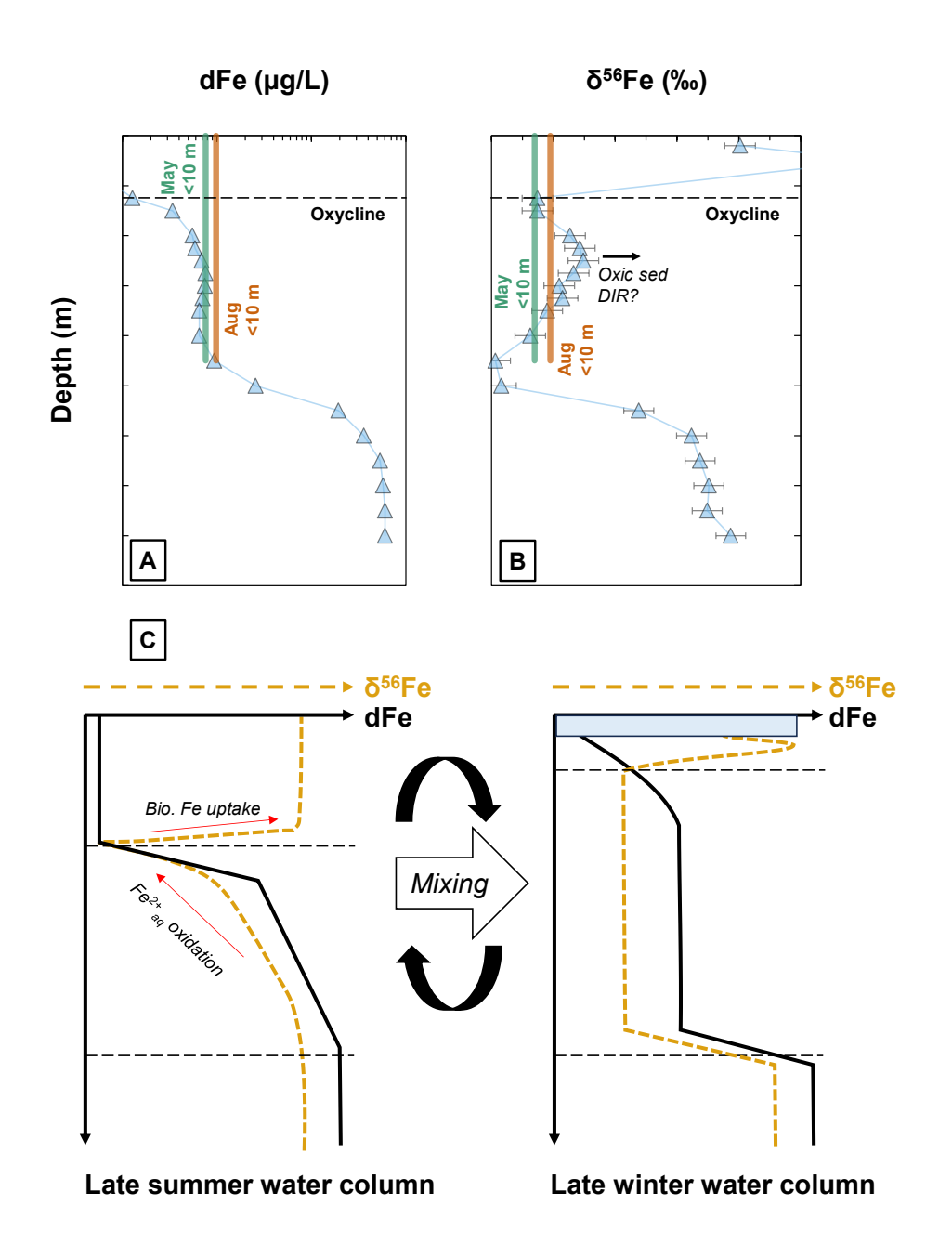


Figure 12: Seasonal dissolved Fe systematics in the Deming Lake water column. A: Dissolved Fe and B: δ^{56} Fe in the ice-covered March 2023 water column as shown in Fig. 3, overlain with calculated column-averaged values (Fe_{col} and δ^{56} Fe_{col}) for the May 2022 (teal) and August 2022 (brown) water columns from 0-9 m (top of the chemocline) depth. The muted depth-dependent variation between the chemocline and shallowed oxycline that is observed in the March 2023 water column is attributed to surface cooling and mixing of the epilimnion and metalimnion (Layers (I) and (II)) of a 'Late Summe' water column and reestablishment of the thermocline in winter (Swanner et al., 2023). This is shown schematically in in C. Subsequent development of dFe and δ^{56} Fe variations in the upper ~2 m of the lake is attributed to establishment of a new, shallow oxycline and associated Fe mineralization and biological uptake processes.

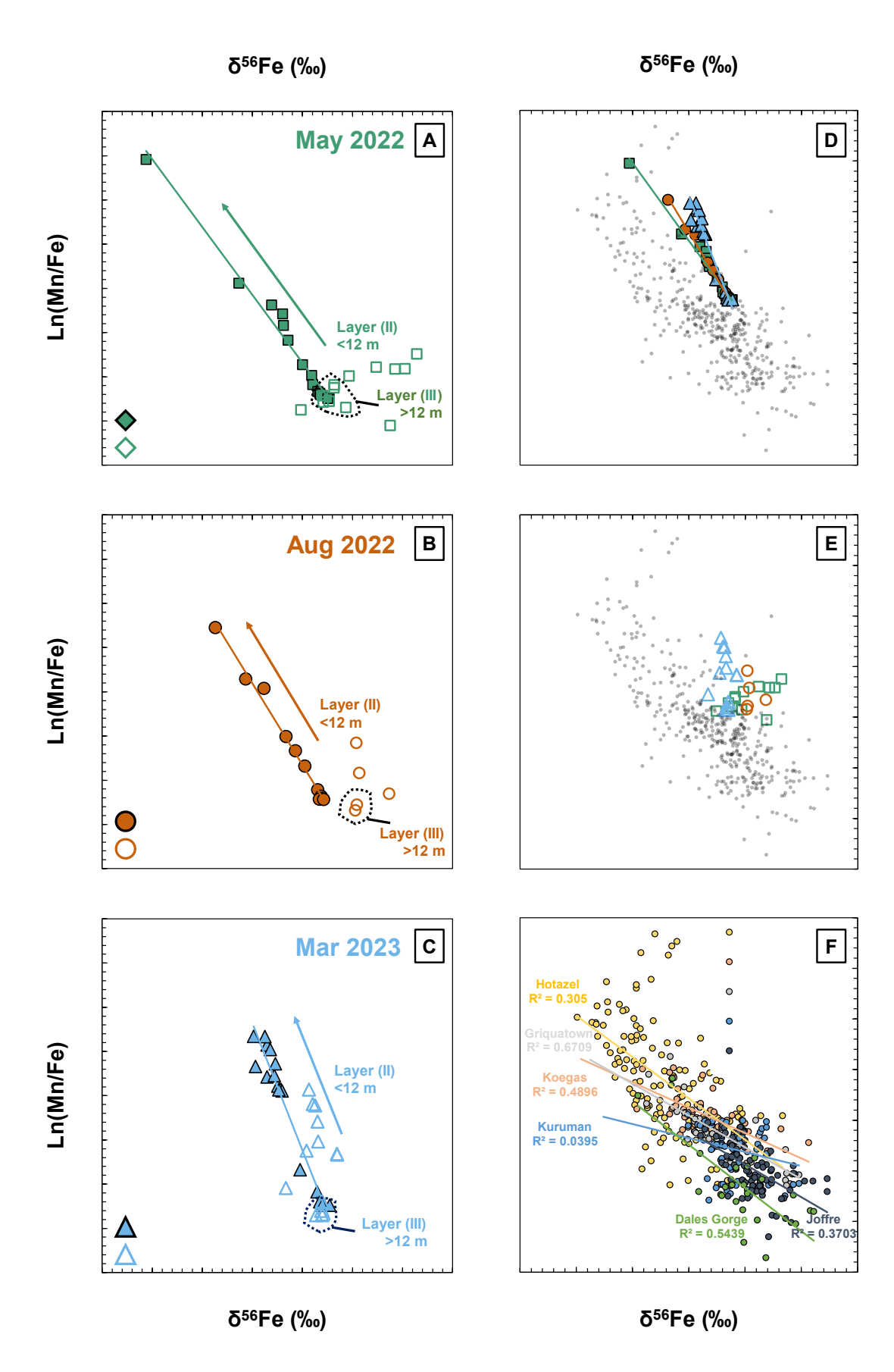


Figure 13: Sub-oxycline Mn/Fe vs. δ⁵⁶Fe dynamics in the Deming Lake water column and their implications for understanding these trends in early Paleoproterozoic iron formations (IFs). A: May 2022, **B:** August 2022, and **C:** March 2023 Ln(Mn/Fe) vs. δ^{56} Fe for dissolved (filled symbols) and particulate phases for Layers (II) and (III) sampled below the oxycline. All dissolved sample arrays (D) define strong negative log-linear correlations consistent with removal of isotopically heavy Fe to particles with little removal of Mn, roughly replicating the systematics seen in pre- or syn-GOE IFs (small grey circles). Particulate phases show no systematic Ln(Mn/Fe) vs. δ^{56} Fe behaviors, with Layer (III) samples falling close to dissolved values and Layer (II) samples being consistently more positive in δ^{56} Fe but showing no uniform behavior in Mn/Fe fractionation (E), and thus not effectively replicating trends seen in pre- or syn-GOE IFs (small grey circles). In the context of these results, we suggest that well developed negative Ln(Mn/Fe) vs. δ⁵⁶Fe trends in several distinct IFs shortly pre- or syn-dating the GOE (F) are unlikely to reflect simple one-phase deposition of oxide precipitates following a Raleigh distillation-type behavior, and may require simultaneous formation of more than one Fe-bearing phase in the early Paleoproterozoic water column. Note that A-E are plotted against the same axis scales while F features a different axis scale. All IF data are from previous publications (Haugaard et al., 2016; Kurzweil et al., 2016; Lantink et al., 2018; Thibon et al., 2019; Tsikos et al., 2010; Wang et al., 2023).